Multi Pulse Terrestrial Gamma-ray Flashes and optical pulses of lightning observed by ASIM

Master Thesis in Space Physics
by
Anders Nødland Fuglestad

Department of Physics and Technology
University of Bergen
Norway

May 31, 2023

Acknowledgments

First and foremost I would like to thank my supervisors Nikolai Østgaard and Andrey Mezentsev for the regular guidance and thoroughly reviewing my work. Andrey for the great help when working with the data and Nikolai for the frequent feedback on my writing.

I would like to thank every one who worked on ASIM for the X- and Gamma-Ray and optical data and Vaisala for the lightning location data.

I would like to thank my fellow student Sander for listening to my rants, when I think I understood something only to realize I didn't and for offering his perspective when I got stuck.

Finally I would like to thank my friends Endre and Herman for keeping my sanity in check while working long hours and late at night, and my family for their support.

Anders Nødland Fuglestad

May 31, 2023

Abstract

Terrestrial Gamma-ray Flashes (TGFs) are short sub-millisecond bursts of energetic gamma rays emitted from lightning flashes inside thunder clouds. Multi pulse TGFs are events where two or more TGFs occur within the same thunder cell hundreds of μs to a few ms apart.

In this thesis we present 52 multi pulse TGFs detected by The Atmosphere-Space Interactions Monitor (ASIM) since launch until the end of 2022. ASIM is uniquely designed for detection of TGFs. In addition, having optical instruments that allows for studying these multi pulse TGFs with associated optical data.
The events are also compared to very low frequency (VLF) sferics from the Vaisala's Global Lightning Dataset (GLD).

7 out of the 52 events where identified to likely have an optical pulse associated with at least one of the TGF pulses, and 24 out of the 52 events where identified as having a likely GLD sferic association.

Based on the gamma-ray data we found that multi pulse TGFs may be characterized by one of the following three distinct patterns:

1. Two bright peaks with similar intensities
2. Initial bright peak followed by subsequent peaks with decreasing intensities.
3. Initial weak peaks followed by subsequent peaks with increasing intensities.

The time separation from the first to the last peak of multi pulse TGFs are found to generally be below 2.3 ms, with a smaller group of events having time separations below 6 ms. This appears to mostly be consistent with the time of lightning leader propagation found by Cummer S. A. et al. [2015], with the exception of two multi pulse TGFs which have a time separation above 10 ms.

It was found that for Multi pulse TGFs with associated optical pulses, the TGFs were always produced before the optical pulse in agreement with the results found by [Skeie C. A. et al. 2022] and [Heumsesser M. et al. 2021].

List of abbreviations

AGILE	Astro-Rivelatore Gamma a Immagini Leggero
ASIM	Atomsphere-Space Interactions Monitor
BATSE	Burst and Transient Source Experiment
BGO	Bismuth-Germanium-Oxide
CEPA	Columbus Externals Payloads Adaptor
CHU	Camera Head Unit
CZT	Cadmium-Zink-Telluride
DAU	Detector Assembly Unit
DHPU	Data Handling and Power Unit
DM	Detector Module
DPU	Data Processing Unit
FoV	Field of View
GBM	Gamma-ray Burst Monitor
GLD	Vaisala's Global Lightning Dataset
HED	High-Energy Detector
IC	Intra Cloud
ISS	International Space Station
LCL	Lifted Condensation Level
LED	Low-Energy Detector
LF	Low Frequency
LHLV	Local Horizontal Local Vertical
MDF	Magnetic Direction Finding
MMIA	Modular Multispectral Imaging Array

MXGS	Modular X- and Gamma-ray Sensor
NED	North East Down
PMT	Photomultiplier Tube
RHESSI	Reuven Ramaty High Energy Solar Spectroscopic Imager
RREA	Relativistic Runaway Electron Avalanche
TGF	Terrestrial Gamma-ray Flash
TOA	Time of Arrival
VLF	Very Low Frequency
WWLLN	World Wide Lightning Location Network

Contents

Chapter 1

Introduction

Terrestrial Gamma-ray flashes (TGFs) are short bursts of gamma rays produced through the bremsstrahlung process by energetic electrons accelerated by the electric fields within thunderclouds [Dwyer et al., 2012].
Multi pulse TGFs are events where two or more TGFs occur within hundreds of μs to a couple of ms apart from the same thunder cell.

There is currently two TGF models capable of explaining the amount of energetic electrons observed from TGFs: Lightning leader model and relativistic feedback discharge model.
Both models agree that TGFs occur due to electrons being accelerated in electric fields strong enough to overcome the friction force of the electrons in what is known as the runaway electron process. The electrons are then multiplied into a cascade of electrons known as a relativistic runaway electron avalanche (RREA) via Møller scattering [Stanbro et al. 2018] [Dwyer et al., 2012]. Where the models disagree is the specific location of the electrical fields that accelerate the electrons. The lightning leader model assumes electron acceleration occurs from electric fields at the tip of the lightning leader, the electrons become accelerated by the cold runaway process before going through RREA multiplication [Carlson et al., 2009] [Celestin & Pasko, 2011]. The relativistic feedback discharge model can work in both leader fields and in large scale electric fields within the thundercloud, where an initial seed electron can cause an exponential amount of RREA to occur due to backward propagation of runaway positrons and backscattered X-rays [Dwyer, 2012].

Both models are capable of explaining multi pulse TGFs. In the lightning leader model multi pulse TGFs are a result of multiple RREA occurring at different times during leader progression [Carlson et al., 2009] [Celestin & Pasko, 2011]. In the relativistic feedback discharge model multi pulse TGFs can occur if the potential difference in the avalanche region of the electric field is large enough that a self-propagating discharge known as a relativistic feedback streamer forms. The relativistic feedback streamer propagates in a pulsed fashion and produces a burst of gamma-rays with each propagation [Dwyer, 2012].

TGFs were first reported by Fishman et al. [1994] from observations by the Burst and Transient Source Experiment (BATSE) on board the Compton Gamma-ray Observatory, The observations from BATSE included several multi pulse TGFs. Since then TGFs and multi pulse TGFs have been detected by several spacecraft such as AGILE [Marisaldi M et al., 2010], Fermi [Briggs M. S. et al., 2010], RHESSI [Grefenstette B. W. et al., 2009] and ASIM [Østgaard N et al., 2019].

The Atmosphere-Space Interactions Monitor (ASIM) launched in 2018, is the first spacecraft designed specifically to observe TGFs. Compared to previous space craft capable of detecting TGFs ASIM has both gamma-ray, Modular X- and Gamma-ray Sensor (MXGS) and optical instruments, Modular Multispectral Imaging Array (MMIA) allowing for studying the relationship between TGFs and optical phenomena [Neubert T. et al., 2019].

With only gamma ray data it is only possible to infer the approximate radial distance of the TGF from the spacecraft. Using lightning location networks such as World Wide Lightning Location Network (WWLLN) and Vaisala's Global Lightning Dataset (GLD) it is possible to identify Very Low Frequency (VLF) sferics associated with TGFs [Connaughton V. et al., 2010]. This makes it possible to narrow down the location of associated TGFs to within a couple of km of the sferic. This method is also applicable to TGFs that are associated to optical emissions from lightning [Stanbro et al. 2018].

The objective of this thesis is to investigate the characteristics of multi pulse TGFs in different regions on Earth. Furthermore, to investigate the relation between multi pulse TGFs, optical and radio signals from lightning.
We start by identifying multi pulse TGFs from ASIMs MXGS High-Energy Detector (HED). For events with optical data the image from the Camera Head Unit (CHU) at the time of the TGFs is projected onto a map to determine the distance of the optical signal to ASIMs footpoint. A consistency check is then preformed by inspecting the characteristics of the TGFs and the location of any optical or radio pulse to determine if they are likely to be associated with the TGFs.

This thesis consists of five major parts:
Chapter 2 presents a brief summary of the theory behind lightning, TGFs and multi pulse TGFs. In chapter 3 we present the instruments used in the thesis. Chapter 4 presents the methods used to identify TGFs, the procedure to map the optical images and the consistency check used to identify likely associated radio and optical pulses. Chapter 5 presents the multi pulse TGFs identified, and their characteristics. Chapter 6 discusses the results of the thesis.

Chapter 2

Background

This chapter will focus on the theoretical background necessary to help understanding this thesis. This includes how clouds are formed, the process of cloud electrification, the processes of lightning discharge, and the production mechanisms of terrestrial gamma-ray flashes. As not all of these processes are fully understood, this section will focus on the current leading theories in regards to each subject. Since thunderclouds and lightning are not the main topic of this thesis, this section will only provide a basic overview of each topic. More details can be found in [William H. B.], [Cooray V., 2003] and [Dwyer et al., 2012].

2.1 Cloud Formation

A useful concept when talking about cloud formation is water vapor pressure e. Water vapor pressure is a measure of how much pressure is exerted by water vapor in the air. If the water vapor pressure becomes too large at some point the water vapor will begin to condense into water droplets. This threshold value is called the saturation vapor pressure e_s and is dependent on the temperature of the air. The ratio of the water vapor pressure e and the saturation vapor pressure e_s is known as the saturation of air $s = \frac{e}{e_s}$ and is used as a measure of the humidity of air. The condition when water vapor begins too condense is known as supersaturation and happens when $s \geq 1$.

Cloud formation occurs when a volume of air reaches the supersaturation condition. This commonly occurs when a warm parcel of air which is subsaturated ($s < 1$) is lifted into the atmosphere and cools by adiabatic expansion. This lifting process can happen by either the air parcel moving into a horizontal pressure gradient, like a mountain. Which causes the air parcel to be pushed upwards. Or by the sun heating the Earth's surface which in turn heats the air. This heating then increases the buoyancy of the air and causes it to rise. When this occurs the air parcel rises fast enough that there is little or no heat transfer between the parcel and the surrounding air. As the air parcel rises the pressure in the atmosphere drops, so the water vapor pressure e also decreases. However since the pressure decreases the air parcel expands in volume which in turn makes the temperature of the air parcel decrease.The saturation vapor pressure e_s is heavily dependant on temperature and decreases faster than the water vapor pressure e. Eventually the water vapor pressure e becomes larger

than the saturation vapor pressure e_s and the air parcel reaches supersaturation. The height at which this occurs is known as the lifted condensation level (LCL). The air parcel continues to rise and condense until the temperature of the air parcel reaches equilibrium with the air surrounding it, at which the cloud has been fully formed [William H. B.].

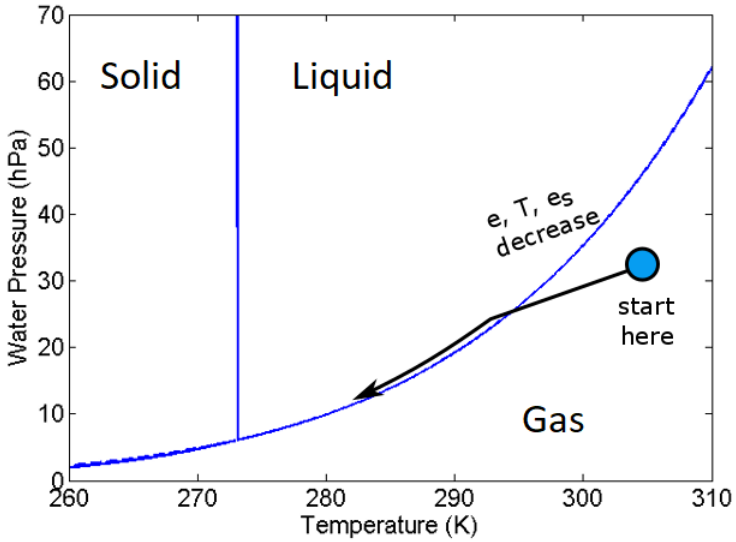

Figure 2.1: Water phase diagram, as the air parcel moves upwards to lower pressure the water vapor pressure e (y-axis) decreases but so does the temperature (x-axis) until the water vapor pressure e becomes larger than the saturation vapor pressure e_s (indicated by the blue line) and a cloud forms. The air parcel continues to rise and condensate so that the water vapor pressure e follows along the saturation vapor pressure e_s curve, until the air parcel reaches equilibrium temperature with the surrounding air. Figure from William H. B..

2.2 Cloud Electrification

Not all clouds are capable of producing lightning.
Clouds typically occur with the LCL within 1000 meters of the Earth's surface, at this height the temperature is typically well above freezing and as a consequence most clouds consist almost entirely of liquid water droplets.
Typical conditions for clouds capable of lighting production are tall clouds with a Thickness greater than 3-4 kilometers where the clouds are at least 2-3 kilometers into the subfreezing portion of the atmosphere. The $0°C$ isotherm typically lies at 4-5 kilometers above the Earth's surface. Lightning generally occurs in regions of high precipitation, when the cloud has a strong convective activity and most essentially when the cloud contains both ice and supercooled water [Cooray V., 2003].

2.2.1 Graupel-Ice Mechanism

The current leading theory for electrification of clouds is the graupel-ice mechanism. Graupel are larger ice particles that form when a supercooled water droplet comes into contact with an ice crystal and freezes onto it in a process known as accretion. When several water droplets freeze onto an ice crystal in this way it results in a larger sphere like ice crystal forming, which is known as a graupel. As illustrated in Figure 2.2 when a graupel collides with a smaller ice particle a charge transfer happens between the graupel and the ice particle, the polarity of the charge transfer has been shown to be dependent on temperature, water content and the supercooled droplet size. The temprature at which the polarity of the charge transfers changes is known as the reversal temperature T_R. At a typical supercooled droplet sizes there is only one reversal temperature, which varies between $-10°C$ to $-20°C$ depending on the cloud water content. Lower cloud water content leads to a higher reversal temperature. In typical conditions the graupel will be negatively charged in collisions at temperatures lower than T_R and positively charged at temperatures higher than T_R [Cooray V., 2003].

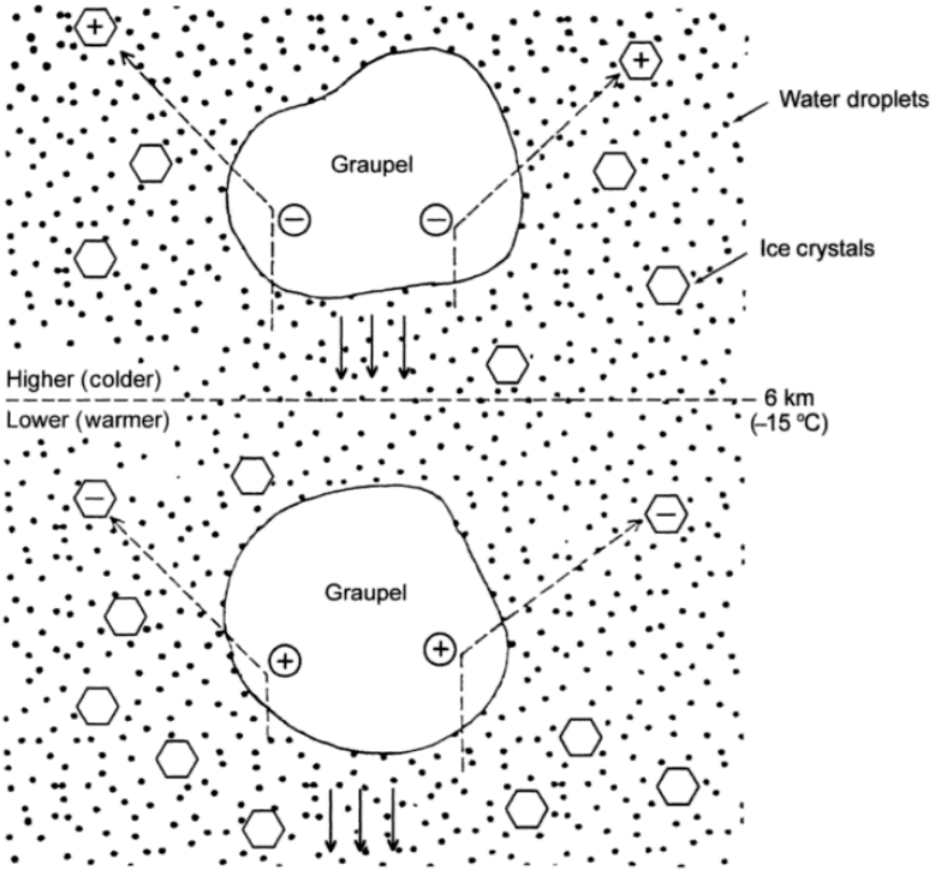

Figure 2.2: Illustration of graupel-ice mechanism. The reversal temperature T_R here is shown to be at $-15°C$ at 6 km. The graupel above 6 km where $T < T_R$ become negatively charged when colliding with ice crystals, while the graupel below 6 km where $T > T_R$ become positively charged. The graupel due to their larger mass then sink which causes a gravity induced separation of charge within the cloud. Figure from Rakov and Uman [2003].

Since the graupels have a high mass they fall downwards in the cloud while the lighter surrounding ice particles and water droplets move upwards due to updrafts. This means that at the bottom of the cloud where temperatures are higher than T_R the graupel become positively charged and create a positive charge center towards the bottom of the cloud, while the lighter particles rise upwards and create a negative charge center towards the middle of the cloud. While in the upper part of the cloud where temperatures are lower than T_R the graupel become negatively charged and sink towards the middle of the cloud converging with the negative ice and water droplets going upwards from the bottom of the cloud, while the lighter positively charged particles rise to the top of the cloud forming a positive charge center at the top. The full effect is that two positive charge centers are formed at the top and bottom, with a negative charge center in the middle of the cloud, as shown in Figure 2.3. In cases with smaller supercooled droplet sizes it is possible to get multiple reversal temperatures which could explain more complex charge distributions found in clouds as shown in Figure 2.4 [Cooray V., 2003].

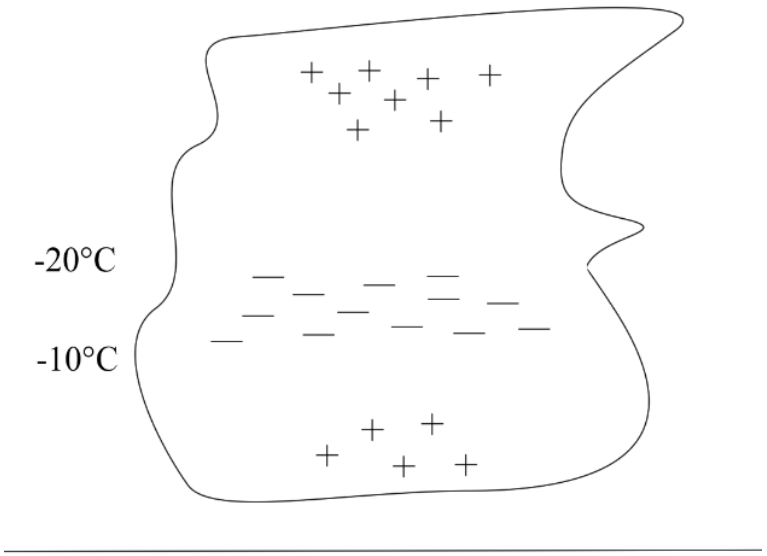

Figure 2.3: Common tripole structure of a thundercloud, the main negative charge tends to be located between the temperature range of $-10°C$ to $-20°C$.

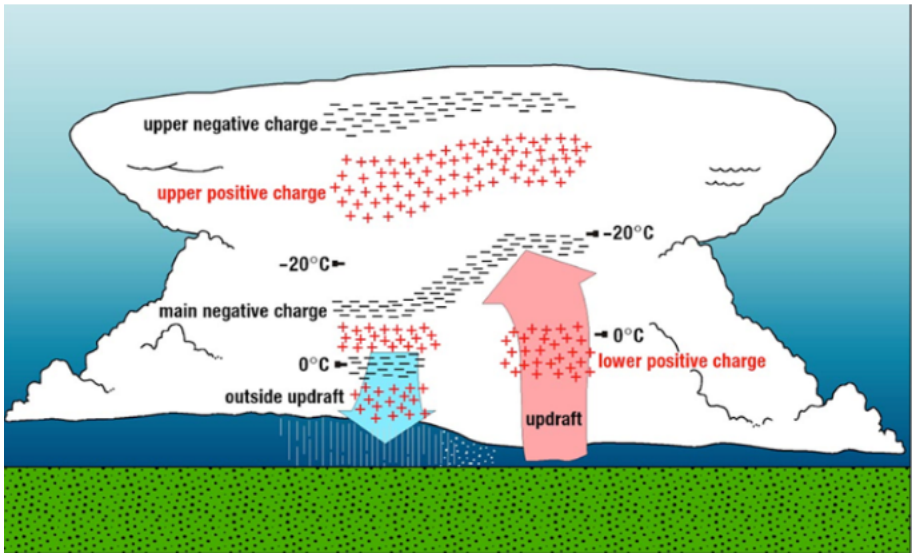

Figure 2.4A more complex charge structure in a thundercloud. Figure from Stolzenburg et al. [1998].

2.3 Lightning discharge

For any lightning to occur the electrical field within a cloud must be large enough that electrical breakdown occurs. Electrical breakdown is when the rate of ionization in the air becomes larger than the rate of deionization, this occurs when the electric field is above $30kV/cm$ which is termed the conventional breakdown field, marked E_k in Figure 2.5. Under these conditions there will be a growing population of free electrons in the air, which makes the air turn from an insulator to a conductor [Cooray V., 2003].

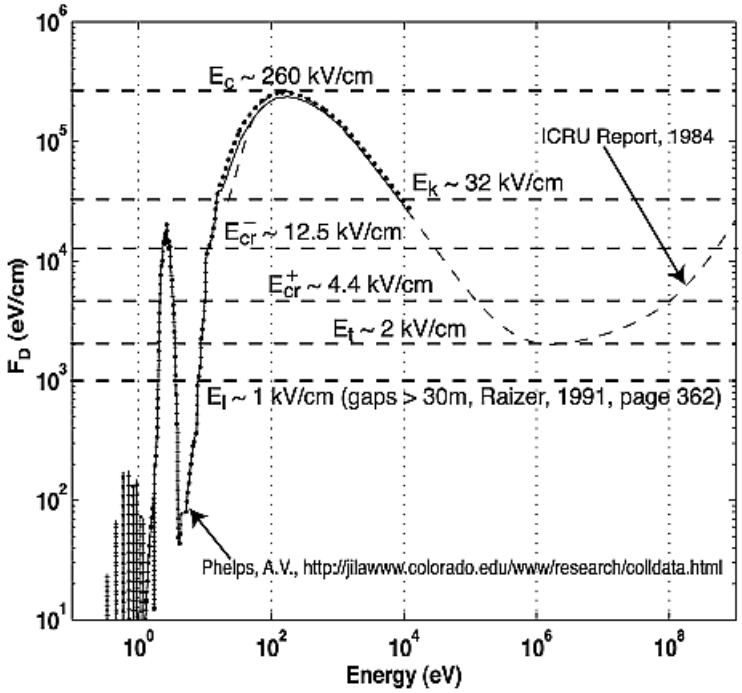

Thermal Runaway:	$E_c \sim 260$ kV/cm	Positive Streamer:	$E_{cr}^+ \sim 4.4$ kV/cm
Conventional:	$E_k \sim 32$ kV/cm	Relativistic Runaway:	$E_t \sim 2$ kV/cm
Negative Streamer:	$E_{cr}^- \sim 12.5$ kV/cm	Leader:	$E_l \sim 1$ kV/cm

Figure 2.5: Friction force on electrons in air at ground pressure as function of electron energy. The dashed horizontal lines represent the electric field threshold energies for different processes to occur. For electrical breakdown to occur the force of the electrical field has to be larger than the first peak of the friction force which is around $30kV/cm$. An electric field at this value is able to accelerate all free electrons up to energies of the order 10^1eV. Figure from Moss et al. [2006].

2.3.1 Thermal Electron Avalanche

All discharges begin with a thermal electron avalanche. A thermal electron avalanche can occur when a free electron is present within a electric field. The electron will accelerate towards the positive charge center and if the energy of the electron becomes larger than the ionization energy of air $\sim 12 - 16eV$, The electron can inelastically collide with a atom or molecule in the air and ionize it. This collision then results in two free electrons which can then collide again and ionize more air particles, which in turn creates more free electrons. The resulting chain produces what is known as a thermal electron avalanche. As a thermal electron avalanche grows it accumulates more and more electrons which in turn creates a negative electric potential, when the electric field generated by an avalanche becomes locally comparable with the background electric field, a streamer can form [Cooray V., 2003].

2.3.2 Streamers

There are two types of streamers; positive as seen in Figure 2.6 and negative as seen in Figure 2.7. A positive streamer occurs when a thermal electron avalanche collides with a positive charge center, the electrons from the avalanche are absorbed by the positive charge center but the avalanche leaves behind a trail of positive ionized particles. This positive ion trail is known as the head of the streamer. When another avalanche hits the streamer head, the positive ions in the head absorb and neutralize the electrons from the avalanche, however this second electron avalanche also has a positive ion trail, which then becomes the new streamer head. This process repeats as the head propagates towards the negative charge center. For positive streamers the electric field required for continuous propagation is $E_{cr}^{+} \sim 4.4kV/cm$ as seen in Figure 2.5 [Cooray V., 2003].

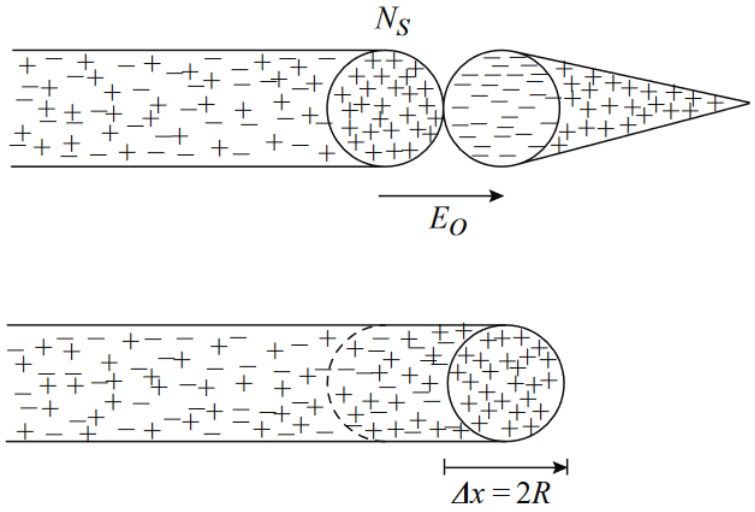

Figure 2.6: Propagation of positive streamer. As the positively charged streamer head is hit by an electron avalanche, the streamer propagates towards the direction of the initial avalanche electron. While the head of the streamer is positively charged, the streamer trail remains neutral. Figure from Cooray V. [2003].

A negative streamer occurs when a thermal electron avalanche starts near a negative charge center, the electrons from the avalanche move towards the positive charge center and leave behind a positive ion trail. This ion trail then becomes attracted towards the negative charge center and gets absorbed and neutralized. This leaves behind the electrons from the electron avalanche as the streamer head. When another avalanche occurs near this streamer head, the electrons become attracted towards the positive ion trail left behind by the next avalanche and neutralize them. This leaves behind the electrons from the second avalanche as the new streamer head. This process repeats as the head propagates towards the positive charge center. For negative streamers the electric field required for continuous propagation is $E_{cr}^{-} \sim 12.5kV/cm$ as seen in Figure 2.5, which is about three times higher than the electric field required for continous propagation of positive streamers at $E_{cr}^{+} \sim 4.4kV/cm$.

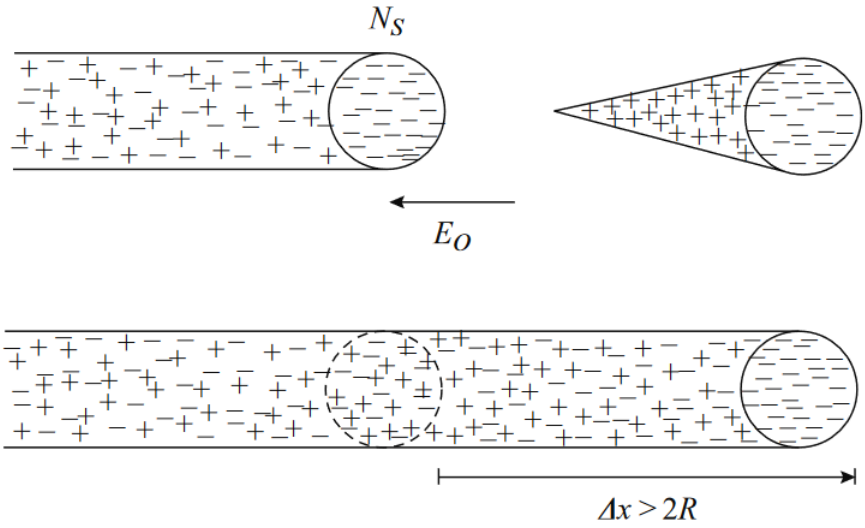

Figure 2.7: Propagation of negative streamer. As the negatively charged streamer head is attracted towards the positive ion trail of the avalanche ahead, the streamer propagates towards the direction of the successive electron avalanches. The head of the streamer is negatively charged, while the streamer trail remains neutral. Figure from Cooray V. [2003].

2.3.3 Leaders

Due to the streamer trail not being particularly ionized, streamers on their own are only weakly conductive. However if multiple streamer trails overlap in a common streamer stem the commutative current of each streamer will heat the air. If the temperature increase is sufficient enough then the gases in the stem will expand which in turn increases the rate of ionization versus the rate of deionization, this causes the stem to become a hot, highly ionized and highly conductive channel called a leader. Unlike streamers which are typically only a couple of mm to cm long a leader can be hundreds of meters to kilometers long and is the part of the lightning that is visible to the naked eye. Due to the high conductivity of the leader most of the voltage from the charge center will be transferred into the leader, resulting in a high electric field in the head of the leader. This in turn causes streamers to be produced from the head of the leader, which causes a new common stem to occur at the head of the leader. The new stem will then become a new leader section, and in this way the leader will begin to propagate towards the charge center of opposite polarity.

When a leader comes near the charge center of opposite polarity, due to the electric field from the leader a connecting leader may form. This connecting leader propagates from the opposite polarity center towards the leader. When the leaders meet a discharge will occur, as the charge gathered in the charge centers travel through the leaders [Cooray V., 2003].

2.4 Terrestrial Gamma-ray Flashes (TGFs)

TGFs where first reported by Fishman et al. [1994] and consist of sub-millisecond bursts of X-ray photons emitted from thunder clouds. While the exact production mechanism of TGFs are not know it is generally agreed that TGFs are caused via bremsstrahlung of energetic electrons known as run-away electrons being accelerated in the electric fields within cloud structures. [Dwyer et al., 2012]

2.4.1 Runaway Electrons

If an electron has a high enough kinetic energy and is placed within a strong enough electric field then a runaway electron might occur. Runaway electrons happen when the Coulomb force on an electron is larger than the friction force the electron experiences due to interactions with the air. When this happens the electron will increasingly gain energy from the electric field and "run away". The friction force of the electron is dependent on the electrons kinetic energy and runaway electrons can only occur if the force from the electric field is larger than the minimum value of the friction force. This value is known as the break even field eE_b marked as E_t in Figure 2.5, where $E_b = 2.18 \times 10^5 V/m \times n$ and n is the density of air with respect to sea level. If the electric field is larger than the break even field then runaway electrons can occur, but not for all electrons. The friction force has a peak at low kinetic energies, this leads to electrons with initial low kinetic energy being accelerated until the friction force becomes equal to the Coulomb force and thus the electrons can not run away. However at higher kinetic energies the frictional force decreases, meaning that any electron with an initial kinetic energy larger than ε_{th} will become a runaway electron [Dwyer et al., 2012].

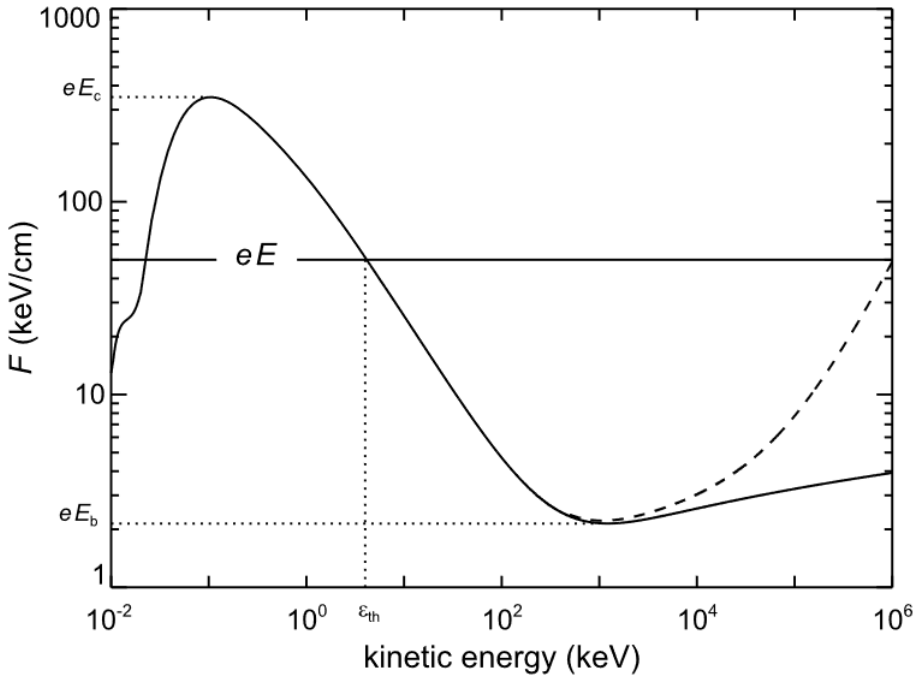

Figure 2.8: Graph showing the frictional force experienced by a free electron. The solid curve shows the frictional force due to inelastic collisions, while the dashed line shows the effects of bremsstrahlung emission. The solid line eE indicates the force due to an electric field with a field strength of E, ε_{th} is the corresponding minimum kinetic energy an electron needs to become a runaway electron. The value E_b is the break even field and is the minimum value that runaway electrons could theoretically occur. The value E_c is the critical field strength and indicates the minimum electric field for thermal runaway to occur. Figure from Dwyer et al. [2012].

2.4.2 Relativistic Runaway Electron Avalanche (RREA)

If electrons had traveled exactly along the electric field lines then the break even field would be the minimum threshold value for runaway electrons. However elastic scattering will cause deviation in the electron trajectories so they do not travel exactly along the field lines Simulations taking into account this elastic scattering have shown that the electric field required for runaway electrons to occur is actually about $\sim 30\%$ higher than the break even field. This value is known as the threshold field $E_{th} = 2.84 \times 10^5 V/m \times n$ and is comparable to the maximum electric fields observed within thunderclouds, which might suggest a possible connection between lightning initiation and runaway electron production. Another effect of taking elastic collisions into account are relativistic runaway electron avalanches RREA. Electrons with an initial kinetic energy larger than ε_{th} are known as seed electrons and may occur due to cosmic-rays or radioactive decay. When a seed electron Møller scatters (electron-electron elastic scattering) with another electron it is possible that both electrons wind up with higher energy than the runaway threshold energy ε_{th}. In this case both electrons will then be accelerated as runaway electrons and can again collide and cause more runaway electrons to occur. The resulting avalanche of electrons is a RREA [Dwyer et al., 2012].

2.4.3 Production and propagation of gamma-rays

Bremmstrahlung is the process when an energetic electron becomes deflected by a charged particle, commonly a nuclei of an atom or molecule which causes the energetic electron to decelerate and lose kinetic energy, due to conservation of energy the kinetic energy lost by the energetic electron is converted into a photon. Bremmstrahlung can occur due to any charged particle decelerating however most commonly occur with electrons due to being the lightest of all charged particles. A process such as a RREA will emit a large amount of energetic electrons which will primarily interact with the atoms or molecules in the air via bremsstrahlung and emit a spectrum of X-rays with energies towards the kinetic energy of the runaway electrons. The emitted X-rays can then propagate much further through the atmosphere than the electrons and can cause further interactions with the air [Dwyer et al., 2012].

The three important interactions of X- and gamma-rays with air are: pair production, Compton scattering and photo-electric absorption.
At energies above a few MeV pair production is the dominating interaction, pair production is when a photon with an energy above $1.022MeV$ interacts with a particle or nucleus and transforms its energy into a positron electron pair. For photons between 100 keV to a few MeV Compton scattering is the dominating interaction. Compton scattering is an elastic interaction between a photon and a charged particle, where the photon transfers a part of it's energy to the charged particle and is scattered. Photons tend to scatter several times before their energy reaches below 100 keV, where photo-electric absorption is the dominating interaction. Photo-electric absorption is an inelastic interaction between a photon and a charged particle, where the photon transfers all of its energy to the charged particle [Dwyer et al., 2012].

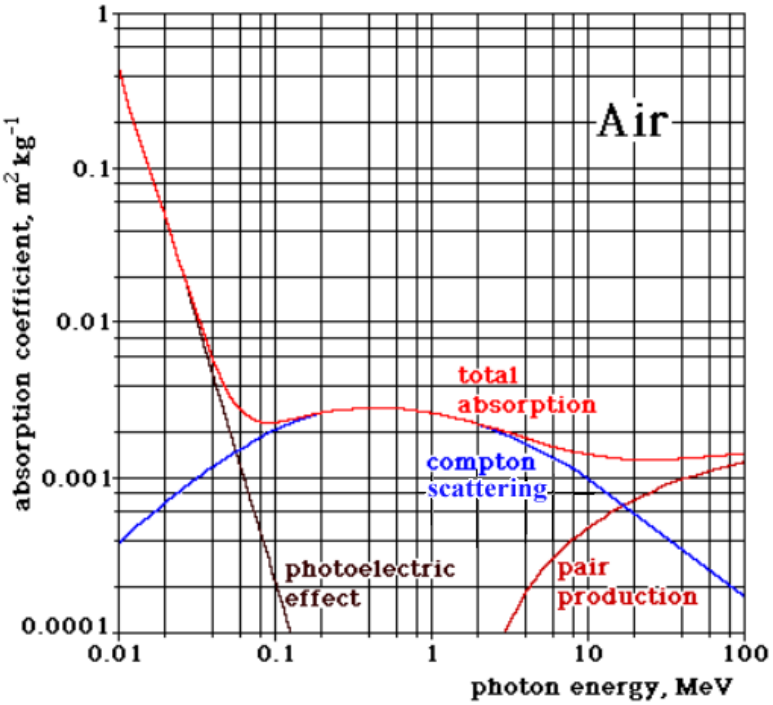

Figure 2.9: Cross section of photon interactions by energy in air. For energies above a few MeV pair production is the dominating interaction, from $\sim 100keV$ to a few MeV Compton scattering is dominating and below $\sim 100keV$ photoelectic effect dominates.

2.4.4 Relativistic Feedback

When a seed electron in an electric field above the threshold field E_{th} initiates a RREA, a large number of energetic X-rays and gamma-rays are produced. If any gamma-ray pair produces a positron, the positron has opposite charge of the electron it will be accelerated by the electric field back towards the source region of the seed electron. Since the positron annihilation cross-section decrees with energy, any positron that is not immediately annihilated will quickly accelerate to tens of MeV and will be able to travel kilometers before being annihilated. It is then possible for these positrons to create more runaway electrons via hard elastic scattering (Bhahba scattering) which can then cause a secondary RREA to occur.

Additionally if any X-rays Compton scatter it is possible that the X-rays are scattered back towards the original direction they came from. The X-rays can then create more runaway electrons either via Compton scattering or by photo-electric absorption. These runaway electrons can then initiate another RREA.

Any RREA generated by either a positron backscattering or an X-ray Compton backscattering can then initiate any of these processes again. Thus, under the right conditions a single electron seed can cause en exponential amount of RREAs to occur within a couple of microseconds. This process of exponential RREAs is known as relativistic feedback [Dwyer et al., 2012].

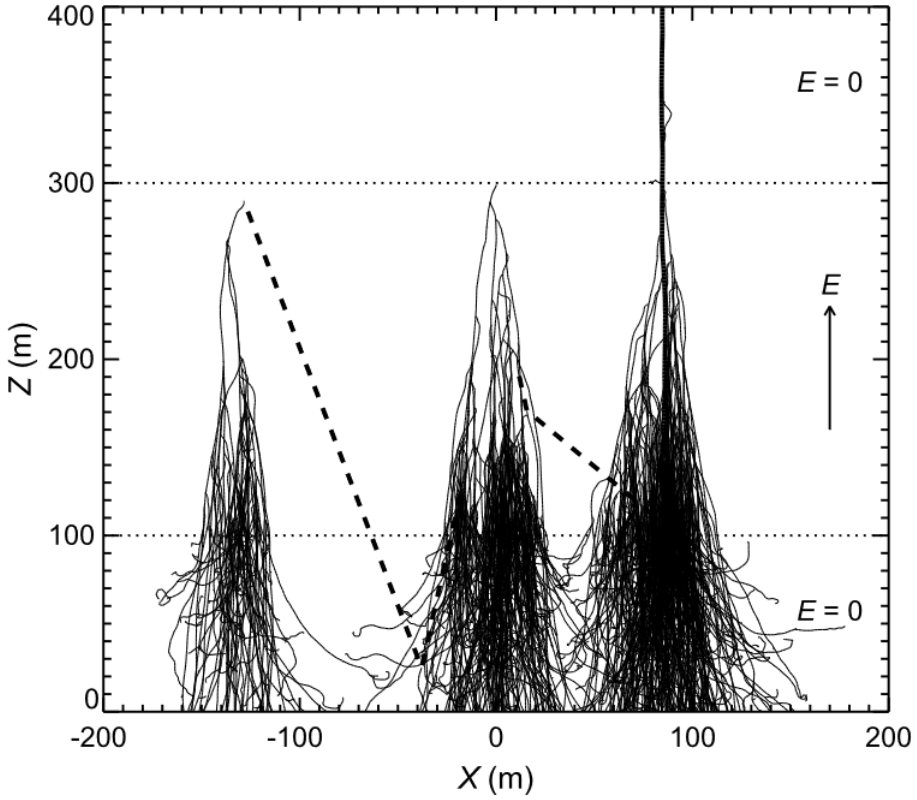

Figure 2.10: Monte Carlo simulation of relativistic feedback mechanism. The dark lines show electons, the dashed lines are X-rays and the dark solid line to the right is a positron. The simulation starts with an initial electron seed which starts at x=0, z=300. The horizontal dotted lines show the boundaries of the electric field. Figure from Dwyer [2013].

2.4.5 TGF production

The amount of energetic electrons created from RREA $\sim 10^3 - 10^5$ are not enough to explain the amount of energetic electrons in TGFs $\sim 10^{17}$. There are two ways to make sufficient runaway electrons necessary for a TGF:

1. Thermal runaway electrons, that go through RREA multiplication
2. Relativistic feedback

The thermal runaway process occurs if the force from the electric field is larger than the maximum value of the friction force. This occurs if the electrical field is above the critical field value E_c as seen in Figure 2.5 and Figure 2.8, and causes all free electrons in the electric field to become runaway electrons. The critical field can be reached in the streamer zone and can give 10^{12} runaway electrons produced in $\sim 1\mu s$. If these electrons then go through RREA multiplication, 10^{17} energetic electrons can be reached [Carlson et al., 2009].

The mechanism known as relativistic feedback as described in 2.4.4 was first proposed by Dwyer [2003] and can increase the amount of energetic electrons from a RREA $\sim 10^3 - 10^5$ by a factor of $\sim 10^{13}$ for a total of $\sim 10^{16} - 10^{18}$.

Thermal runaway process is tightly connected to leader propagation and occurs in the leader tips while relativistic feedback can work in both leader fields and in large scale electric fields within the thundercloud. Relativistic feedback requires an minimum electric field of about $\sim 4kV/cm$ over a large volume (Figure 2.11), while the thermal runaway process requires the critical field $E_c = 260kV/cm$ to be reached in a streamer [Carlson et al., 2009] Dwyer [2003].

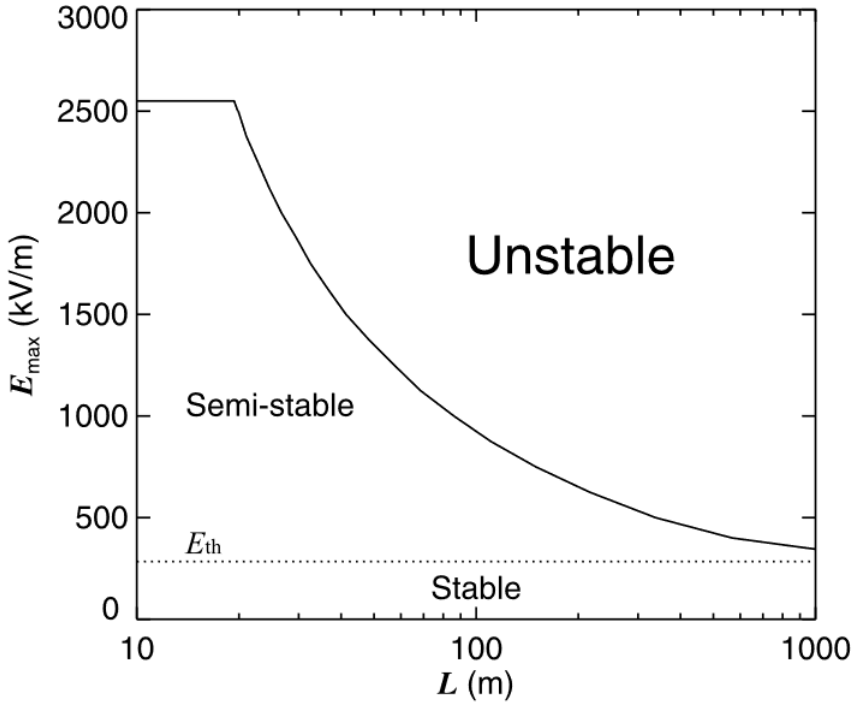

Figure 2.11: Electric field necessary to sustain relativistic feedback E_{max} as a function of electric field region L, at 1 atm. The horizontal dotted line shows the threshold field E_{th} necessary for runaway electrons Dwyer [2003].

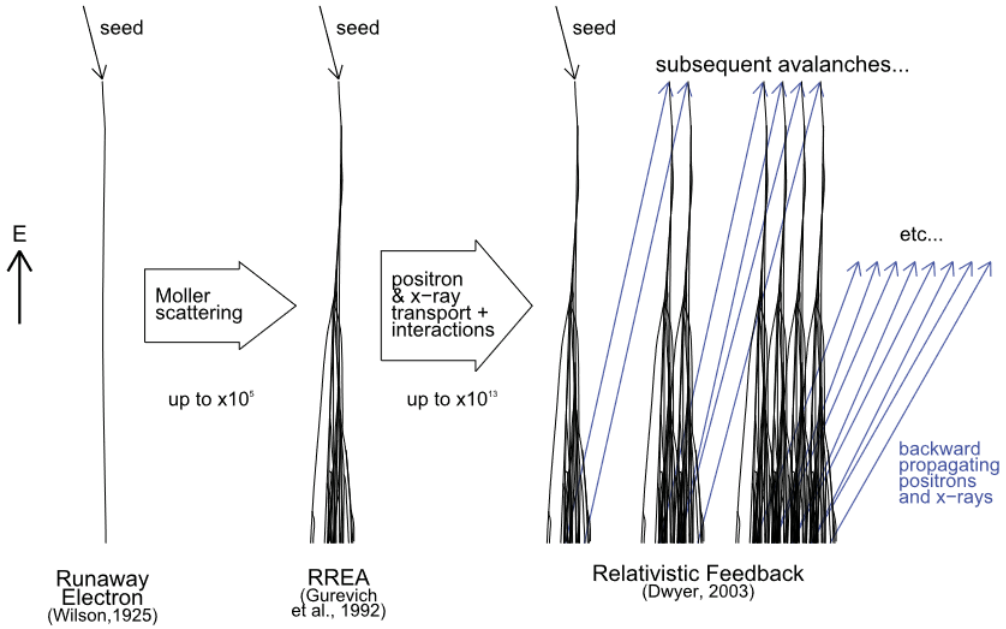

Figure 2.12: Diagram showing how the relativistic feedback mechanism builds upon relativistic runaway electron avalanches, which builds upon runaway electrons. The relativistic runaway electron avalanche mechanism is created by introducing elastic electron collisions (møller scattering) in the runaway electron mechanism and results in about 10^5 more runaway electrons compared to the runaway electron mechanism. The relativistic feedback mechanism is created by introducing X-rays interactions to the RREA mechanism and results with another increase of up to 10^{13} more runaway electrons than RREA mechanism. Figure from Dwyer et al. [2012].

2.4.6 Multi Pulse Terrestrial Gamma-ray Flashes

In some instances Multiple TGFs can occur within the same thunder cell within hundreds of μs to a couple of ms apart, these cases are known as multi pulse terrestrial gamma-ray flashes. Multi pulse TGFs where first reported by BATSE in 1994 in the same paper that reported on the discovery of TGFs [Fishman et al., 1994]. Since then Multi pulse TGFs have been reported by several space missions including RHESSI, Fermi, AGILE and ASIM.

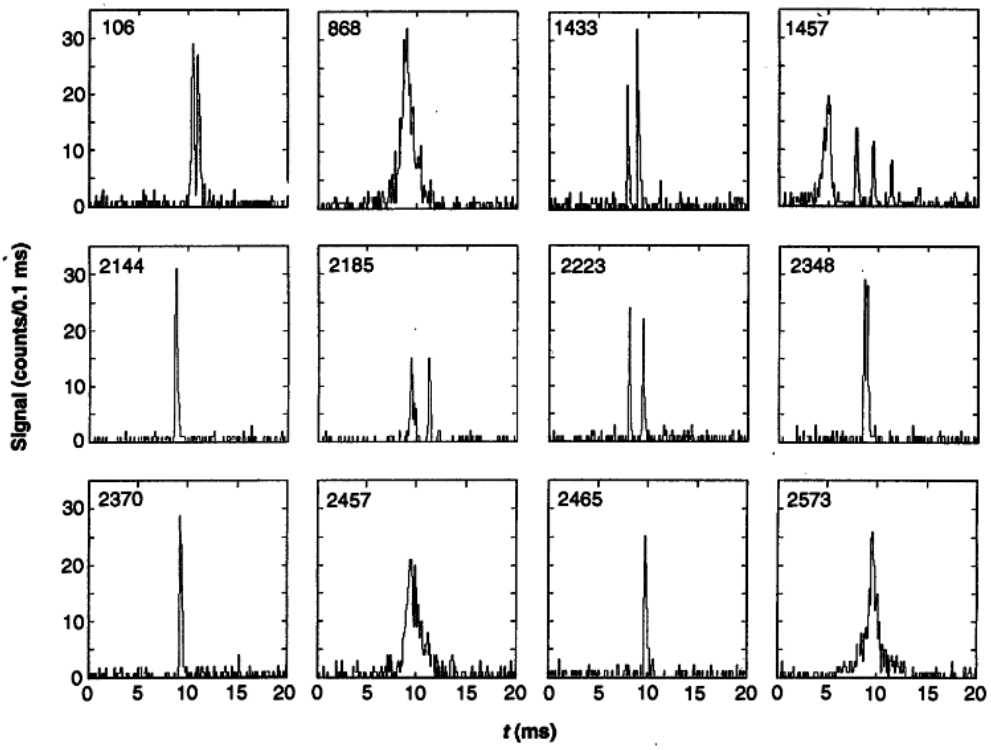

Figure 2.13: TGFs from BATSE, of which several are multi pulse TGFs. Figure from [Fishman et al., 1994].

The current consensus in regards to TGFs it that they are caused by bremsstrahlung from electron cascades known as RREA caused by strong electric fields within the atmosphere, however the precise location of the electric field is still contested [Stanbro et al., 2018]. There are two general models in regards to the high-potential electrical fields position [Foley et al., 2014].

The lightning leader emission model assumes that electron acceleration occurs by the cold runaway process from electric fields at the tip of the leader. In this scenario the electric field at the streamer tip becomes larger than E_C (see Figure 2.5) so that all electrons inside of the field are able to become runaway electrons, which will then go through RREA multiplication. In this model multi pulse TGFs are a result of multiple RREA occurring at different times during leader progression through the cloud [Carlson et al., 2009] [Celestin & Pasko, 2011].

The second model is the relativistic feedback discharge model, in which the electron acceleration occurs in either leader fields or large scale electric fields inside of the cloud. In this scenario the TGF is caused by a seed electron creating a RREA which causes relativistic feedback through the generation of backward propagating runaway positrons and backscattered X-rays. If the potential difference in the avalanche region is large enough a self-propagating discharge known as a relativistic feedback streamer can occur. The relativistic feedback streamer propagates in a pulsed fashion producing a TGF with each propagation, which results in the observation of a multi pulsed TGF [Dwyer, 2012].

A paper by Stanbro et al. [2018] looked into consecutive TGF pulses using the Fermi Gamma-ray Burst Monitor and found that there was a significant lack of TGFs with a time separation between 10ms and 1s Figure 2.14. The paper interpreted this gap as showing differing origins of the TGFs. With the TGFs with a time separation smaller than 10ms being single TGFs with multiple pulses, while the TGFs with a time separation larger than 1s being from consecutive individual TGFs.

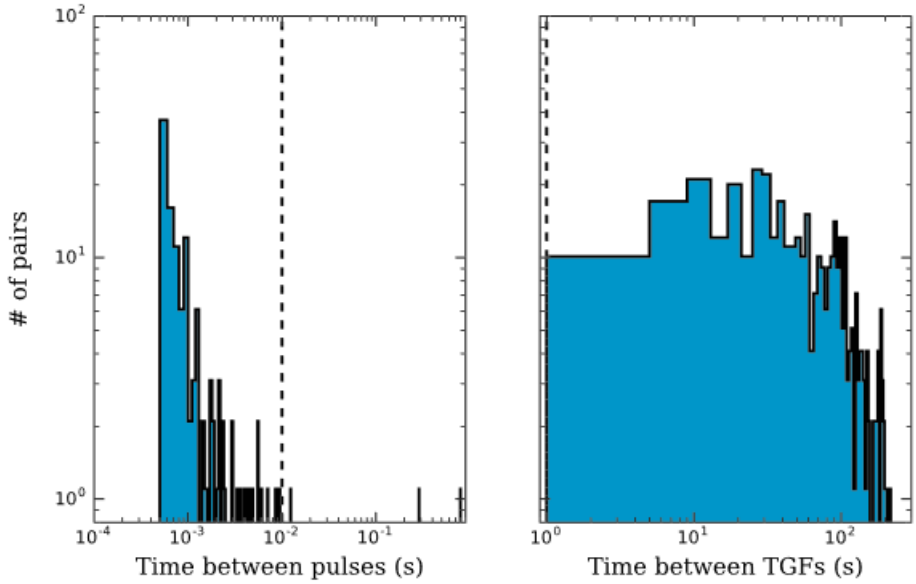

Figure 2.14: Separation time between TGFs, left plot has 10 μs binning and shows separation times lower than 1s. Right plot has 1 s binning and shows separation times above 1s. Figure from Stanbro et al. [2018].

Several papers [Mezentsev et al., 2016][Lindanger et al., 2020][Mailyan et al., 2020] have looked into VLF sferics associated with multi pulse TGFs.

Mezentsev et al. [2016] looked at multi pulse TGFs from RHESSI and found that all VLF sferics were always associated with the last TGF pulse. Lindanger et al. [2020] found that multi pulse TGFs from AGILE agreed with Mezentsev et al. [2016] findings that VLF sferics where always associated with the last pulse in a multi pulse TGF. Mailyan et al. [2020] looked at multi pulse TGFs from Fermi Gamma-ray Burst Monitor and also found that all multi pulse TGFs with associated VLF sferics always had a VLF associated with the last TGF pulse, however unlike the previous two studies several double pulse TGFs had VLF sferics associated with both pulses.

Mezentsev et al. [2016] gives three possible explanations for the phenomena. First is that WWLLN is more likely to detect the last sferic in a sequence of VLF pulses due to instrumental issues. Second is that the VLF signal associated with the TGF pulses might be too weak to observe, and the sferic observed occurs due too the recoil current from the leader propagating to the opposite charge center. In this case early pulses of multi pulse TGFs occur in association with the steps of the lightning leader, while the last pulse is associated with the leader propagating into the opposite charge center and

so the last pulse will be associated with a much stronger VLF sferic. The third explanation is that during leader progression, some leader steps may be non-vertical. A TGF emitted during such a step would still be detectable by a spacecraft, however due to the angle the VLF signals emitted would be harder to detect for ground stations. A later pulse then traveling vertically would be detectable by ground stations. However as pointed out by Mailyan et al. [2020], it is not evident why the last pulse is more likely to be produced by a vertically traveling leader. Mailyan et al. [2020] points out that current models cannot explain the lack of correlation between radio and gamma-ray intensities observed for some TGFs.

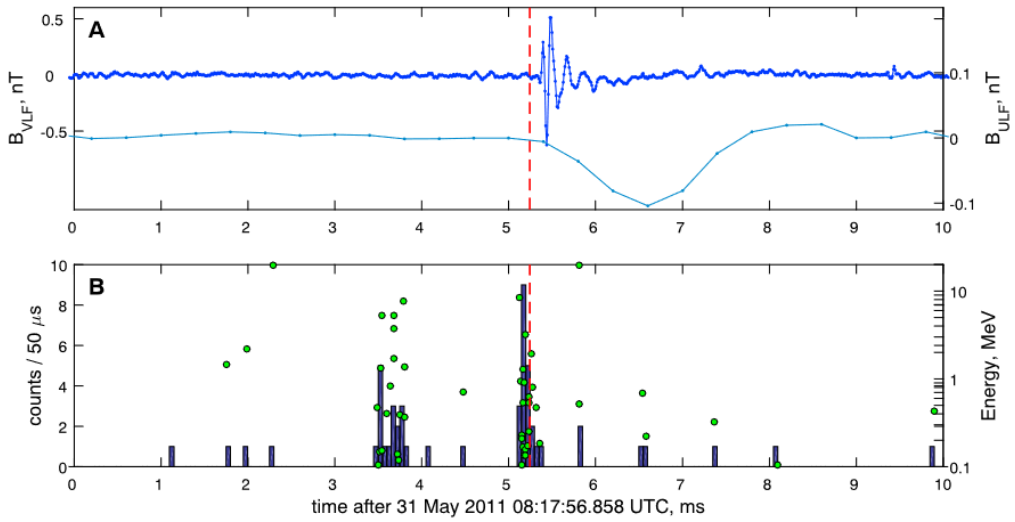

Figure 2.15: VLF signal associated with last TGF pulse in a multi pulse TGF. Figure from Mezentsev et al. [2016].

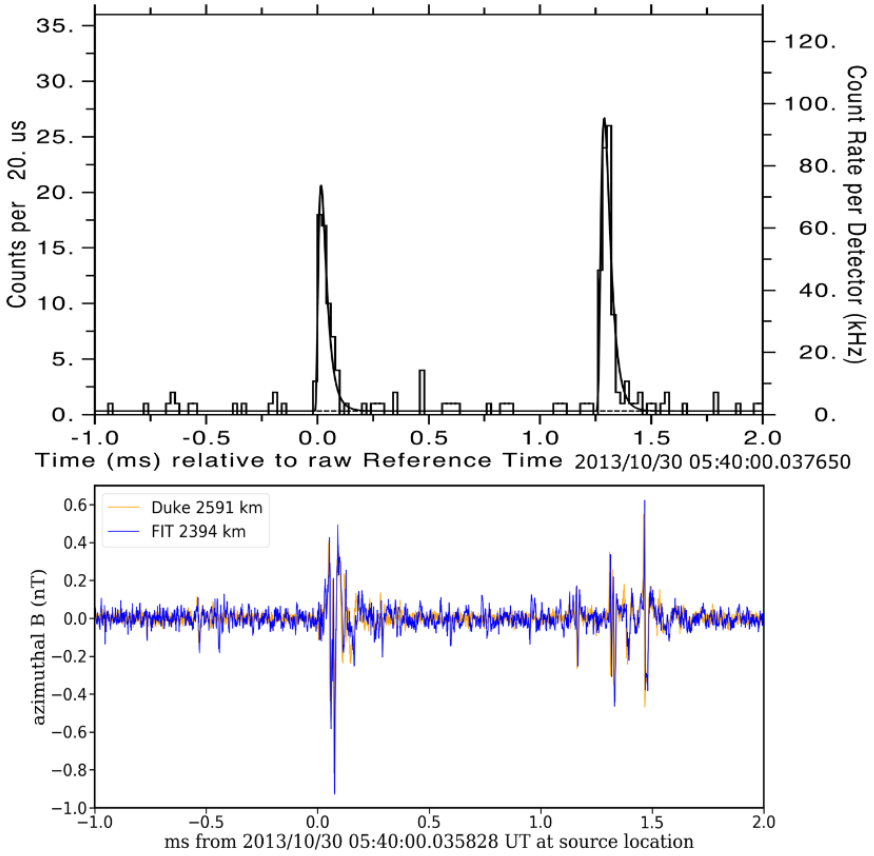

Figure 2.16: VLF signal associated with both pulses in a multi pulse TGF. Figure from Mailyan et al. [2020].

Chapter 3

Data

This chapter will cover the instruments used in this thesis.

3.1 ASIM

The Atmosphere-Space Interactions Monitor (ASIM) payload includes two main instruments the Modular Multispectral Imaging Array (MMIA) and the Modular X- and Gamma-Ray Sensor (MXGS). ASIM is mounted onto the side of Columbus module on the International Space Station (ISS), with MXGS facing towards nadir and MMIA facing a 5 degree angle starboard from nadir.

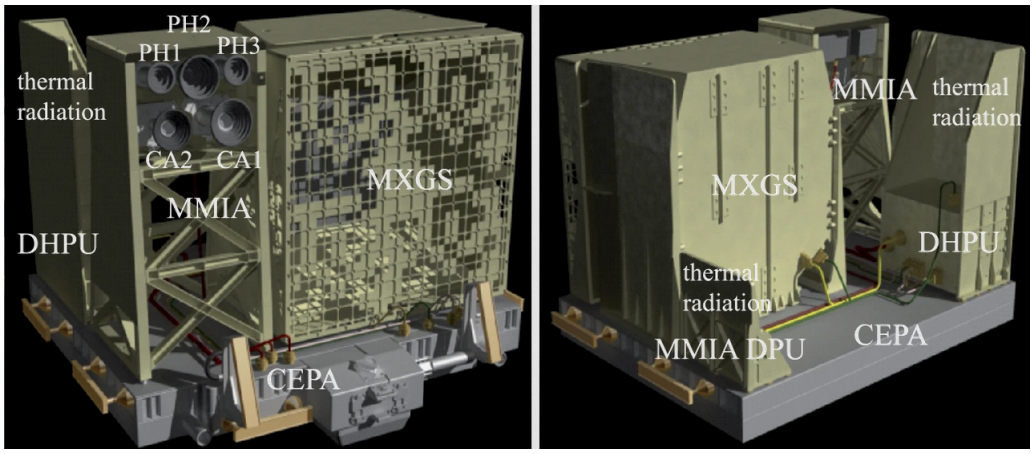

Figure 3.1: The ASIM payload mounted onto the Columbus External Payloads Adaptor (CEPA). The main instruments MMIA and MXGS are located at the front, with the MMIA Data Processing Unit (DPU) and the Data Handling and Power Unit (DHPU) at the back. Figure from Neubert et al. [2019]

3.1.1 MMIA

MMIA [Chanrion et al., 2019] consists of two imaging cameras (Camera Head Unit, CHU) in 337 nm and 777.4 nm, and three photometers at 180-230 nm, 337 nm and 777.4 nm.

CHU	337 nm	777.4 nm
Sampling Rate	12 Hz	
Temporal resolution	>83 ms	
Bandwidth	4 nm	3 nm
FoV	Square 80° over diagonal	
Resolution	1024x1024	
Spatial Resolution (at 400 km)	$\sim$ 400 x 400 m at center of FoV	

Table 3.1: CHU specifications

Photometer	180-230 nm	337 nm	777.4 nm
Sampling Rate	100 kHz		
Temporal resolution	10 μs		
Bandwidth	-	4 nm	5 nm
FoV	Circular 80°	Square 80° over diagonal	

Table 3.2: Photometer specifications

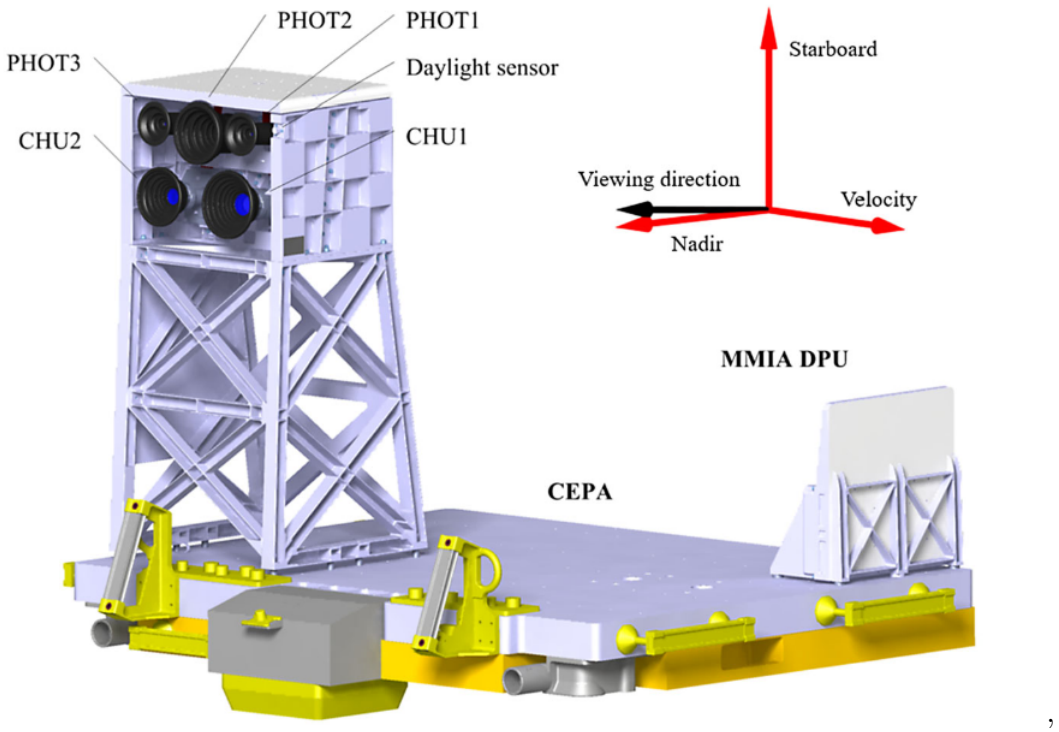

Figure 3.2: MMIA mounted onto the Columbus External Payloads Adaptor (CEPA). The MMIA instruments consisting of three photometers and two camera head units are mounted onto a support structure to avoid having the nadir-directed platform in the FoV. The instruments are tilted with an angle of 5° from nadir towards starboard as indicated by the black arrow. Figure from Chanrion et al. [2019].

3.1.2 MXGS

MXGS [Østgaard et al., 2019] consists of two co-planar detector layers, HED High-Energy Detector which is mounted behind LED Low-Energy Detector. HED consits of Bismuth-Germanium-Oxide (BGO) detector bars, and detects photons in the energy range of 300 keV to >30 MeV and has a time resolution of 28.7 ns. BGO is a scintilator coupled to a photomultiplier tube (PMT). Since the light pulse from BGO is several hundreds of ns long the effective time resolution for HED is about 1 μs.
LED consists of Cadmium-Zink-Telluride (CZT) detector crystals, can detect photons in the energy range of 50 to 400 keV and has a time resolution of 1 μs. CZT is a solid state detector.

Detector	Effective Temporal resolution	Energy Range	Detector Area
HED	1 μs	300 keV to >30 MeV	900 cm^2
LED	1 μs	50 to 400 keV	1024 cm^2

Table 3.3: HED and LED spesifications

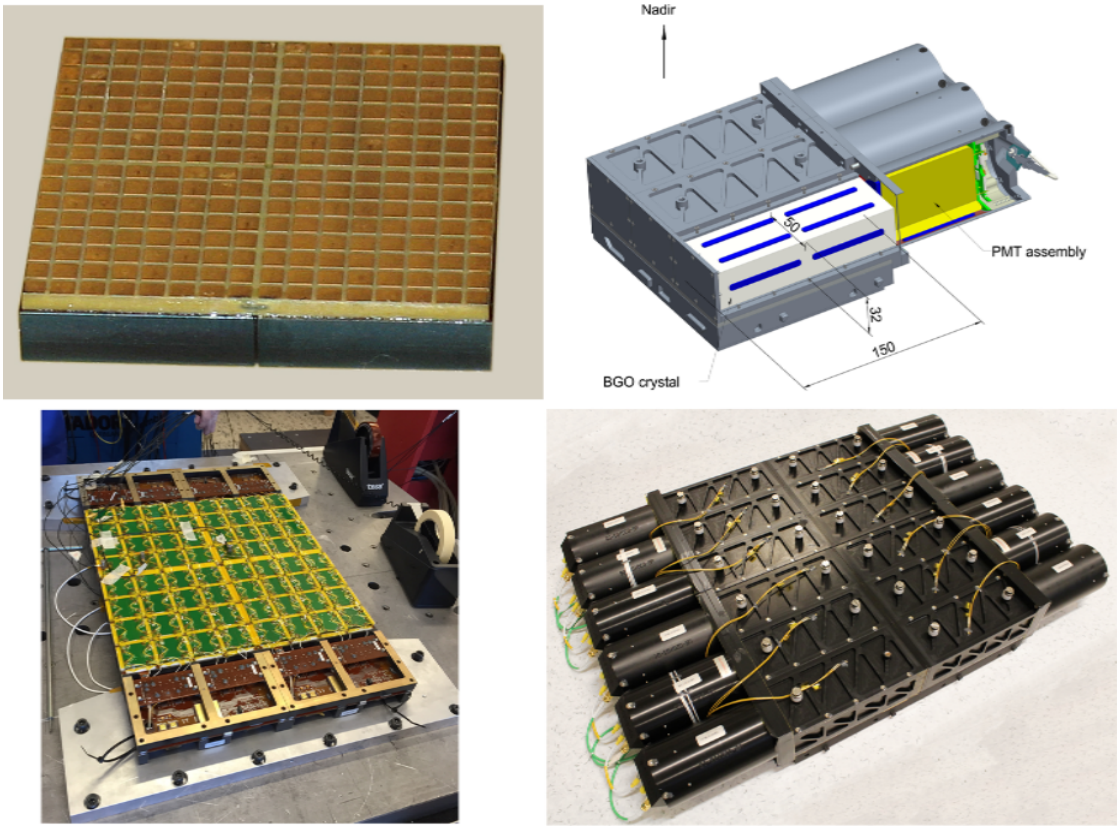

Figure 3.3: Image of LED (left) and HED (right). Upper left shows one individual detector module (DM) made of 16 x 16 CZT crystals. The full LED (bottom left) consists of 4 Detector Assembly Units, DAU each of which consists of a 4x4 array of DMs. The upper right shows one HED DAU which consists of 3 BGO bars. The full HED (lower right) consits of 4 HED DAUs. Figure from Østgaard et al. [2019].

3.2 GLD

Vaisala's Global Lightning Dataset GLD360 [Said & Murphy, 2016] is used for time and location of lightning flashes. The GLD360 dataset is created using a network of Low Frequency (LF; 30-300 kHz) and Very Low Frequency (VLF; 3-30 kHz) detectors together with Time of Arrival (TOA) and Magnetic Direction Finding (MDF) to determine the time and location of individual lightning flashes. A central processor (CP) combines measurements from multiple sensors to calculate the time and location of a lightning discharge. The dataset has a 75 - 85% detection efficiency for cloud-to-ground lightning flashes and 40 - 50% detection efficiency for intra-cloud lightning flashes. The dataset has a median location accuracy of 1.8 km with the 90th percentile at 6.4 km. The detection efficiency of the GLD dataset varies around the globe in areas with less detectors.

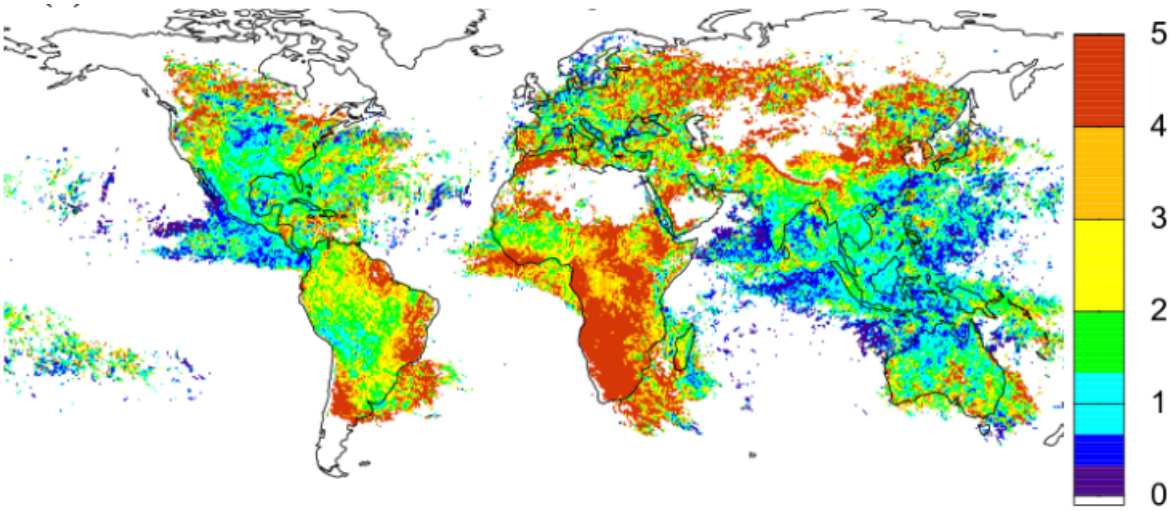

Figure 3.4: Comparison of GLD ground flash density and Optical Transient Detector (OTD) and Lightning Imaging Sensor (LIS) ground flash density. The colorbar show the ratio of LIS/OTD total flash density (fl-km^{-2}-yr^{-1}) to GLD total flash density. The regions with best detection are around America, Europe and Southeast Asia. Figure from Said & Murphy [2016].

Chapter 4

Methodology

This chapter covers the method and formulas used in this thesis. The method consists of three main steps: 1) TGF identification, 2) mapping optical data and 3) Consistency check of TGF optical and GLD data. From the first step multi pulse TGFs are found, some of which will have optical data that the second step can be applied to. The third step is to determine likely GLD sferics and optical pulses associated to the TGFs.

4.1 TGF Identification

Since TGFs are a cascade of gamma photons, the flux of a TGF is a lot higher than background. This makes it possible to detect TGFs by finding the time delay between counts from the MXGS HED and MXGS LED detectors, by plotting the time delay between each count vs counts TGFs should appear as an interval of low values on the plot. However cosmic rays also have a high flux compared to background. Cosmic rays are distinguishable from TGFs due to having a lower number of counts and additionally all counts hitting the detector almost simultaneously. Cosmic rays can then usually be identified as > 2 counts within 1 μs. TGFs on the other-hand will usually have counts in the order of 10 to the order off 10^2, while having a couple of μs between each count.

As seen in Figure 4.1 and Figure 4.2 it is possible to identify TGFs visually for most cases.
In addition it is possible to plot energy of counts in the detector by time, and histogram of counts in time (Figure 4.2, Figure 4.4) . TGFs should appear on the energy scatter plot as a dense spike of counts, while on the histogram appearing as a high peak.

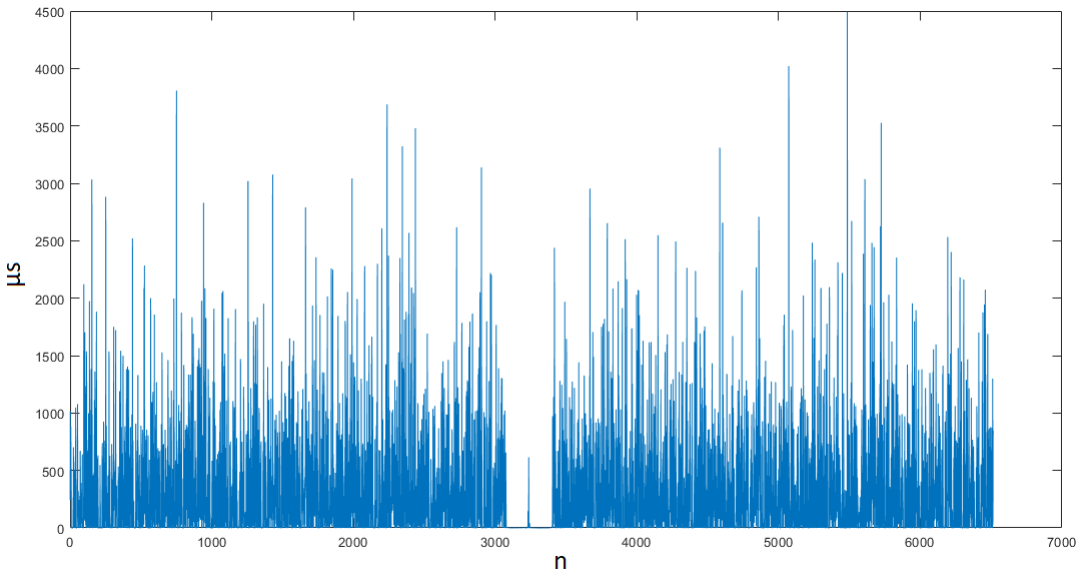

Figure 4.1: Time difference between MXGS HED counts along the y-axis and counts along x-axis, with two TGFs in the middle of the graph.

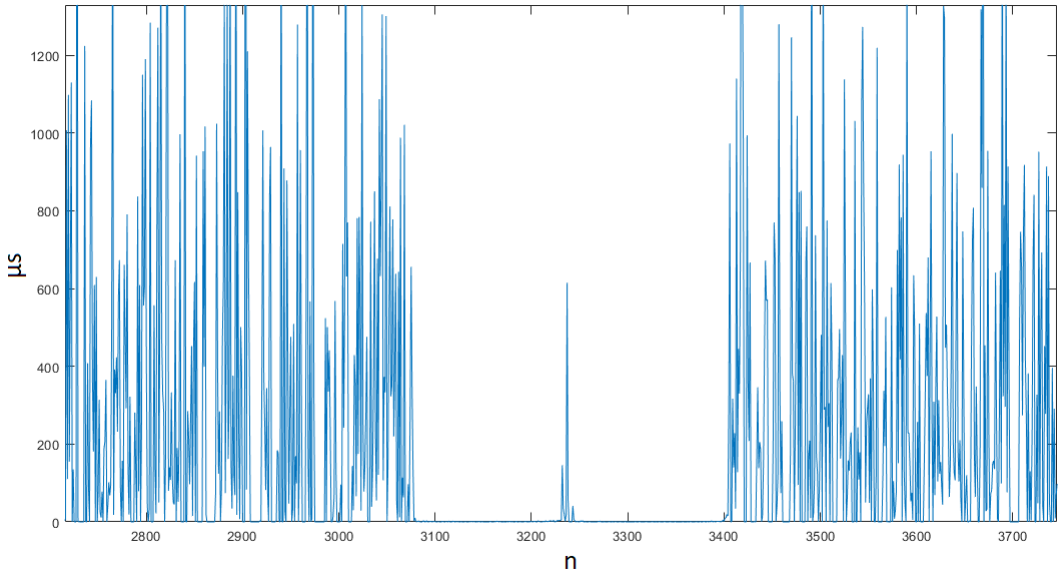

Figure 4.2: Zoomed in on the TGFs from Figure 4.1, two TGFs are distinguishable. The first starting just before count 3100 and the second starting around count 3250.

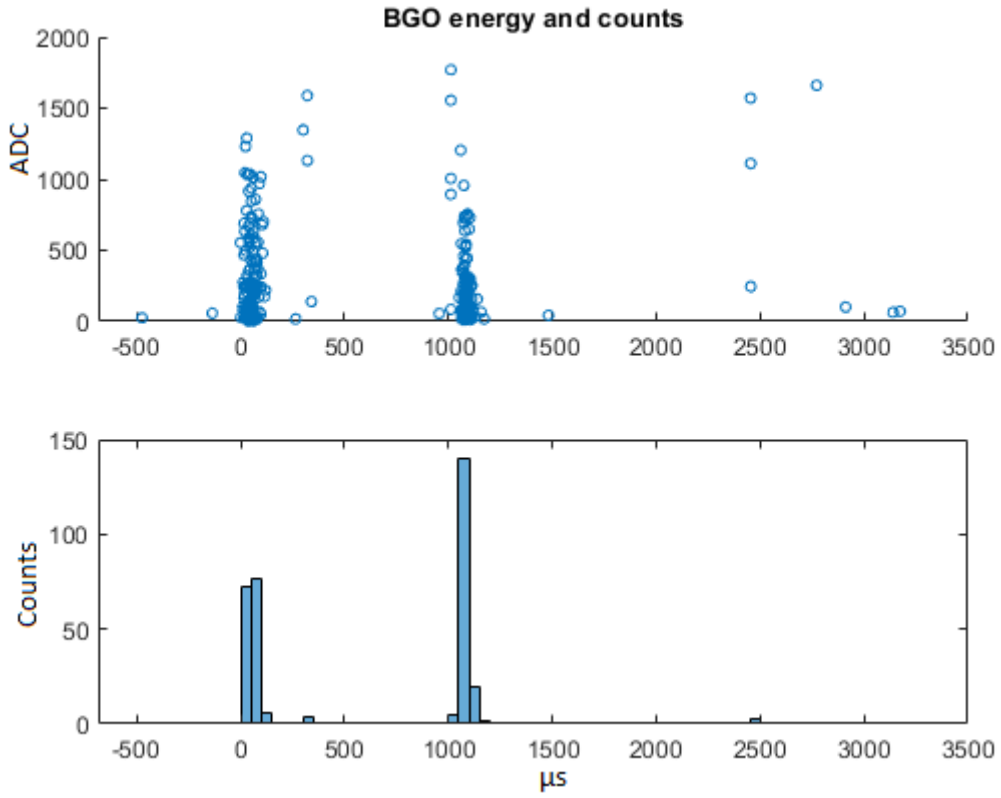

Figure 4.3: Scatter plot of energy ADC and histogram of counts from MXGS HED along y-axis, and time in μs along x-axis. Two TGFs are seen the first around $t = 0\ \mu s$ and the second around $t = 1000\ \mu s$. ADC $= 1000$ corresponds rougly to $\sim 10MeV$, but varies slightly for each BGO/PMT.

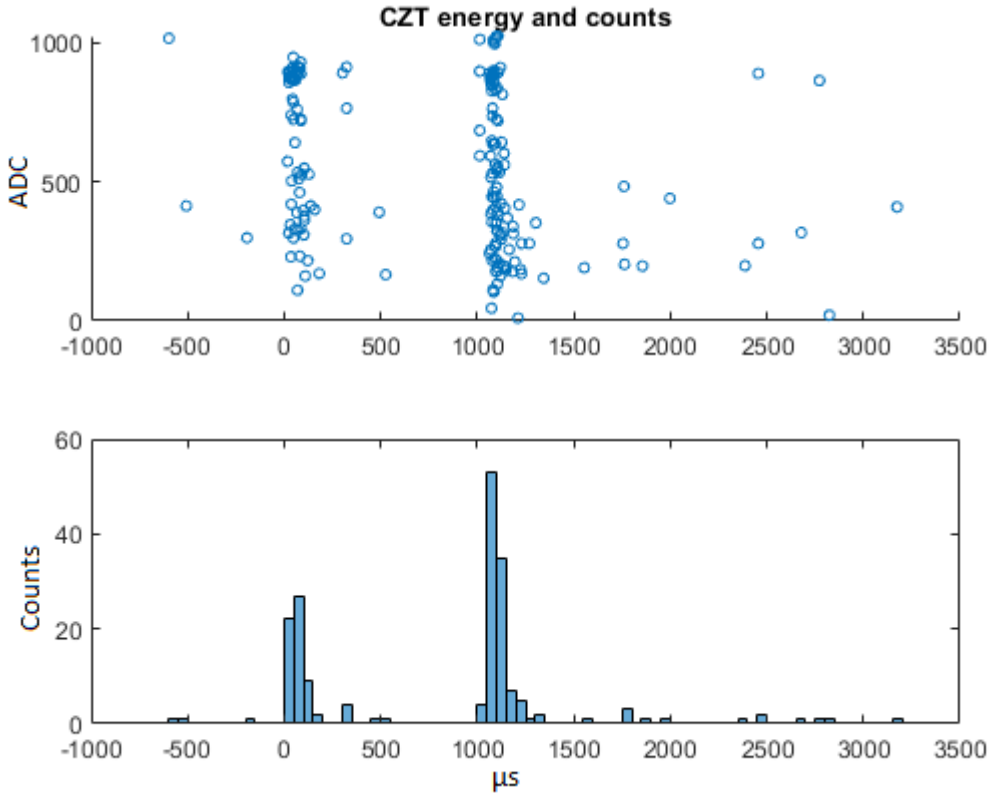

Figure 4.4: Scatter plot of energy *ADC* and histogram of counts from MXGS LED along y-axis, and time in μs along x-axis. showing the same event as Figure 4.3.

4.1.1 Identification of TGF onset and duration

For each TGF event the following information is stored:

- Number of Peaks
- Onset of TGF
- Duration of TGF
- Counts in TGF
- Time between onsets, *dt*

The number of peaks is defined as the amount of TGFs in an event.
The onset of the TGF is identified using the time delay between counts (Figure 4.2), where the onset is the first count in the low value interval for the TGF.
The end of the TGF is similarly identified using the time delay between counts (Figure 4.2) as the last count before there is a significant time delay until the next count.
The duration of the TGF is then found by taking the time difference between the onset count and the end count.
The counts in a TGF is found by taking the amount of counts from the onset count to the end count.

The dt time difference between TGFs is found by taking the time difference between the onset of one TGF until the onset of the next TGF.

4.2 Mapping CHU data onto geographic coordinates

To map the camera data onto geographical coordinates, the location of the ISS at the time of the TGF event is necessary. As telemetry data for the latitude and longitude of the ISS is not always correct, data from the ISS tracker is used instead [Paolini M. L.]. The ISS tracker provides the latitude and longitude of the ISS footpoint with a time resolution of 1 second. The ISS location ISS_{lat} and ISS_{lon} at the exact time of the TGF event is found by taking two adjacent points and linearly approximating the flight path of the ISS between them to get the sub-second position. Additionally by taking a sample of positions from the ISS tracker over several seconds and doing a linear approximation of the flight path, the tangential velocity v_{lat} and v_{lon} at the time of the TGF event is found. The Altitude h and rotation ψ_x, ψ_y, ψ_z of the ISS are given by the MMIA telemetry.

4.2.1 LVLH frame and NED frame

Two frames of reference will be used: 1) the ISS's Local Vertical Local Horizontal (LVLH) frame of reference and 2) the North East Down (NED) frame of reference.

LVLH is a right handed, local tangent plane coordinate system.
LVLH axes are defined as:

- Z-axis points towards Nadir, the center of the Earth.
- X-axis points tangential to the Earths surface along the direction of travel of the ISS.
- Y-axis points orthogonal to the X and Z-axis such that it forms a right hand system.

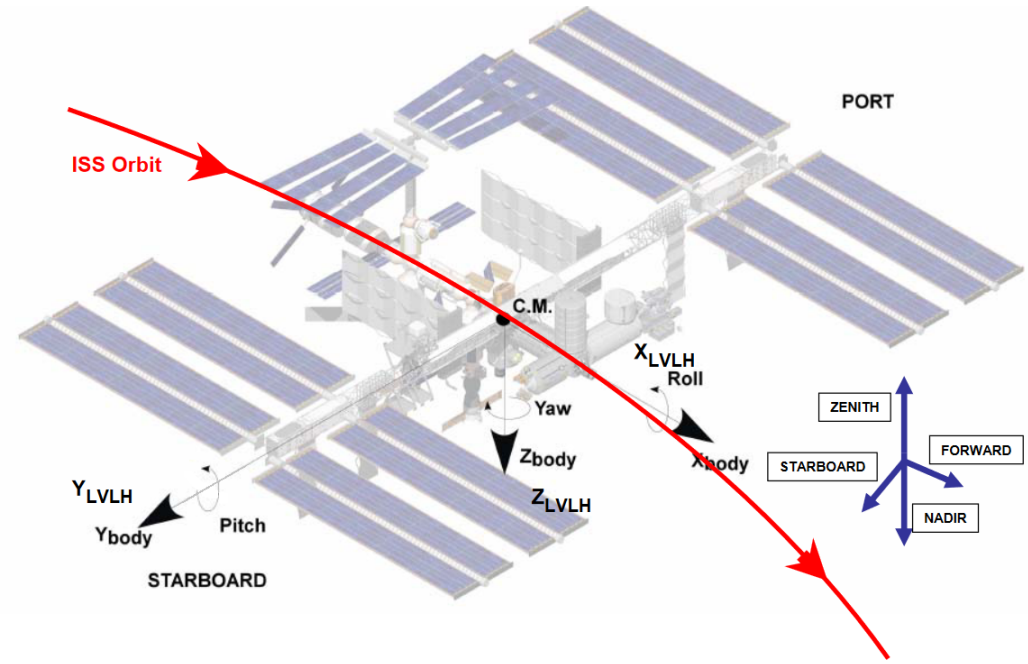

Figure 4.5: Illustration of the ISS's Local Vertical Local Horizontal reference frame. The yaw, pitch and roll indicated show the positive rotation direction. Figure from [Hatton J.]

NED is a left handed, local tangent plane coordinate system.
NED axes are defined as:

- Z-axis points towards Nadir, the center of the Earth.
- X-axis points tangential to the Earths surface towards the local east direction.
- Y-axis Points tangential to the Earths surface towards the local north direction.

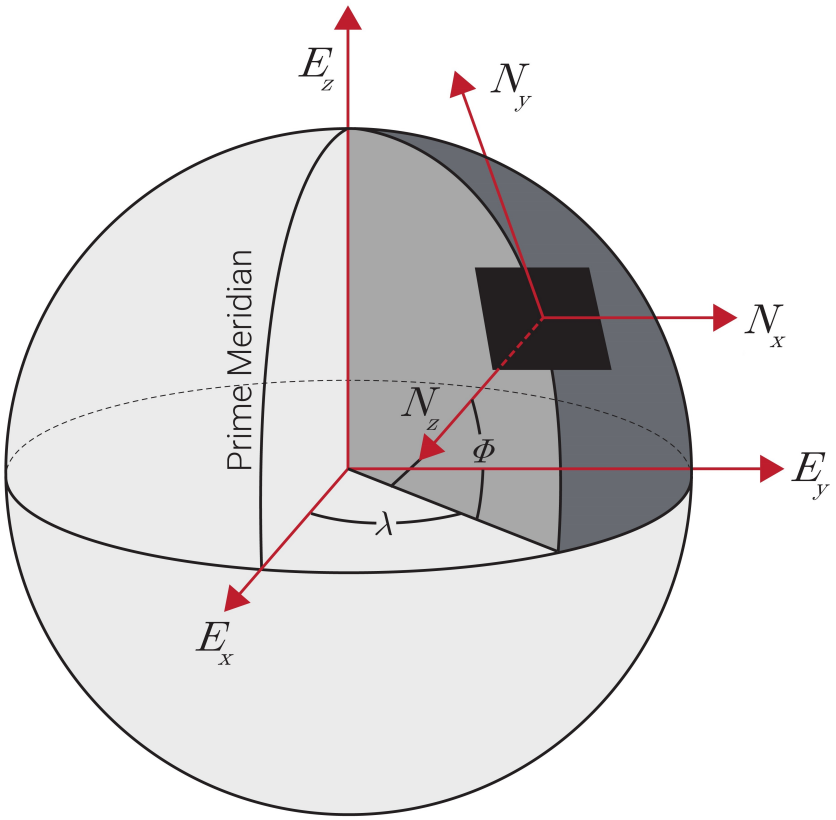

Figure 4.6: Illustration of the North East Down reference frame. Figure from [Vectornav]

4.2.2 Rotation in LVLH frame

The ISS is not perfectly stationary in the LVLH system and usually has some small roll ψ_x, pitch ψ_y, yaw ψ_z rotation that changes with time. Additionally MMIA is not facing directly down along the Z-axis but is mounted onto the ISS with a roll of 5° counterclockwise (rotation around X-axis from Z towards Y) which has to accounted for before applying rotations. To find the cameras orientation in the LVLH reference system we have to account for these rotations.

The rotation matrix of the roll ψ_x, around the X-axis:

$$R_x = \begin{pmatrix} 1 & 0 & 0 \\ 0 & cos(\psi_x) & -sin(\psi_x) \\ 0 & sin(\psi_x) & cos(\psi_x) \end{pmatrix} \tag{4.1}$$

The rotation matrix of the pitch ψ_y, around the Y-axis:

$$R_y = \begin{pmatrix} cos(\psi_y) & 0 & sin(\psi_y) \\ 0 & 1 & 0 \\ -sin(\psi_y) & 0 & cos(\psi_y) \end{pmatrix} \tag{4.2}$$

The rotation matrix of the yaw ψ_z, around the Z-axis:

$$R_z = \begin{pmatrix} cos(\psi_z) & -sin(\psi_z) & 0 \\ sin(\psi_z) & cos(\psi_z) & 0 \\ 0 & 0 & 1 \end{pmatrix} \tag{4.3}$$

Rotation matrix of the MMIA mounting position:

$$R_I = \begin{pmatrix} 1 & 0 & 0 \\ 0 & cos(-5°) & -sin(-5°) \\ 0 & sin(-5°) & cos(-5°) \end{pmatrix} \tag{4.4}$$

For clarity the roll ψ_x, pitch ψ_y, yaw ψ_z are defined as positive when they are clockwise relative to the LVLH reference frame, when the axis the rotation occurs about points away from observer (see Figure 4.5).

The order of applying these rotations onto a vector is important as the rotation matrices are not commutative. The order of application is not 100% sure, but given the small angles of rotation the difference in order of application will be quite small. The convention used here is the Tait-Bryan convention which applies the rotations in the order of yaw, pitch, roll or z-y-x.
This gives that any vector relative to the camera is given in the LVLH system as:

$$\bar{u}^{LHLV} = R_x R_y R_z R_I \bar{u} \tag{4.5}$$

Pre-multiplication is used here meaning that the multiplication order is given by always multiplying the vector with the matrix to it's left, until all matrices are multiplied.

4.2.3 Rotation matrix from LVLH to NED

Since both LVLH and NED are local tangent plane coordinate systems, they both share a common axis being the z-axis. NED however is a left hand coordinate system, while LVLH is a right hand coordinate system. This means that a conversion from LVLH to NED can be expressed as a rotation along the z-axis by the angle θ_E which is the angle between LVLH x-axis and NED x-axis, followed by inverting the y-axis:

$$M_{LVLH \to NED} = \begin{pmatrix} 1 & 0 & 0 \\ 0 & -1 & 0 \\ 0 & 0 & 1 \end{pmatrix} \begin{pmatrix} cos(\theta_E) & -sin(\theta_E) & 0 \\ sin(\theta_E) & cos(\theta_E) & 0 \\ 0 & 0 & 1 \end{pmatrix} \tag{4.6}$$

Which gives us any vector in the LVLH system can be expressed in the NED system as:

$$\bar{u}^{NED} = M_{LVLH \to NED} \bar{u}^{LVLH} \tag{4.7}$$

The angle θ_E can be calculated from the ISS tangential velocity v_{lat}, v_{lon} found from the ISS tracker and is given as:

$$\theta_E = atan\left(\frac{-v_{lat}}{v_{lon}}\right) \tag{4.8}$$

4.2.4 NED to geographic coordinate

Approximating the Earth as a plane it is possible to calculate the projected location of a NED vector as a intersection point between a plane, and a line. For a vector $\bar{u} = \begin{pmatrix} a \\ b \\ c \end{pmatrix}$ starting in origin the line equation is given by:

$$l(t) = \left\{ \begin{array}{c} x = at \\ y = bt \\ z = ct \end{array} \right\} \tag{4.9}$$

where t is an arbitrary variable.
The Earth is set as a plane parallel to the xy-plane at a height h given by the altitude of the ISS.
The line will then cross this plane when $z = h$, this gives:

$$t_1 = \frac{h}{c} \tag{4.10}$$

Inserting t_1 into x and y gives:

$$x(t_1) = \frac{a}{c} \cdot h \tag{4.11}$$

$$y(t_1) = \frac{b}{c} \cdot h \tag{4.12}$$

In a NED system the y-component and x-component points towards local north and local east respectively (see Figure 4.6). Therefore, the calculated x and y values (in km) will correspond to the longitudinal and latitudinal distance from the footpoint of the ISS to the projected location on Earth for the vector $\bar{u}$.
The actual longitude and latitude coordinates for the projected location can then be found by converting the x and y values into degrees on Earth by multiplying x and y with $\frac{360}{2\pi \cdot 6371}$. Then adding this value onto the coordinates of the ISS footpoint gives:

$$Lat = ISS_{lat} + \frac{b}{c} \cdot \frac{h \cdot 360}{2\pi 6371} \tag{4.13}$$

$$Lon = ISS_{lon} + \frac{a}{c} \cdot \frac{h \cdot 360}{2\pi 6371} \tag{4.14}$$

4.2.5 Field-of-View (FoV) projection

As specified in table 3.1 both CHU 337 and CHU 777 have a square FoV with 80° over the diagonal.
The photometers as specified in table 3.2 also have a square FoV with 80° over the diagonal with the exception of the 180-230 nm photometer which has a circular FoV with 80° over the diagonal.

To find the projected location for any vector on the Earth, the rotations of the FoV from the MMIA mounting position and from ISS's rotation, are applied onto the vector by using Eq. 4.5. Then the vector is converted into the NED system by applying Eq. 4.7. Using the values of the vector in the NED system the projected latitudinal coordinate can be found by using Eq. 4.13, and the projected longitudinal coordinate by Eq. 4.14. This process requires that all vectors are first defined in the LVLH system relative to if the camera was facing directly towards the Earth along the z-axis.

The center of the FoV for the CHU is defined as directly along the Z-axis of the camera (0, 0, 1).
The circular FoV of the 180-230 nm photometer can be defined in spherical coordinates as a cone with polar angle $\theta = 40°$. On the map the circular FoV will appear as slightly elliptic.
The square FoV used by the CHU 337, CHU 777 and the 337 and 777 photometer can also be defined in spherical coordinates, as a pyramid where the four vectors to each corner have polar angle $\theta = 40°$, and azimuthal angle $\varphi = 45°, 135°, 225°, 315°$.
The spherical coordinates are then given in Cartesian coordinates as:

$$\bar{u} = \begin{Bmatrix} sin\theta cos\varphi \\ sin\theta sin\varphi \\ cos\theta \end{Bmatrix} \tag{4.15}$$

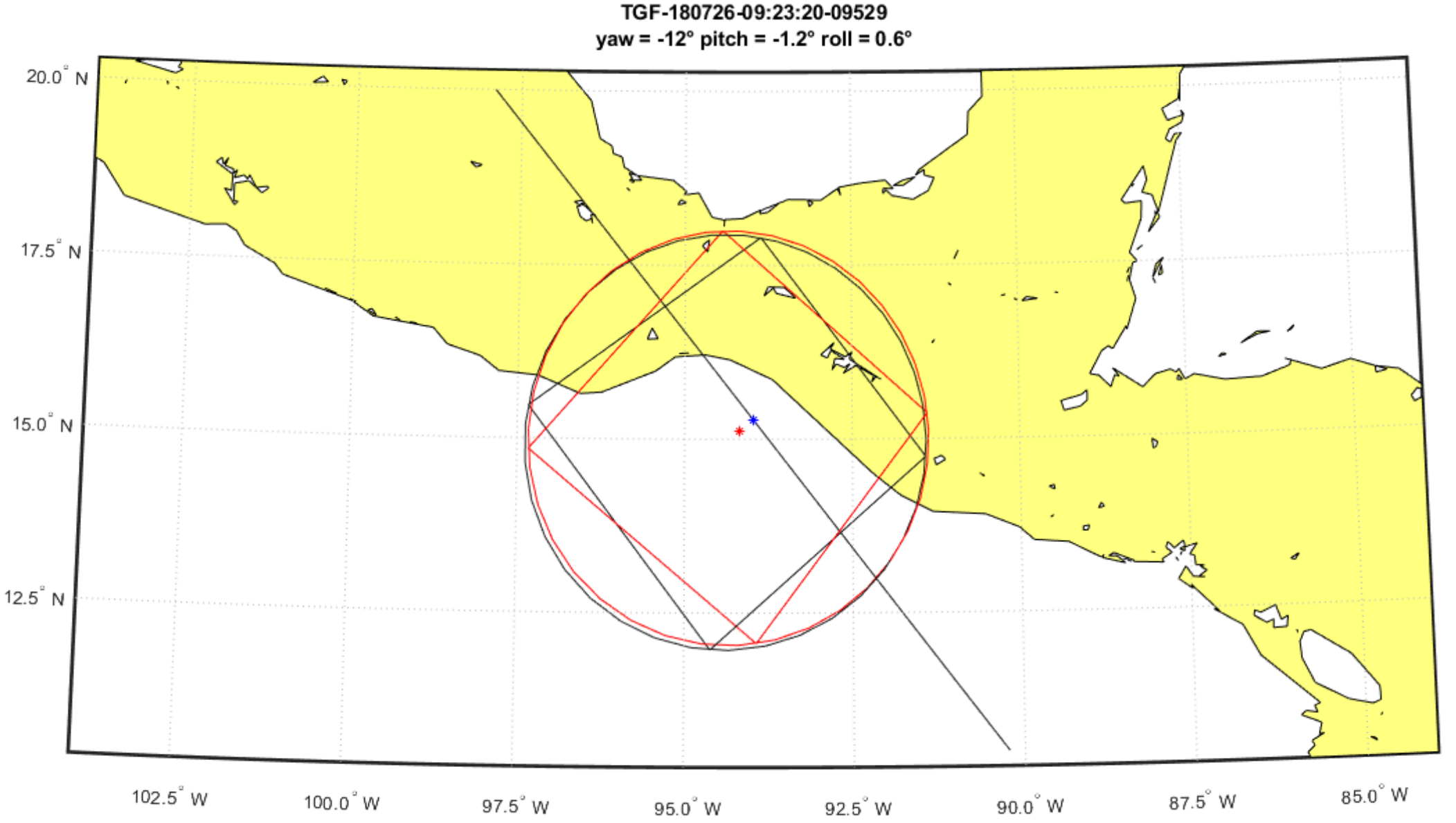
TGF-180726-09:23:20-09529
yaw = -12° pitch = -1.2° roll = 0.6°
20.0° N
17.5° N
15.0° N
12.5° N
102.5° W
100.0° W
97.5° W
95.0° W
92.5° W
90.0° W
87.5° W
85.0° W

Figure 4.7: FoV projected onto map. The black square shows FoV without taking account of rotations, while red shows FoV with rotations. The blue mark is the footpoint of the ISS, while the red mark is the center of the FoV. The outer circle of the FoV shows the slightly elliptical FoV of the 180-230 nm photometer, while the inner square of the FoV shows the square FoV used by both CHU and the other photometers.

4.2.6 CHU image projection

As specified in table 3.1 both CHU 337 and CHU 777 have an image resolution of 1024x1024 pixels, which is stored in a 1026x1056 data matrix.
The 1026x1056 matrix needs to be placed between the four corner vectors of the square FoV. This requires knowing the angular output each pixel corresponds to, which requires the lens specifics of both CHU 337 and CHU 777. It is however possible to do some approximations for the lenses.
Since each pixel corresponds to some polar angle and azimuth angle range, every pixel can be described by four vectors for each corner of the pixel. Since the corners of neighboring pixels overlap, 1027x1057 vectors are necessary to describe the 1026x1056 matrix.
Three different lens approximations where used:

1. Image as a flat plane
2. Image as surface on a sphere
3. Image as surface on a sphere using great circles

Each method uses that the image should fit between the square given by the FoV corner vectors, so the Cartesian coordinates go from $x = \{-\frac{1}{\sqrt{2}}sin(40°), \frac{1}{\sqrt{2}}sin(40°)\}$, $y = \{-\frac{1}{\sqrt{2}}sin(40°), \frac{1}{\sqrt{2}}sin(40°)\}$. While the z value determines the lens effect of the image.
The first method places the image between the corner vectors as a flat plane by setting $z = cos(40°)$ for all vectors. Any position (m, n) in the 1027x1057 matrix then gives the vector output:

$$\bar{u}(m,n) = \left\{ \begin{array}{c} x = \left(-\frac{1}{2} + \frac{m-1}{1056}\right)\sqrt{2}sin(40°) \\ y = \left(-\frac{1}{2} + \frac{n-1}{1026}\right)\sqrt{2}sin(40°) \\ z = cos(40°) \end{array} \right\}$$

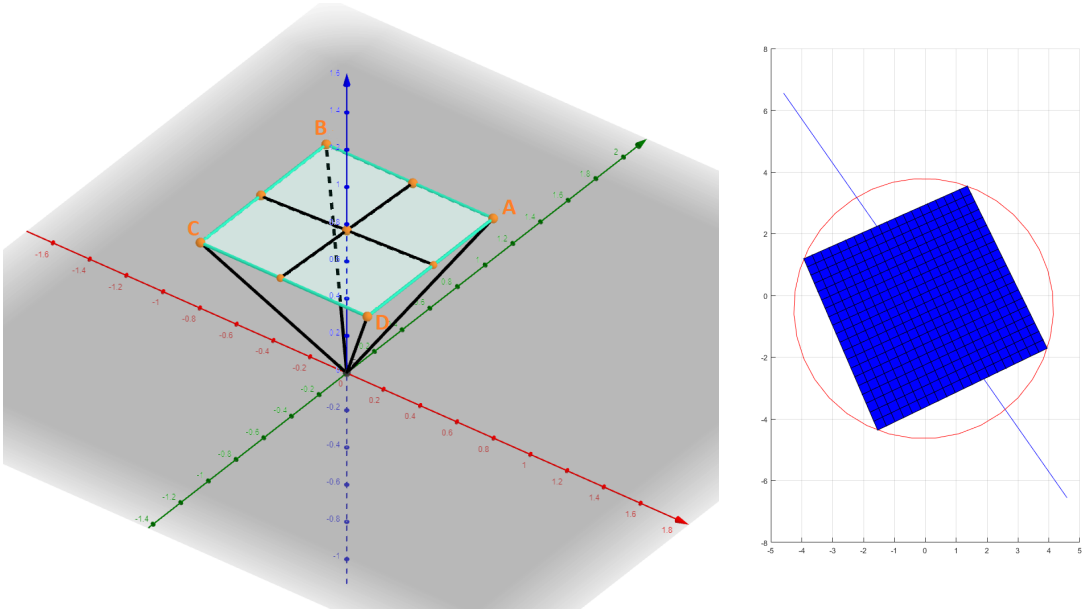

Figure 4.8: Left image shows example of the first lens approximation if the image had 4 pixels. The points A,B,C,D show the corner vectors of the FoV. The vectors used to project the image is then the vectors from the origin to all of the orange points. Right image shows example of a 20x20 image projected using this lens approximation.

The second method places the image between the corner vectors as the surface on a sphere, by using the Cartesian equation of a sphere with radius 1:

$$\bar{u}(m,n) = \left\{ \begin{array}{c} x = \left(-\frac{1}{2} + \frac{m-1}{1056}\right)\sqrt{2}sin(40°) \\ y = \left(-\frac{1}{2} + \frac{n-1}{1026}\right)\sqrt{2}sin(40°) \\ z = \sqrt{1-x^2-y^2} \end{array} \right\}$$

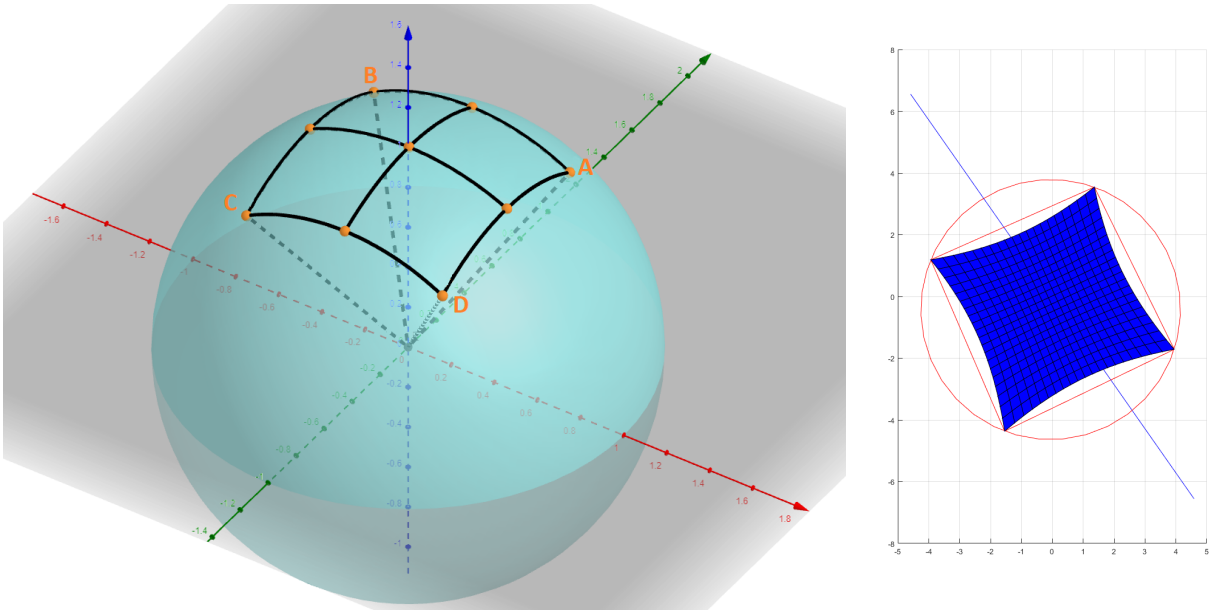

Figure 4.9: Example of the second lens approximation if the image had 4 pixels, The image is warped onto a sphere between the same x and y values used in the first method. The points A,B,C,D show the corner vectors of the FoV. The vectors used to project the image is then the vectors from the origin to all of the orange points. Right image shows example of a 20x20 image projected using this lens approximation, for this method the pixels are smaller towards the center of the image and become larger and more deformed towards the edges of the image.

The third method also projects the image onto a sphere but divides the image into pixels along the sphere rather than along the xy plane.
This means that each pixel corner is the cross point between a great circle lying in the x axis with some angle θ from the z axis and a great circle in the y axis with some angle θ from the z axis.

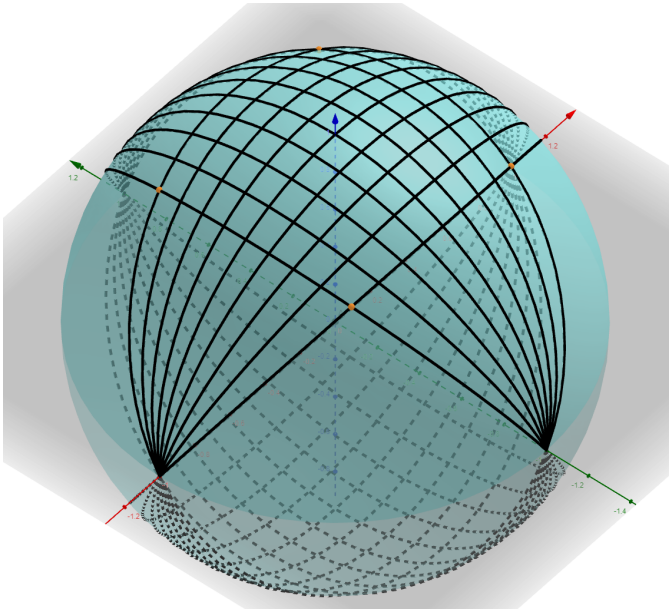

Figure 4.10: Example of placing an image onto a sphere using great circles, here 8x8 pixels are created using two sets of 8 great circles.

By treating the great circles as planes and finding their intersection lines it is possible to get the vector that corresponds to the cross point of the circles. A plane can be defined by two vectors lying within that plane. The set passing through the x-axis will always have the vector $[1, 0, 0]$ while the set passing through the y-axis will always have the vector $[0, 1, 0]$. Both sets will contain a vector:

$$\begin{bmatrix} \frac{1}{\sqrt{2}} sin\theta \\ \frac{1}{\sqrt{2}} sin\theta \\ cos\theta \end{bmatrix}$$

Where θ is the angle between the vector and the z-axis, and goes from $-40°$ to $40°$ where it is a corner vector of the FoV. For the set of planes passing through the x-axis we set this angle as some angle α which goes from $-40°$ to $40°$ in 1056 equal length steps. For the set of planes through the y-axis we set this as some angle β which goes from $-40°$ to $40°$ in 1026 equal length steps. The plane normal vectors are then given by:

$$\bar{n}_x = \begin{bmatrix} 0 \\ -cos(\alpha) \\ \frac{1}{\sqrt{2}} sin(\alpha) \end{bmatrix}, \bar{n}_y = \begin{bmatrix} -cos(\beta) \\ 0 \\ \frac{1}{\sqrt{2}} sin(\beta) \end{bmatrix}$$

Taking the cross product of the plane normal vectors gives the vector for the line of intersection for the planes, which corresponds to the vectors of the corners of the image pixels.

$$\bar{u}(m,n) = \begin{Bmatrix} x = \frac{1}{\sqrt{2}} cos(\alpha) sin(\beta) \\ y = \frac{1}{\sqrt{2}} sin(\alpha) cos(\beta) \\ z = cos(\alpha) cos(\beta) \end{Bmatrix}$$

$$\begin{Bmatrix} \alpha(m) = \left(-\frac{1}{2} + \frac{m-1}{1056}\right) \cdot \frac{80\pi}{180} \\ \beta(n) = \left(-\frac{1}{2} + \frac{n-1}{1026}\right) \cdot \frac{80\pi}{180} \end{Bmatrix}$$

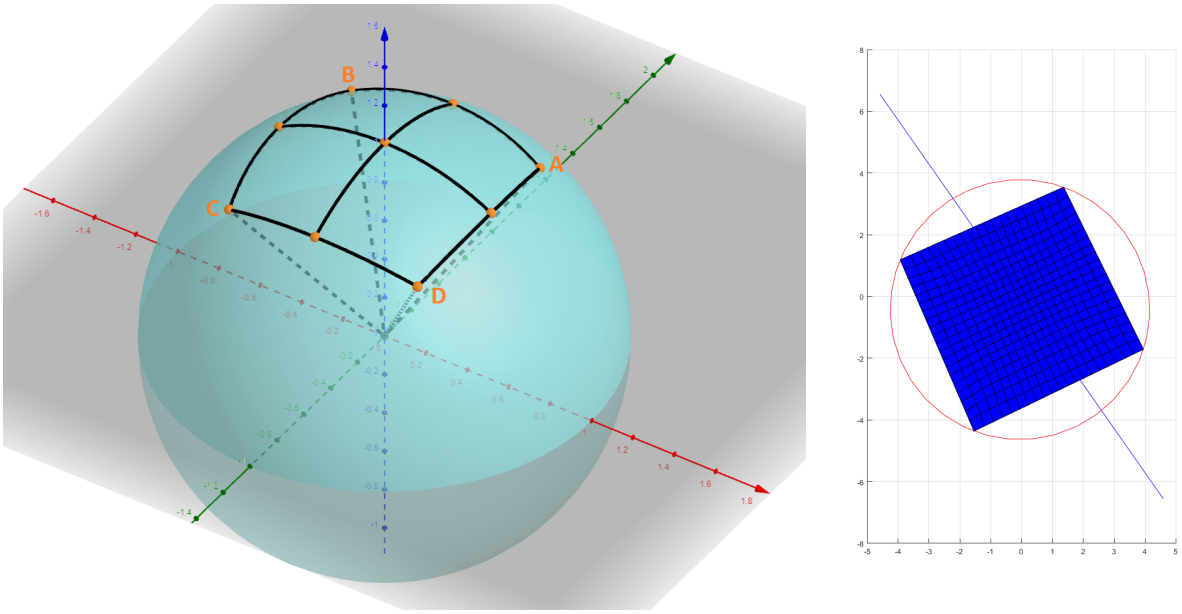

Figure 4.11: Example of third lens approximation if the image had 4 pixels, The image is warped onto a sphere where each corner of a pixel is given as the cross point between a circle along the x axis rotated around the x axis some angle θ_1 and a circle along the y axis rotated around the y axis some angle θ_2. The points A,B,C,D show the corner vectors of the FoV. The vectors used to project the image is then the vectors from the origin to all of the orange points. Right image shows example of a 20x20 image projected using this lens approximation, for this method the pixels are smaller towards the center of the image but become larger towards the edges, unlike the second method the image still fills the entire FoV.

4.3 Testing the projection with coastline images and GLD

The different lens approximations where tested using data from an event in which the CHU 337 and CHU 777 was used to take an image of a coastline. It was found for this event that the camera image did not match with the position of the ISS at the time of recording. The correct position of the ISS for the image appeared to be the position it was in about 12 seconds earlier than the time recorded in the data. This error in the stored timing of the event is most likely caused due to ASIM not operating by standard procedure during this specific event.
By comparing the coastline image projection by the three different lens approximations with a map of the coastline, it was found that the second lens approximation matched the camera data closest to the map. The image was additionally scaled up to match coastline with the map better, which was done by adding an additional 50 km to the altitude of the ISS in the code.

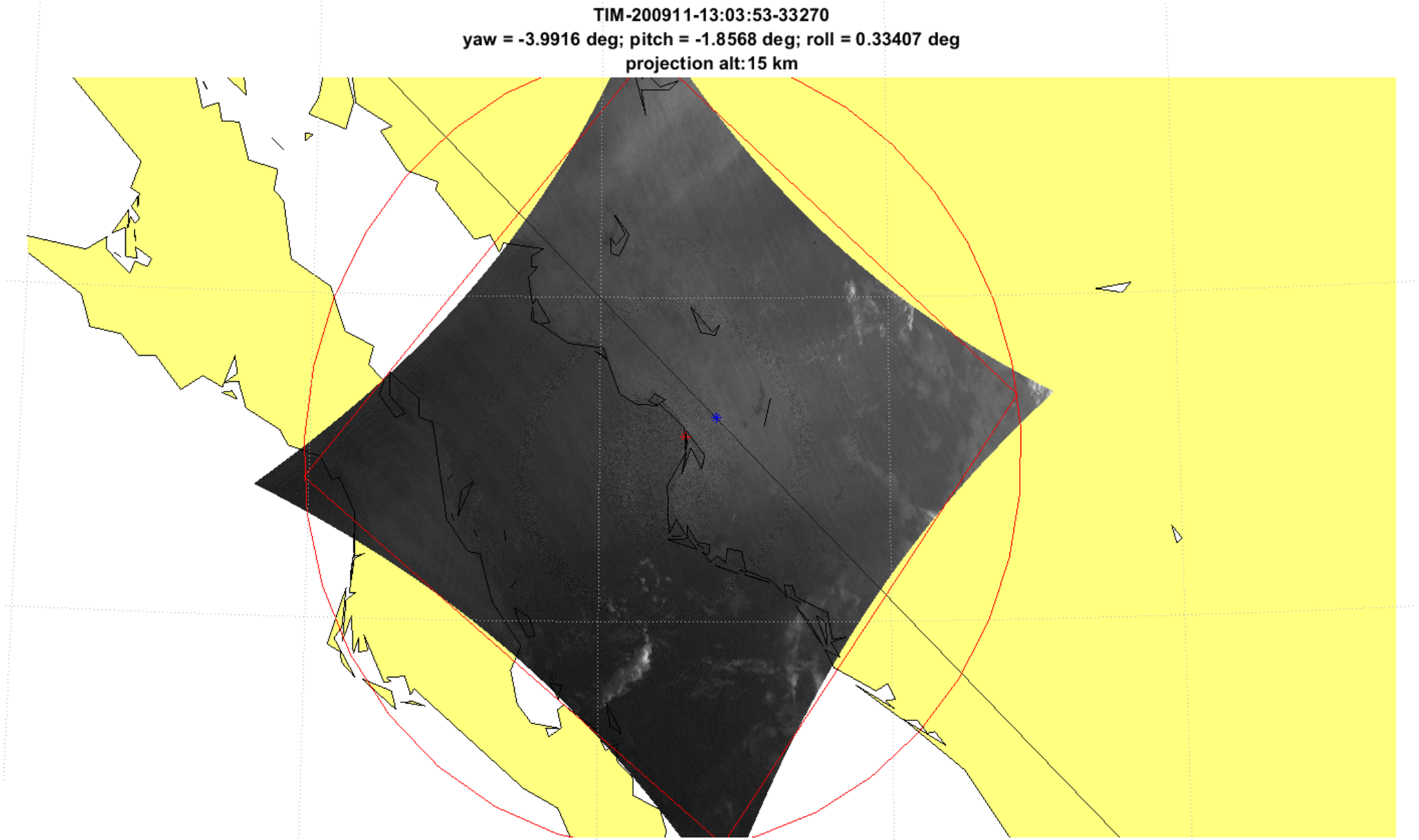
TIM-200911-13:03:53-33270
yaw = -3.9916 deg; pitch = -1.8568 deg; roll = 0.33407 deg
projection alt:15 km

Figure 4.12: Comparison of camera image projection with map data, using the second lens approximation described in 4.2.6. The black lines in the figure show the coastline data overlaid onto the projected image. The image matches closest towards the center of the FoV, while deviating more towards the edges.

By taking the distance between geographical features on the image and the corresponding geographical location from the map. It was found that the projection method has an average offset of about 28 km outside of the center of the FoV.

The lens approximation was additionally compared with GLD data, by taking MMIA triggers that contained several bright spots in the CHU data and comparing the projected location with GLD data within same time frame.

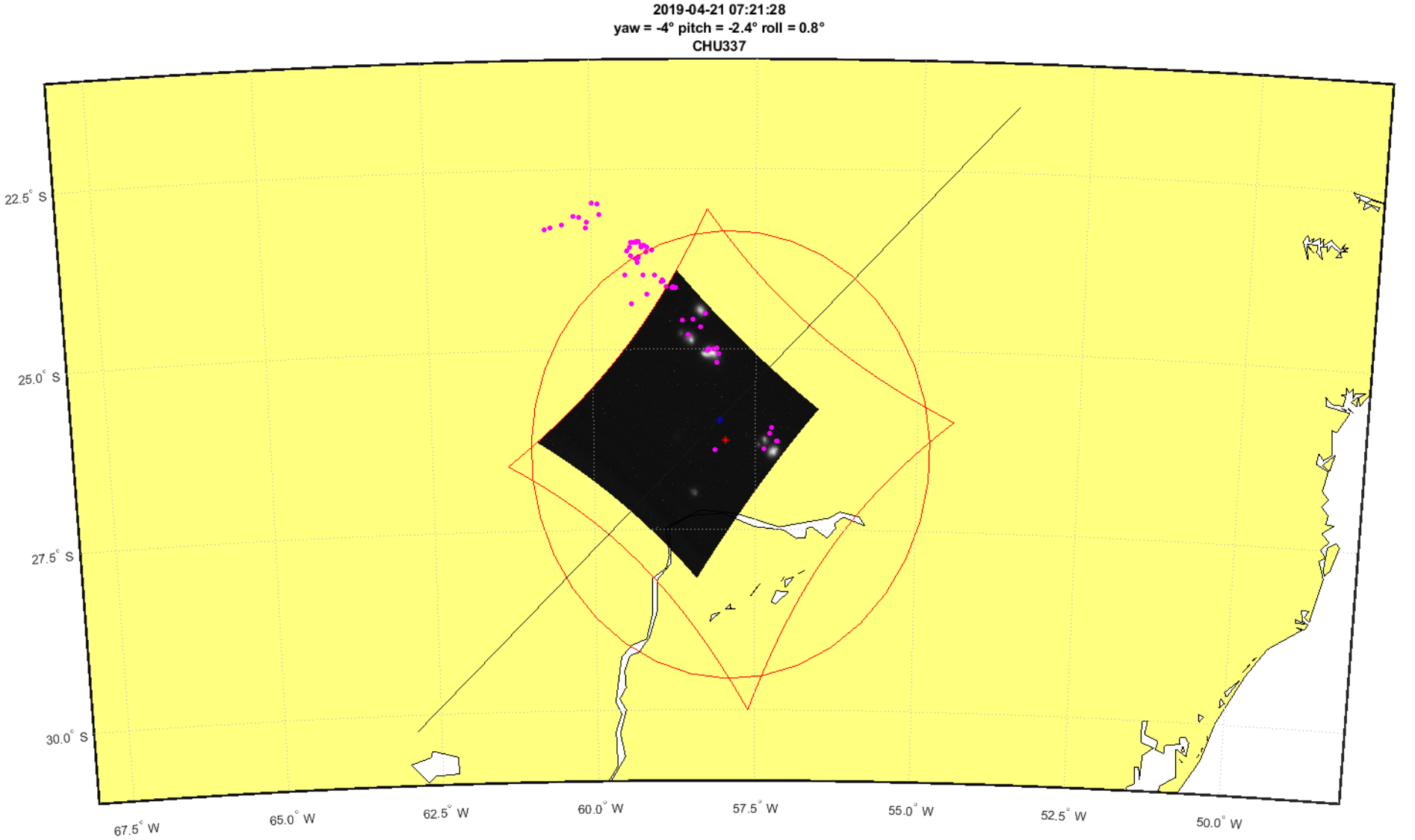
2019-04-21 07:21:28
yaw = -4° pitch = -2.4° roll = 0.8°
CHU337
22.5° S
25.0° S
27.5° S
30.0° S
67.5° W
65.0° W
62.5° W
60.0° W
57.5° W
55.0° W
52.5° W
50.0° W

Figure 4.13: Mapping of a MMIA trigger with several bright spots, the image shows all camera frames of the event interpolated into one image, with GLD triggers that occurred within 1s of the images displayed on top.

Taking the distance between optical flashes and GLD for 46 such events it was found that the projected image location was on average 19.8 km away from a corresponding GLD sferic.

4.4 Consistency check with TGF characteristics and location from optics and GLD

Similarly to section 3.2 in [Bjørge-Engeland et al. 2022] the MXGS HED data of the TGFs are used to do a consistency check for GLD sferics and optical pulses that may be associated with the TGFs.

For multi pulse TGFs with optical data, optical pulses are considered to be associated if they occur within a few ms of a TGF peak. The multi pulse TGFs with optical data are then categorized into three different samples:

Optical 1: Events with optical pulses associated with each TGF peak.
Optical 2: Events with optical pulses associated with one TGF peak.
Optical 3: Events with no associated optical pulse.

Additionally all multi pulse TGFs where checked for possible GLD sferics associated with the events. As done by Bjørge-Engeland et al. [2022] GLD sferics within $[-10, 40]$ ms of TGF detection times, and within 800 km from the ISS footpoint where considered. Unlike Bjørge-Engeland et al. [2022] time alignment of GLD sferics and MMIA optical pulses was not preformed. The multi pulse TGFs where categorized into four different samples:

GLD 1: Events with only one GLD detection in the $[-10, 40]$ ms timewindow.
GLD 2: Events with multiple GLD detections that could be associated with the TGFs.
GLD 3: Events with a GLD detection that is uncertain if associated.
GLD 4: Events with no possible GLD sferics associated with the TGFs.

For TGFs with possible optical pulse associations or GLD sferic associations a consistency check was preformed based on the radial distance of the optical pulse/GLD sferic location from the ISS footpoint, to determine cases where optical pulse/GLD sferic where unlikely to be associated so they could be discarded from the optical/GLD grouping. It is assumed a TGF production half-cone of 40°, with no tilt. The following TGF characteristics were considered:

1. "**TGF intensity**: Due to scattering processes in the atmosphere and the $1/r^2$-effect, we expect the number of counts detected by ASIM to be less for TGFs produced at large radial distances from the ISS footpoint [Gjesteland et al., 2011]."[Bjørge-Engeland et al. 2022]

2. "**TGF hardness**: if high energy counts ($> 10MeV$)" which is approximately > 1000 ADC but varies slightly for each BGO/PMT, "are detected by HED we expect the source location of the TGF to be at a short radial distance from the footpoint [Carlson et al., 2007; Hazelton et al., 2009;Østgaard et al., 2008]. This is because only photons that have been Compton scattered and have reduced energies will be observed outside the initial angular distribution of photons, which was found to be $30 - 40°$ [Gjesteland et al., 2011]. As shown in Figure 2 in Lindanger et al. [2021], the energy spectra of TGFs become softer when observed from a source location at a larger radial distance and Gjesteland et al. [2011] showed that the softening of the TGF spectra is significant at observation angles $> 40°$. Hence, we expect HED to detect photons with energies $> 10MeV$ if the TGF is produced at a location within the MMIA FOV. As the initial angular distribution of high-energy gamma rays could be slightly tilted toward the ISS, detections of counts with energies $> 10MeV$ were only used as an indicator for the TGF being produced inside the MMIA FOV." [Bjørge-Engeland et al. 2022]

Additionally for possible GLD sferic associations:

3. "**TGF duration**: [Connaughton et al. [2013] and Lindanger et al., [2020] both showed that long duration TGFs are less likely to have associated sferic detections than short TGFs, and hence we expect it to be less likely that very long TGFs have associated sferic detections. This led to more caution when considering possible sferic matches for longer TGFs than for the shorter TGFs detected." [Bjørge-Engeland et al. 2022]

For cases with both optical associations and GLD sferic associations we expect that if both are associated with the TGF, then they should have approximately the same location.

Chapter 5

Results

In this chapter we will present the multi pulse TGFs identified from ASIMs data from launch until the end of 2022, using the procedure described in 4.1 and will cover the geographical distribution of multi TGFs, the distribution of the time between pulses dt, the multi pulse TGFs with possible associated optical pulses and GLD sferics. Additionaly multi pulse TGFs where categorized based on the pattern of the X-rays.

5.1 Distribution of Multi TGFs from ASIM data

The distribution of multi pulse TGFs from ASIMs data was plotted using the longitude and latitude data (Figure 5.1). In general there are three regions with concentrations of TGFs being: the Caribbean, Africa and south east Asia.

In total 52 multi pulse TGFs where found, with 10 in the Caribbean, 11 in Africa and 28 in south east Asia.
Compared to the distribution of regular TGFs detected by ASIM (Figure 5.2), a total of 1428 TGFs have been detected since launch until the end of 2022, with 409 regular TGFs in the Caribbean, 266 in Africa and 583 in sounth east Asia.

To see if there is any difference in the time between onsets pulses dt between regions, histograms of the dt value for each region was made (Figure 5.3).

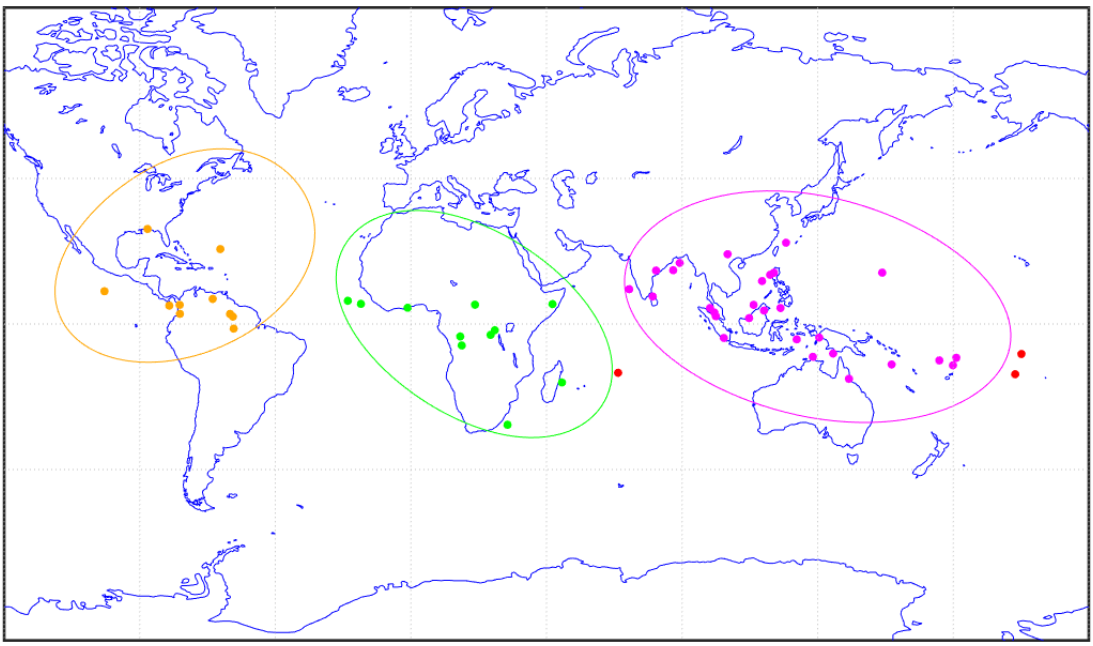

Figure 5.1: Map of all multi TGFs recorded by ASIM as of launch until the end of 2022, separated into regions and color coded. Orange corresponds to Caribbean, green for Africa and purple for south east Asia.

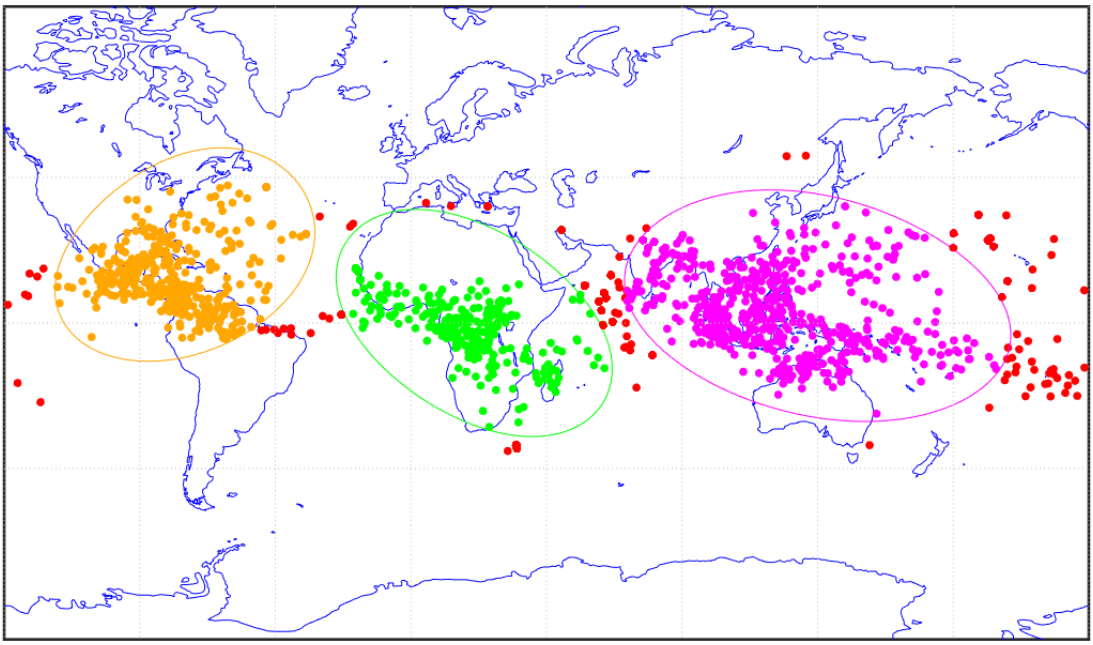

Figure 5.2: Map of all regular TGFs recorded by ASIM as of launch until the end of 2022, separated into regions and color coded. Orange corresponds to Caribbean, green for Africa and purple for south east Asia.

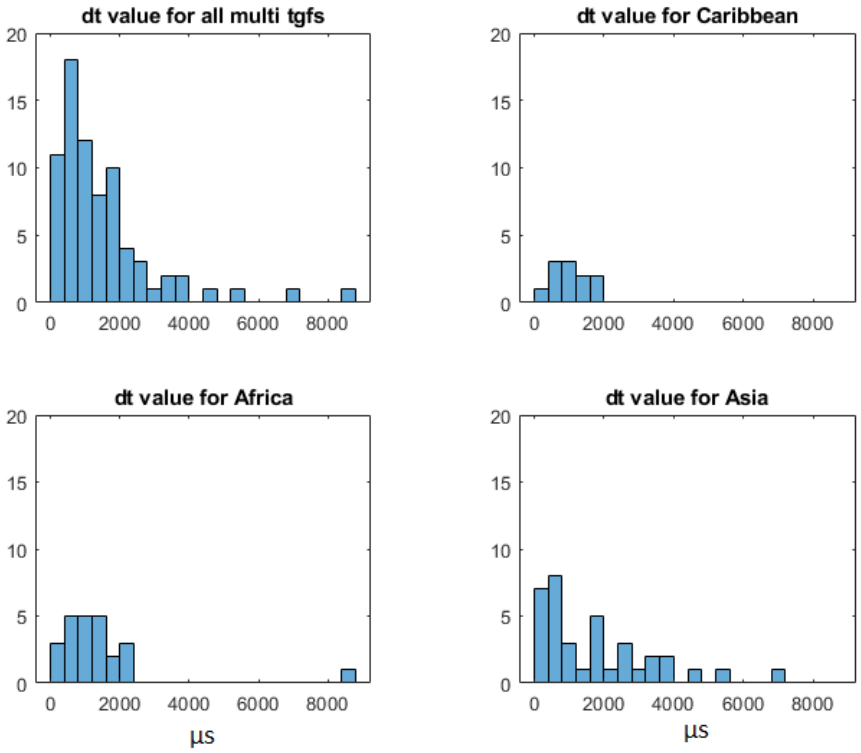

Figure 5.3: Histogram of dt values of Multi TGFs divided into regions shown in Figure 5.1, bin size 400 μs.

5.2 Different types of multi pulse TGFs

Following the procedure outlined in the methodology we will present the multi pulse TGFs as follows:

For TGFs without optical data:

1. The gamma photons as an energy scatterplot and as a histogram for HED (Figure 5.4).
2. Geographical distribution of GLD data within $+-1000s$ of the TGF. (Figure 5.5)

For TGFs with optical data:

1. The gamma photons as an energy scatterplot and as a histogram for both HED and LED. The optical data as a line plot for the photometers 337, 180-230 and 777 nm. (Figure 5.6)
2. The optical data as an image for the CHU 337, 777 nm and as line plot for the photometers 337 and 777 nm for the duration of the camera frame. (Figure 5.7)

3. Geographical distribution of GLD data within $+-1000s$ of the TGF and CHU 337 or 777 nm image projected onto geographical coordinates. (Figure 5.8)

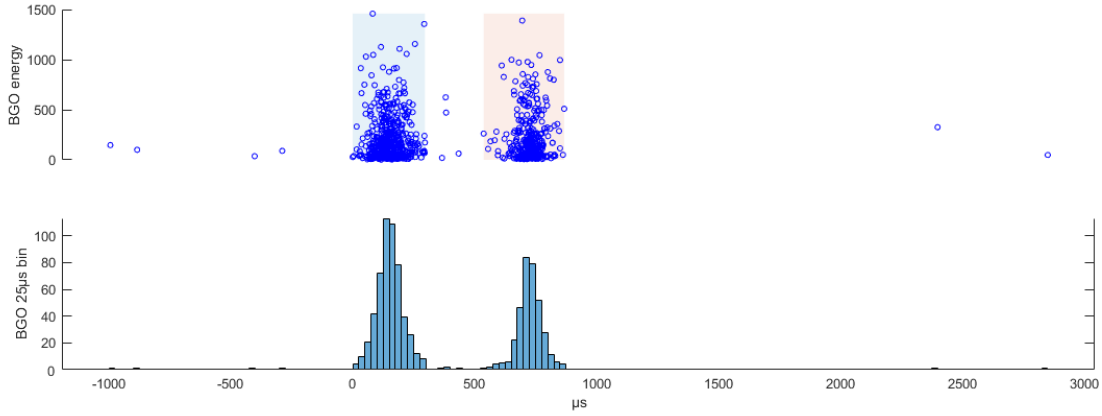

Figure 5.4: Energy scatterplot and histogram for TGF-200921, a multi pulse TGF without optical data. In this case only the MXGS HED data is displayed with a energy scatter plot for graph 1 and a counts histogram with a bin size of 25 μs for graph 2. The TGFs found are marked with a colored background on the BGO scatterplot, and cosmic rays are marked on the scatterplots by red circles instead of blue. For the energy plots the y-axis is ADC. The timescale is indicated at the bottom and is in μs.

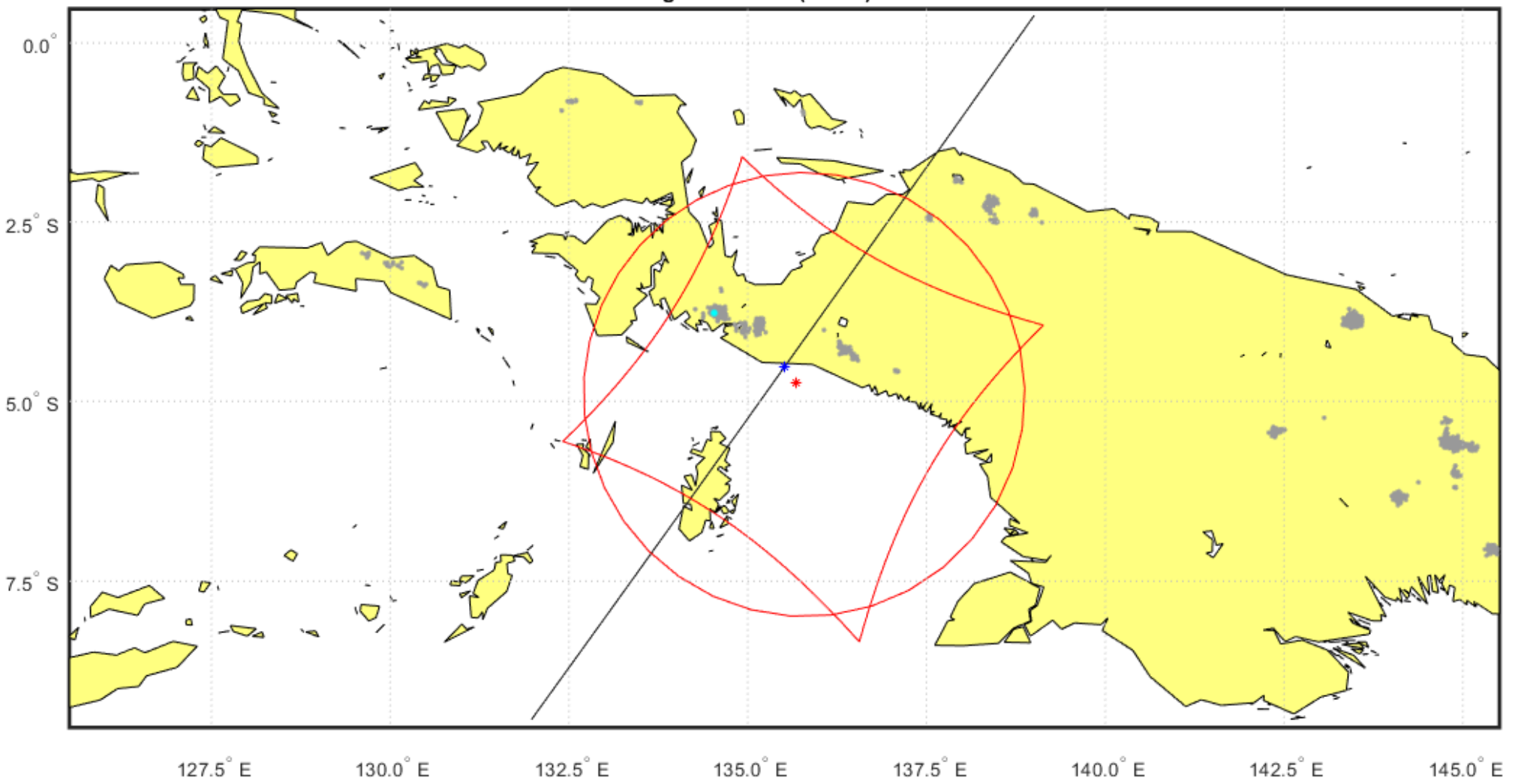
TGF-200921-06:13:33-12856
yaw = -4° pitch = -1.7° roll = 0.9°
gld distance: (137.6) km
0.0°
2.5° S
5.0° S
7.5° S
127.5° E
130.0° E
132.5° E
135.0° E
137.5° E
140.0° E
142.5° E
145.0° E

Figure 5.5: Mapping of TGF event TGF-200921. A multi pulse TGF without optical data. The ISS footpoint is indicated by a blue star, while the center of the FoV is indicated by a red star. The red ellipse indicates the FoV of the 180-230 nm photometer while the red "cushion" shape indicated the FoV of the other photometers and both CHU 337 nm and 777 nm. The black line indicates the flight path of the ISS. The white areas indicate sea or lakes, while yellow areas indicate land. The GLD sferics are marked on the map as either cyan, magenta or gray dots. The gray dots show GLD concurring within $[-1000, 1000]$ s of the TGF, the magenta dots indicate within $[-1, 1]$ s of the TGF while the cyan dots show GLD occurring within $[-10, 40]$ ms of the TGF. The top of the figure contains information about the event including the ID of the TGF, the rotation of the ISS, the distance to the $[-10, 40]$ ms GLD from the footpoint. In the annex there is additionally a version of the map without the $[-1000, 1000]$ s GLD.

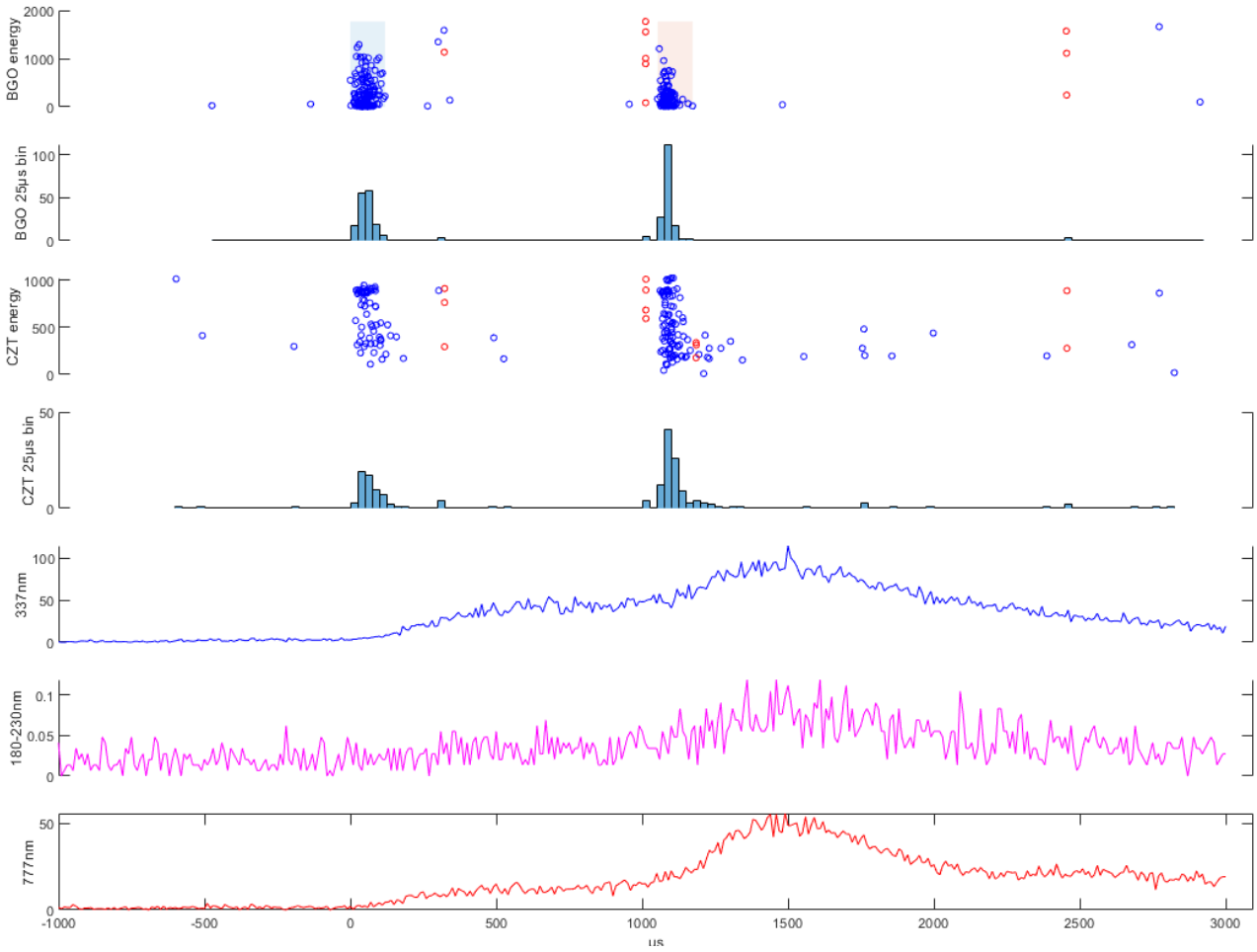

Figure 5.6: Energy scatterplot, histogram and photometer for TGF-191109, a multi pulse TGF with optical data. in addition to having the energy scatterplot and counts histogram for HED like Figure 5.4 it also has energy scatterplot and counts histogram for LED and graphs for the photometers; 337 nm in blue, 180-230 nm in magenta and 777 nm in red. For the photometer plots the y-axis is ADC.

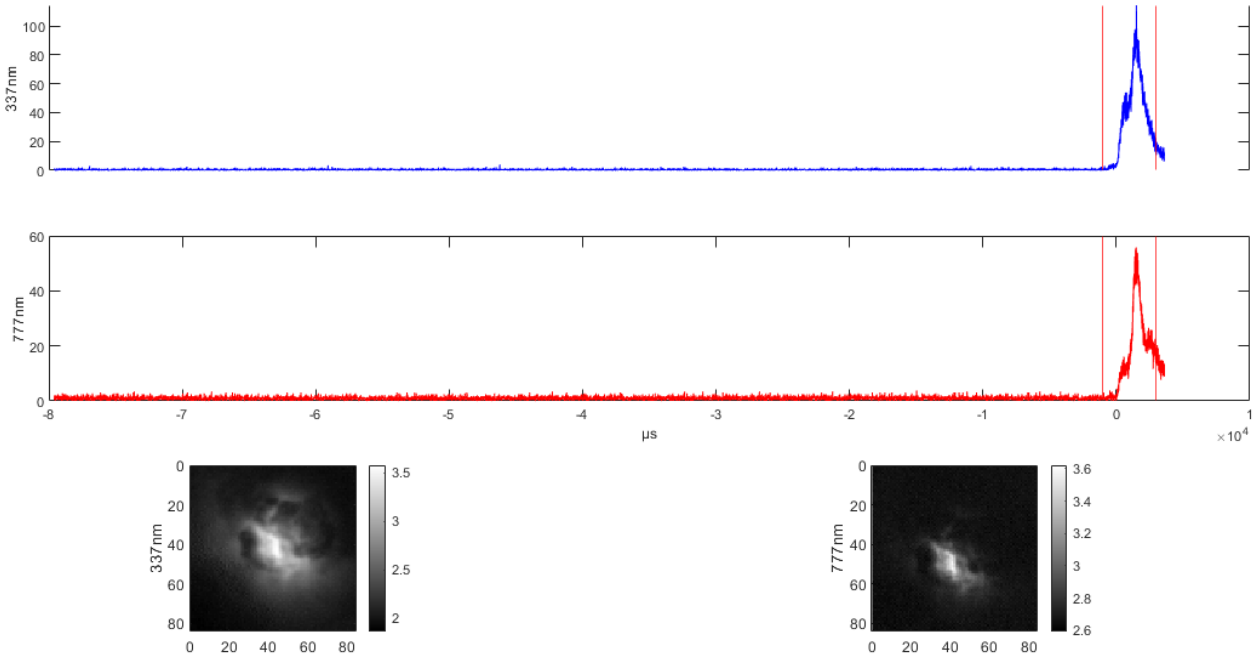

Figure 5.7: Optical data plot for TGF-191109, the graphs at the top show photometer data for 337 *nm* and 777 *nm* for the entirety of the camera frame. The red lines on the graphs indicate the interval the TGF occurred in and corresponds to the time interval shown in Figure 5.6. The images at the bottom are the CHU 337 *nm* and CHU 777 *nm* frame in which the TGF occured. The brightness scale for the images are logarithmic. For some events the TGFs occur between two camera frames, in these cases the split between frames are indicated by a black line in the photometer graph.

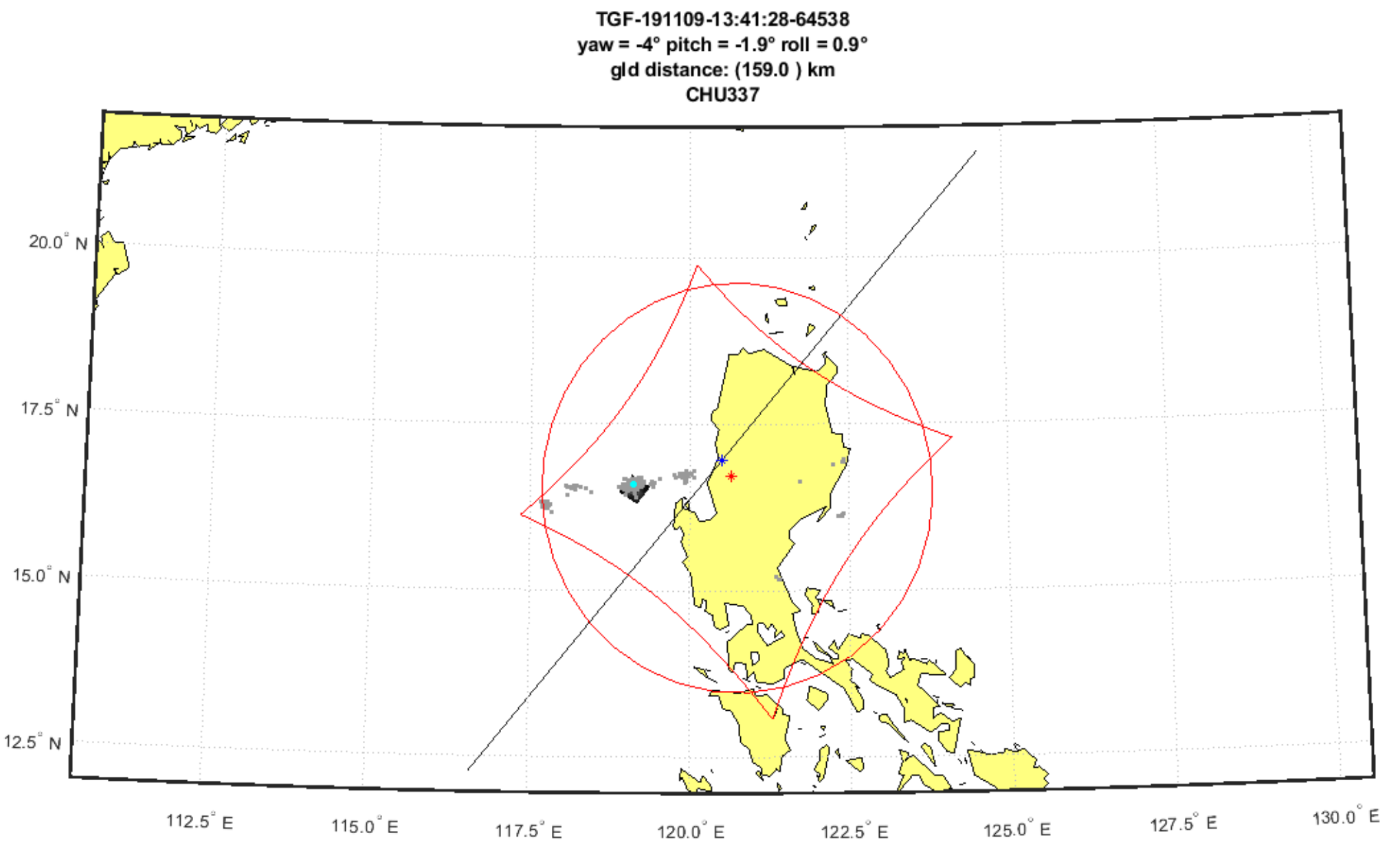
TGF-191109-13:41:28-64538
yaw = -4° pitch = -1.9° roll = 0.9°
gld distance: (159.0) km
CHU337
20.0° N
17.5° N
15.0° N
12.5° N
112.5° E
115.0° E
117.5° E
120.0° E
122.5° E
125.0° E
127.5° E
130.0° E

Figure 5.8: Mapping of TGF event TGF-191109. A multi pulse TGF with optical data. In addition to the features described in Figure 5.5 the CHU image for the frame of the TGF is projected onto the map with the method described in section 4.2. Which CHU is used for the mapping is noted on the top of the figure.

From the MXGS HED data it was noticed that multi pulse TGFs tend to follow three types of patterns in the energy and counts.

1. Events with two peaks of similar intensity.
2. Events where subsequent pulses have decreasing counts
3. Events where subsequent pulses have increasing counts

From grouping the multi pulse TGFs based on these categories it was found that:

Group	# of possible	# of clear
Similar Intensity	10	7
Decreasing	25	19
Increasing	9	6
Other	20	8

Tabel 5.1: Amount of multi pulse TGFs within each grouping. Showing the number of possible events that may fit into the group and the number of events that clearly fit into the group. The other category includes TGFs that are too weak to group, and TGFs that do not fit any of the groupings. Tabel 5.2 to Tabel 5.7 show the data for the "# of possible" TGFs based on grouping.

Figure 5.9 to Figure 5.20 below show examples of multi pulse TGFs that distinctly match the three groupings but not all multi pulse TGFs where this clear.

Tabel 5.4 to Tabel 5.7 below contain information about the multi pulse TGFs that where found based on this grouping. For each group the first Table (Table 5.2, 5.4, 5.6) contains the TGFs that have optical data, while the second Table (Table 5.3, 5.5, 5.7) contains the TGFs that do not have optical data.

Which group they are included in is indicated under "TGF group" with 1. similar intensity, 2. decreasing, 3. increasing and 4. other. For cases where the group is uncertain they are indicated as 1/4, 2/4 or 3/4.
The likely optical pulse associations are indicated under "Optical group" with the values meaning: 1. optical pulse associated with each peak, 2. optical pulse associated with one peak, 3. no associated optical pulse. Optical pulse associations that are uncertain are indicated as either 1/3 or 2/3.
The likely GLD associations are indicated under "GLD group" with the values meaning: 1. Likely GLD within $[-10, 40]$ ms, 2. multiple likely GLD within $[-10, 40]$ ms, 3. uncertain if GLD is associated and 4. no associated GLD sferic.

For some events the amount of peaks where uncertain, for these cases the originally determined amount of peaks from the procedure in 4.1 is sett in the table with other possible peak amounts in parenthesis.
It should also be noted that the optical rise times noted in the tables are from the TGF onset until the optical peak.

5.2.1 Two peaks of similar intensity

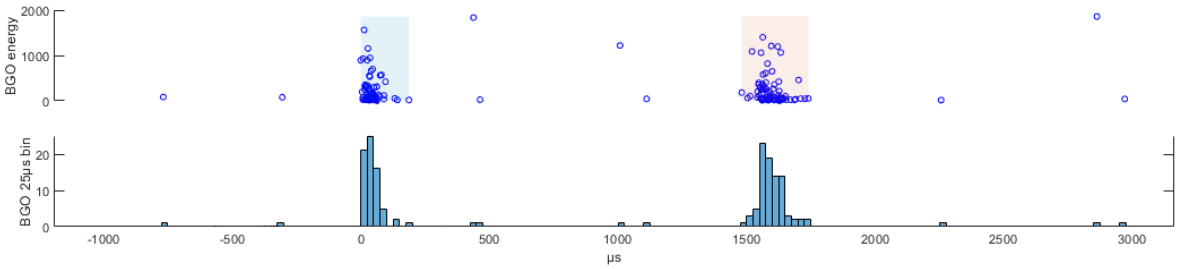

Figure 5.9: 18/08/30-06:53:37

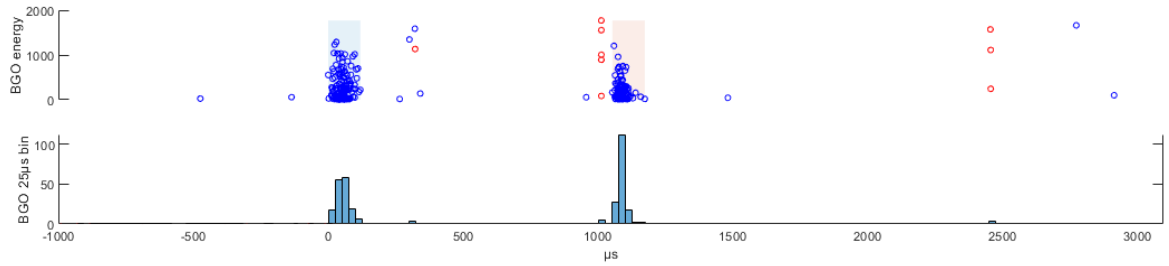

Figure 5.10: 19/11/09-13:41:28

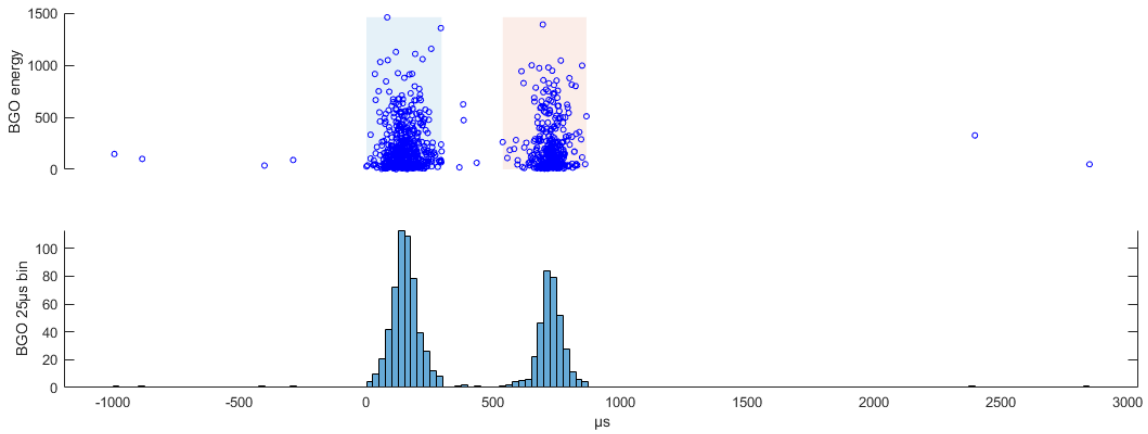

Figure 5.11: 20/09/21-06:13:33

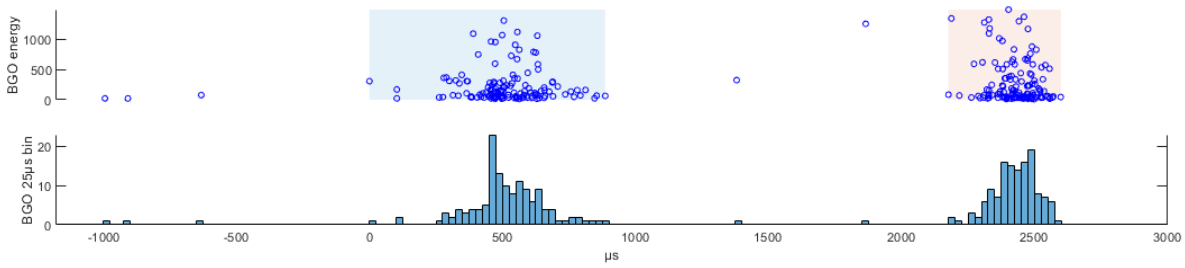

Figure 5.12: 21/05/07-18:20:25

Figure 5.9 to Figure 5.12 shows an example of four multi pulse TGFs that have two peaks of similar intensity. In total 10 multi pulse TGFs where found that may match this group, with 7 having very clearly two peaks of similar intensity.

TGFs with optical data:

Date and time	Peaks	# of counts	% of counts >1000 ADC	TGF dt μs	TGF duration μs	ISS footpoint		TGF group	Optical group	Optical signal from peak #	Photometer peak ADC		Optical rise time μs	CHU brightness $\mu W/m^2Sr$		GLD group	Distance to GLD km	GLD peak current kA	dt TGF to GLD ms
						Lat	Lon				337 nm	777 nm		337 nm	777 nm				
18/03/30-06:53:37	2	70, 88	2.9, 6.8	1481	187, 259	8.3291	-65.7899	1	1	1, 2	50, 40	20, 20	1000, 500	3160	2000	1	137.9	21	25.8
19/11/09-13:41:28	2	155, 162	5.2, 0.6	1053	119, 120	16.9599	120.5065	1	1	1, 2	80, 170	50, 140	500, 500	3160	3980	1	159.0	-129	20.0
21/05/07-18:20:25	2	136, 132	3.7, 7.6	2176	886, 422	6.6406	47.0008	1	2	2	50	40	750	3980	1580	1	117.0	24	22.3

Table 5.2: Data for multi pulse TGFs with two peaks of similar intensity, for events with optical data.

TGFs without optical data:

Date and time	Peaks	# of counts	% of counts >1000 ADC	TGF dt μs	TGF duration μs	ISS footpoint		TGF group	GLD group	Distance to GLD km	GLD peak current kA	dt TGF to GLD ms
						Lat	Lon					
18/06/21-16:00:53	6 (2/5)	158, 39, 38, 26, 15, 192	8.9, 5.1, 13.2, 15.4, 6.7, 4.7	333, 474, 476, 430, 383	312, 145, 319, 353, 166, 298	6.4436	21.2559	4/1	1	57.6	234	8.7
18/09/27-20:19:05	2 (1)	257, 252	3.9, 1.6	120	120, 175	24.4206	-63.2904	1	4			
19/07/31-04:57:25	3	41, 10, 32	4.9, 0, 9.4	937, 848	250, 157, 61	-1.5003	-58.8311	1	2	248.3, 246.4	34, 14	11.8, 13.7
19/08/22-22:14:01	2	27, 20	0, 0	186	101, 70	22.8648	105.1296	4/1	4			
20/03/14-07:40:31	3	30, 30, 18	0, 0, 0	3797, 1524	724, 1104, 558	-13.4128	159.5197	4/1	3	458.1	10	12.9
20/09/21-06:13:33	2	534, 350	1.5, 0.6	537	296, 330	-4.5233	135.5131	1	1	137.6	28	14.3
22/06/21-06:35:27	2	144, 72	3.5, 4.2	910	510, 152	14.1809	116.5607	1	2	61.0, 68.3	28, -12	13.6, 17.5

Table 5.3: Data for multi pulse TGFs with two peaks of similar intensity, for events without optical data.

5.2.2 Decreasing Intensity

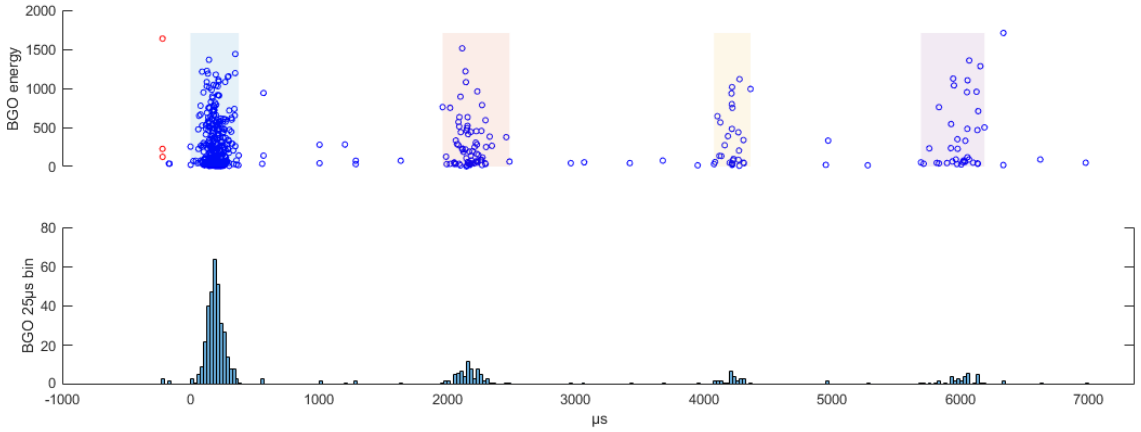

Figure 5.13: 18/10/22-06:47:04

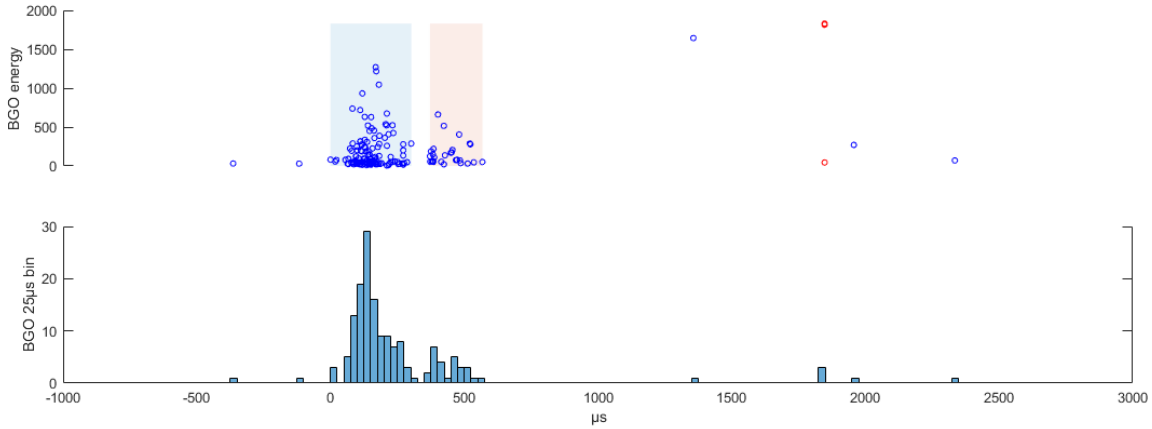

Figure 5.14: 20/10/28-06:05:02

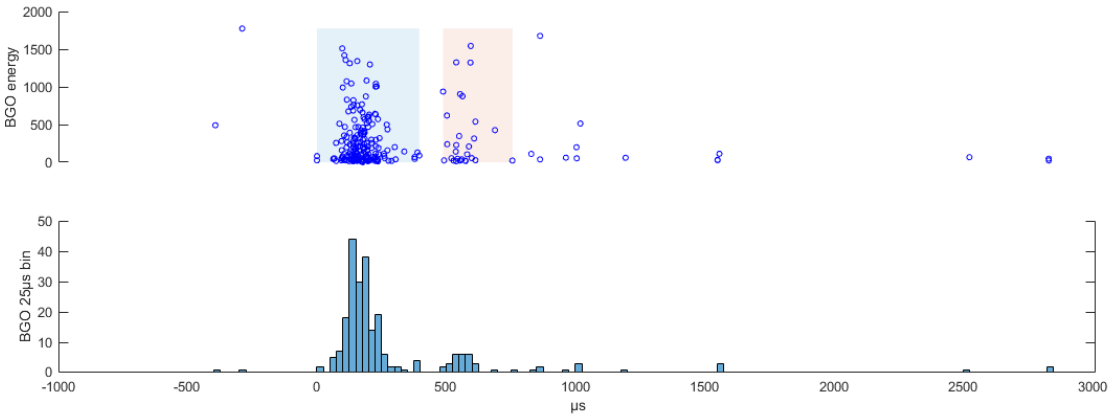

Figure 5.15: 21/08/01-18:28:29

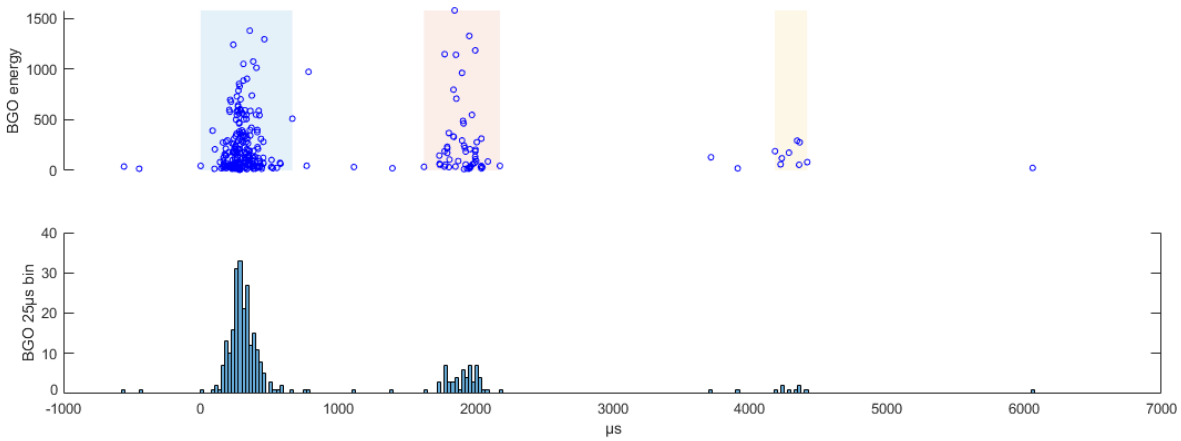

Figure 5.16: 21/11/20-15:48:30

Figure 5.13 to Figure 5.16 shows an example of four multi pulse TGFs that have decreasing intensity from the first peak. In total 25 multi pulse TGFs where found that may fit into this group, with 19 having a clear decrease in intensity after the first peak.

TGFs with optical data:

Date and time	Peaks	# of counts	% of counts >1000 ADC	TGF dt μs	TGF duration μs	ISS footpoint		TGF group	Optical group	Optical signal from peak #	Photometer peak ADC		Optical rise time μs	CHU brightness $\mu W/m^2Sr$		GLD group	Distance to GLD km	GLD peak current kA	dt TGF to GLD ms
						Lat	Lon				337 nm	777 nm		337 nm	777 nm				
19/04/24-23:22:21	3	33, 7, 16	0, 14.3, 6.3	1078, 759	182, 76, 70	-32.2737	32.6093	4/2	3							3	156.5	4	34.1
21/03/01-05:07:27	2	54, 21	1.9, 4.8	760	300, 261	3.3843	-76.6611	2	2/3	2	40	20	1250	3160	1000	3	147.2	51	14.2
21/05/07-21:25:49	2	33, 11	0, 0	1598	433, 194	5.4221	-1.0878	4/2	3							1	484.8	10	31.1
21/12/30-17:57:41	2	225, 19	0.9, 0	759	339, 148	-16.1194	68.7562	2	2	2	60	20	1000	630	630	1	153.7	48	12.2

Table 5.4: Data for multi pulse TGFs with decreasing intensity, for events with optical data.

TGFs without optical data:

Date and time	Peaks	# of counts	% of counts >1000 ADC	TGF dt μs	TGF duration μs	ISS footpoint		TGF group	GLD group	Distance to GLD km	GLD peak current kA	dt TGF to GLD ms
						Lat	Lon					
18/06/28-03:50:05	2	51, 7	5.9, 14.3	472	246, 104	16.8968	156.4528	4/2	1	180.4	61	29.2
18/09/19-13:09:58	2	110, 62	6.4, 9.7	342	275, 297	20.3842	89.5708	2	1	206.8	12	24.2
18/10/17-22:32:05	2	118, 9	3.4, 0	518	305, 188	3.3933	-60.0646	2	1	189.4	-30	-8.5
18/10/22-06:47:04	4	334, 72, 28, 36	5.4, 4.2, 7.1, 13.9	1996, 2115, 1614	376, 521, 285, 495	7.7363	-20.9288	2	2	98.2, 95.2	-27, -29	15.1, 27.5
19/02/04-22:04:29	2 (1)	160, 52	6.9, 7.7	1474	1376, 1010	-4.1427	16.3763	4/2	1	126.5	28	24.5
19/02/25-06:02:41	2 (1)	80, 16	6.3, 6.3	297	269, 109	-9.7719	140.0843	2	4			
19/04/16-17:03:42	2	65, 14	7.7, 21.4	2059	477, 271	-2.3997	28.2116	2	1	98.1	34	25.4
19/07/12-01:38:48	3	39, 14, 10	5.1, 14.3, 0	1779, 2504	388, 478, 437	5.3439	99.2309	2	1	60.8	11	15.7
19/07/12-01:39:42	3	78, 7, 10	2.6, 0, 0	660, 245	332, 85, 137	2.6223	101.1608	2	1	158.1	28	14.8
19/08/03-05:00:08	2	89, 27	4.5, 11.1	1866	446, 268	26.4489	124.4969	2	1	128.6	34	15.7
19/09/13-11:23:14	2	33, 14	6.1, 14.3	1938	93, 264	30.6533	-87.4078	2	2	209.1, 208.6	59, 6	20.4, 20.8
19/10/21-15:32:49	3	102, 9, 18	2.0, 0, 13.6	531, 373	182, 134, 392	-7.1857	16.8986	2	1	251.39	-24	4.0
19/10/21-20:57:32	2	45, 7	4.4, 0	413	155, 39	6.4176	113.7646	2	2	144.8, 138.2	21, 29	21.8, 29.9
19/11/20-20:23:57	2	90, 9	6.7, 0	849	487, 214	2.4610	-59.0551	2	1	206.5	24	1.9
20/10/28-06:05:02	2	122, 27	2.5, 0	372	302, 196	17.4331	87.4288	2	4			
21/03/17-03:29:47	3 (1)	50, 56, 12	2, 5.4, 0	739, 1041	669, 951, 140	-9.9675	-157.3703	4/2	2	285.4, 278.5	13, 15	24.2, 29.2
21/08/01-18:28:29	2	192, 28	6.3, 10.7	488	396, 268	10.8739	-101.6974	2	4			
21/11/20-15:48:30	3	222, 56, 8	2.7, 8.9, 0	1627, 2557	668, 553, 235	-11.2412	-178.9852	2	1	32.1	6	21.3
22/01/09-10:07:02	2	88, 14	5.7, 7.1	5506	605, 705	-10.8994	133.4041	2	4			
22/07/12-14:13:50	2	37, 14	0, 0	539	244, 284	17.6444	81.3366	4/2				
22/10/05-12:35:41	2	34, 10	0, 0	1434	189, 87	5.2492	122.6959	2				

Table 5.5: Data for multi pulse TGFs with decreasing intensity, for events without optical data.

5.2.3 Increasing Intensity

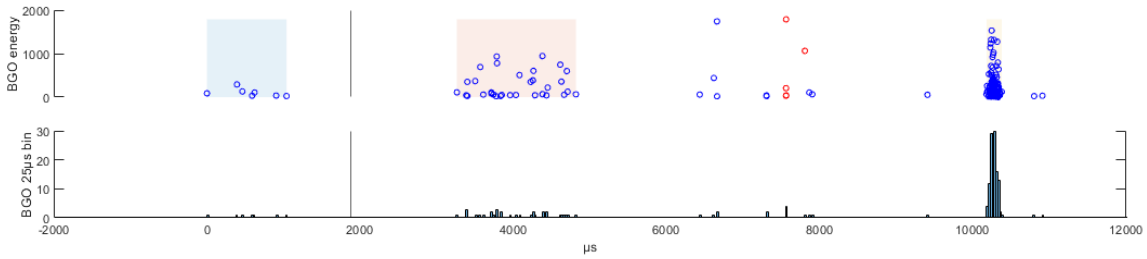

Figure 5.17: 20/07/11-12:48:33

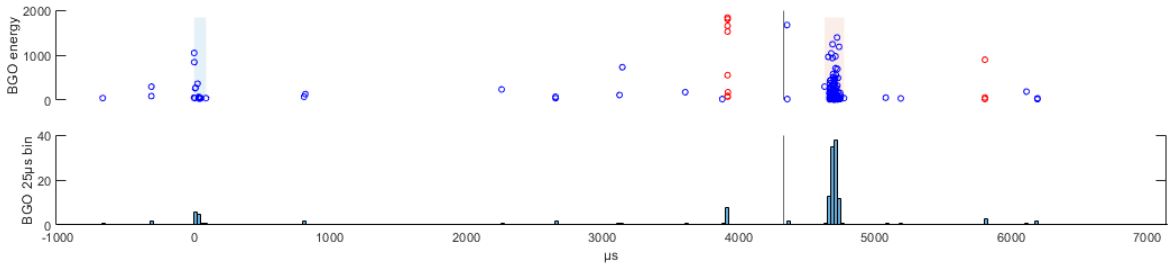

Figure 5.18: 21/10/21-14:48:50

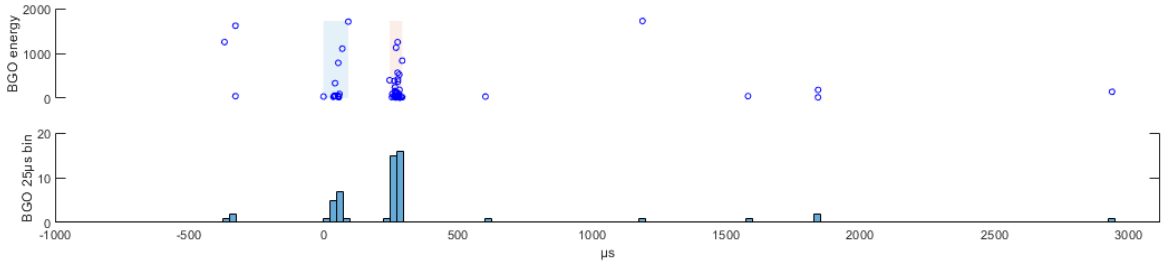

Figure 5.19: 22/06/27-11:56:02

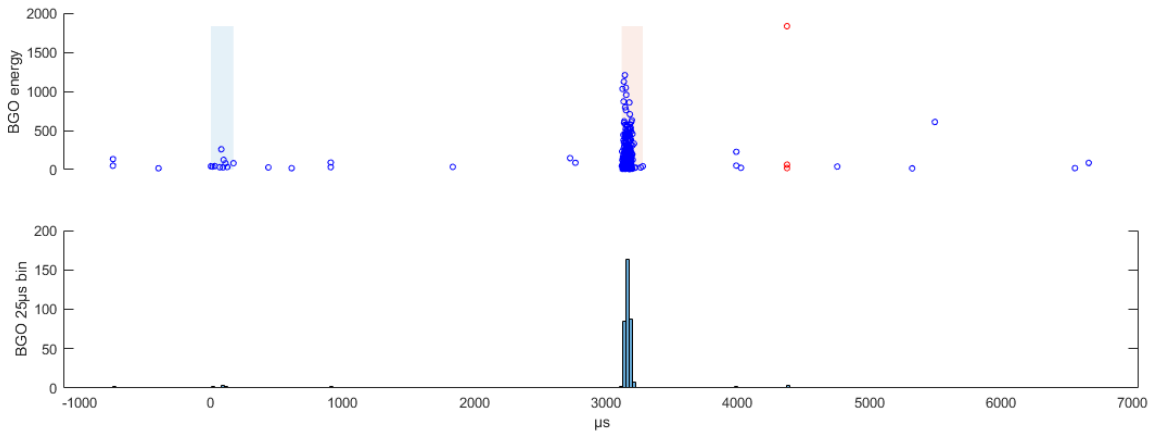

Figure 5.20: 22/12/12-10:07:15

Figure 5.17 to Figure 5.20 shows an example of four multi pulse TGFs that have increasing intensity until a last bright peak. In total 9 multi pulse TGFs where found that may fit into this group, with 6 having a clear increase in intensity until a last bright peak.

TGFs with optical data:

Date and time	Peaks	# of counts	% of counts >1000 ADC	TGF dt μs	TGF duration μs	ISS footpoint		TGF group	Optical group	Optical signal from peak #	Photometer peak ADC		Optical rise time μs	CHU brightness $\mu W/m^2Sr$		GLD group	Distance to GLD km	GLD peak current kA	dt TGF to GLD ms
						Lat	Lon				337 nm	777 nm		337 nm	777 nm				
20/04/27-03:09:52	2	21, 57	4.8, 1.8	1155	461, 280	6.7041	-16.5757	3	2/3	2	50	20	1500	1000	790	3	230.3	48	23.6
20/07/11-12:48:33	3 (2)	7, 32, 136	0, 0, 5.1	3263, 6914	1039, 1553, 198	16.2550	119.2081	3	2	3	80	100	500	3160	2510	3	108.5	15	-20.1
21/05/10-12:51:32	2	16, 16	0, 0	914	503, 209	-4.6298	103.8671	4/3	3/2	2	4	4	750			4			
21/10/21-14:48:50	2	13, 100	7.7, 4.0	4628	87, 143	-12.0978	175.3834	3	1	1, 2	40, 40	10, 10	750, 750	3160	31620	2	267.1, 272.0	-66, -15	21.4, 36.7
22/06/27-11:56:02	2	14, 32	14.3, 6.3	246	92, 47	-13.6420	179.9227	3	3							3	68.7	22	42.7

Table 5.6: Data for multi pulse TGFs with increasing intensity, for events with optical data.

TGFs without optical data:

Date and time	Peaks	# of counts	% of counts >1000 ADC	TGF dt μs	TGF duration μs	ISS footpoint		TGF group	GLD group	Distance to GLD km	GLD peak current kA	dt TGF to GLD ms
						Lat	Lon					
18/08/18-12:25:10	2	14, 38	7.1, 7.9	1924	344, 705	6.0609	-80.2494	4/3	2	80.4, 100.2	12, 20	-8.3, 35.4
19/10/15-23:19:23	2	49, 189	2.0, 2.6	1307	64, 116	6.4098	-76.7814	3	2	128.6, 189.0	40, -14	8.4, 14.0
22/01/08-09:19:03	2	5, 14	0, 0	753	122, 79	-18.0312	145.4068	4/3	1	630.0	5, 54	-9.0
22/12/12-10:07:15	2	10, 348	0, 1.1	3120	171, 160	4.4754	117.2013	3				

Table 5.7: Data for multi pulse TGFs with increasing intensity, for events without optical data.

5.3 Optical Data and GLD association

16 out of the 52 multi pulse TGFs had optical data. The TGF that do not have optical data are due to being obtained during daytime, when both MMIA and MXGS LED is turned off.

For each multi pulse TGF a consistency check was preformed based on the TGF characteristics as described in 4.3. This gives a rough estimate of the radial distance of the TGF and if it is likely that the TGF occurred outside the FoV or inside the FoV. Then using the mapping of the events as seen in Figure 5.5 and Figure 5.8, optical data and GLD sferics that do not match the expected distance of the TGF could be discarded. For events with optical data by inspecting the timing of the optical pulse compared to the TGF (as seen in Figure 5.6 and Figure 5.7), optical pulses that occurred outside of the time window of the TGF could also be discarded.

For optical associations it was found:

Optical association	# of events
Each peak	3
Multiple peaks	1
One peak	3
Uncertain	3
No association	6

Table 5.8: Amount of multi pulse TGFs with optical pulses associated to TGF peaks.

The three events with a optical pulse associated with each peak were all double pulse TGFs and the event with multiple optical peaks associated was TGF 21/12/09-18:09:13 (Figure 6.15) which had three peaks, two of which were associated with an optical pulse.
For the three events with one associated optical pulse, all had the optical pulse associated with the last peak of the multi pulse TGF.
The uncertain events all had a possible optical peak associated to the last pulse, but based on the TGF characteristics it was uncertain if the optical pulse was associated.
The last six events where determined to have no associated optical pulse this was either due to: 1) No optical pulses occurring in the TGF time window, likely because the TGF occurred outside the FoV. 2) The TGF characteristics indicated that the TGF was unlikely to be from the position given by the CHU data.

For GLD associations it was found:

Association	# of events
One likely within -10, 40 ms	20
Multiple likely within -10, 40 ms	9
Uncertain	7
No association	16

Table 5.9: Amount of multi pulse TGFs with GLD sferics associated to event.

Most of the multi pulse TGFs had one likely GLD sferic associated and for cases with optical data there usually was a GLD sferic which closely matched the CHU data position. For the events with multiple likely GLD associations for most of the events the likely GLD sferics where from about the same location, while two of the events TGF 18/08/18-23:25:10 (not shwon) and TGF 19/10/15-23:19:23 (not shown) had likely GLD sferics that were tens of km apart.

Chapter 6

Discussion

This chapter will discuss the results presented in chapter 5. This includes the distribution of multi pulse TGFs, the peak value of the time between TGF onsets dt and the duration of multi pulse TGFs in comparison with lightning leader propagation times. In addition we will discuss the multi pulse TGFs with associated optical data and some other notable multi pulse TGFs.

6.1 Multi pulse TGF distribution

Since the launch of ASIM until the end of 2022, ASIM has detected 1428 TGFs. 52 or 3.6% of the total TGFs where identified as multi pulse TGFs. The amount of multi pulse TGFs by the region distribution shown in Figure 5.1 and Figure 5.2:

Region	Amount TGFs		Multi pulse TGF	
	# of TGF	% of total	# of TGF	% of region
Caribbean	419	29.3	10	2.4
Africa	277	19.4	11	4.0
South east Asia	611	42.8	28	4.6
Outside	121	8.5	3	2.5

Table 6.1: Distribution of TGFs and multi pulse TGFs by regions shown in shown in Figure 5.1 and Figure 5.2.

There are some differences in the amount of multi pulse TGFs compared to total amount of TGFs based on region, with Africa and south east Asia quite similar at 4% and 4.6% while the Caribbean has a lower value at 2.4%. However we do not have enough events to be able to determine this difference as statistically significant.

From Figure 5.3 it can be seen that the distribution of dt (time between onsets of TGFs) has a peak between 400-800 μs after which the dt value decreases exponentially. The largest dt value is found to be at 8758 μs. We did not have enough events to determine if there was a difference in the distribution of the dt value based on regions.

Cummer S. A. et al. [2015] studied the time of the TGF relative to leader propagation in positive intra cloud (IC+) lightning and found that TGFs

appeared to occur midway through the lightning leader ascension and that the time for vertical propagation for negative leaders in IC+ lightning ranged from 3.3 ms to 5.2 ms. It should be mentioned that Cummer S. A. et al. [2015] analyzed a relatively small set of events so some leeway should be given to the exact timing of the leader propagation.

By taking the time from the onset of the first TGF until the onset of the last TGF of the multi pulse TGFs we found the time separation of multi pulse TGFs to be generally consistent with the results from Cummer S. A. et al. [2015]. Figure 6.1 shows that most multi pulse TGFs have a time separation below 2.3 ms with some events having time separations up to 6 ms. This shows that the time separation of most multi pulse TGFs are on the same scale as the propagation time of IC+ lightning leaders. There were however two multi pulse TGFs with time separations at around 10 ms, which is longer than what Cummer S. A. et al. [2015] suggested, and needs to be investigated further.

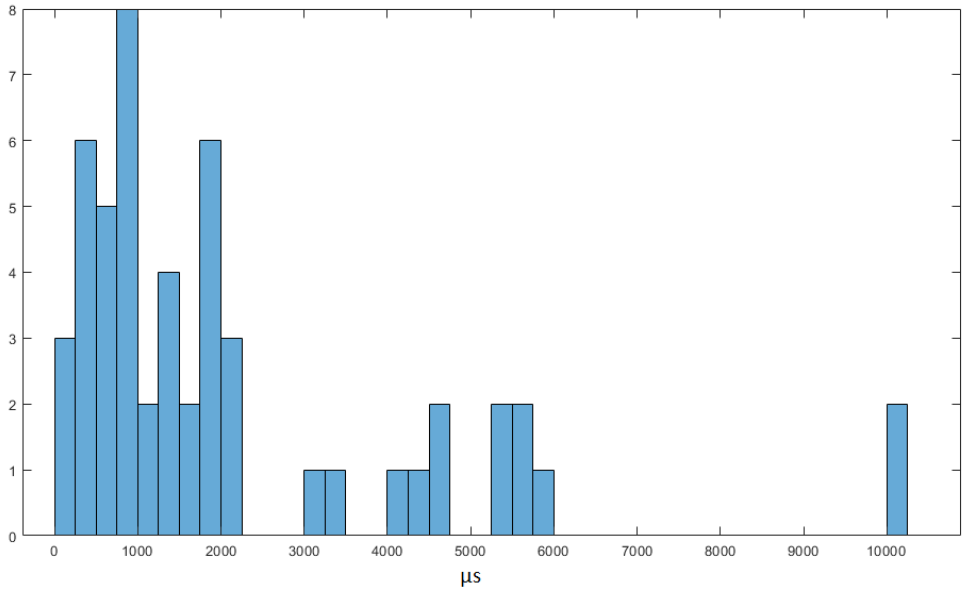

Figure 6.1: 250 μs bin histogram showing time from the onset of the first TGF until the onset of the last TGF.

6.2 Characteristics of different types of multi pulse TGFs

Based on the grouping it was found that multi pulse TGFs with a decreasing intensity from subsequent peaks appears to be the most common type of multi pulse TGF, having 25 events that could fit into this group and 19 events that clearly followed this pattern.
Events with two or more peaks of similar intensity and events with increasing intensity both had around the same number of events.

Skeie C. A. et al. [2022] and Heumsesser M. et al. [2021] studied the temporal

relationship between TGFs and associated optical pulses and found TGFs are always before the optical pulse.

For the multi pulse TGFs with associated optical pulses studied in this thesis the optical pulse always occurred after a TGF in agreement with the results found by [Skeie C. A. et al. 2022] and [Heumsesser M. et al. 2021].
For all seven events associated with optical pulses there was always an optical pulse after the last TGF peak, while the four cases that had multiple associated optical pulses all had two optical pulses, one after the second last TGF and another after the last TGF peak.

As stated by Skeie C. A. et al. [2022] optical pulses can be separated into pre-activity and main rise. The pre-activity appears as a weak optical signal slightly higher than the background and is thought to be optical emissions from the propagating lightning leader. The main rise comes from a large current pulse heating up the leader channel causing a strong optical pulse to be emitted. [Østgaard et al. 2019]

6.2.1 Two peaks of similar intensity

For multi pulse TGFs with two peaks of similar intensity, generally all events have two peaks. Three of the events have more than two peaks being TGF 18/06/21-16:00:53 (Figure 6.17), TGF 19/07/31-04:57:25 (not shown) which have weak TGFs occurring in between the two peaks of similar intensity and TGF 20/03/14-07:40:31 (not shown) which has a weak TGF occurring after the two peaks of similar intensity. There where no events observed with three or more peaks of similar intensity.

There where three events with optical data, each of which had an associated optical pulse and GLD sferic. TGF 18/08/30-06:53:37 and TGF 19/11/09-13:41:28 (Figure 6.2, Figure 6.4) had optical pulses associated with both peaks, while TGF 21/05/07-18:02:25 (Figure 6.6) had an optical pulse associated with the last peak. All three events had a likely associated GLD sferic that matched closely with the optic location.

From Figure 6.3, Figure 6.5 and Figure 6.7 we can see that the optical signal for each event came from one spot and ranges in size from about 5-15 pixels wide in the CHU which corresponds roughly to 2-6 km. This spread in the optical location can be explained by the light from the leader being scattered in the cloud. The dt value for these three events is between 1-2 ms which is within the time the leader takes to propagate found by Cummer S. A. et al. [2015]. For these events it is reasonable to believe that TGFs are produced by the same leader as it propagates through the cloud.

TGF 18/08/30-06:53:37 and TGF 19/11/09-13:41:28 (Figure 6.2, Figure 6.4) it appears that both TGFs occur during pre-activity, when the first TGF occurs a slight increase in the optical activity can be seen in Figure 6.3 and Figure 6.5 followed by the main rise shortly after. For both events the second TGF occurs after the peak of the first optical pulse has passed but before the second optical pulse occurs, this is likely around the same time as the

pre-activity of the second pulse.

In the case of TGF 21/05/07-18:02:25 (Figure 6.6) there is no optical pulse associated with the first peak It is unlikely that the first TGF is from outside the FoV due to the brightness and high energies. Figure 6.6 shows some weak optical activity occurring during the time of the first TGF, which could indicate pre-activity.

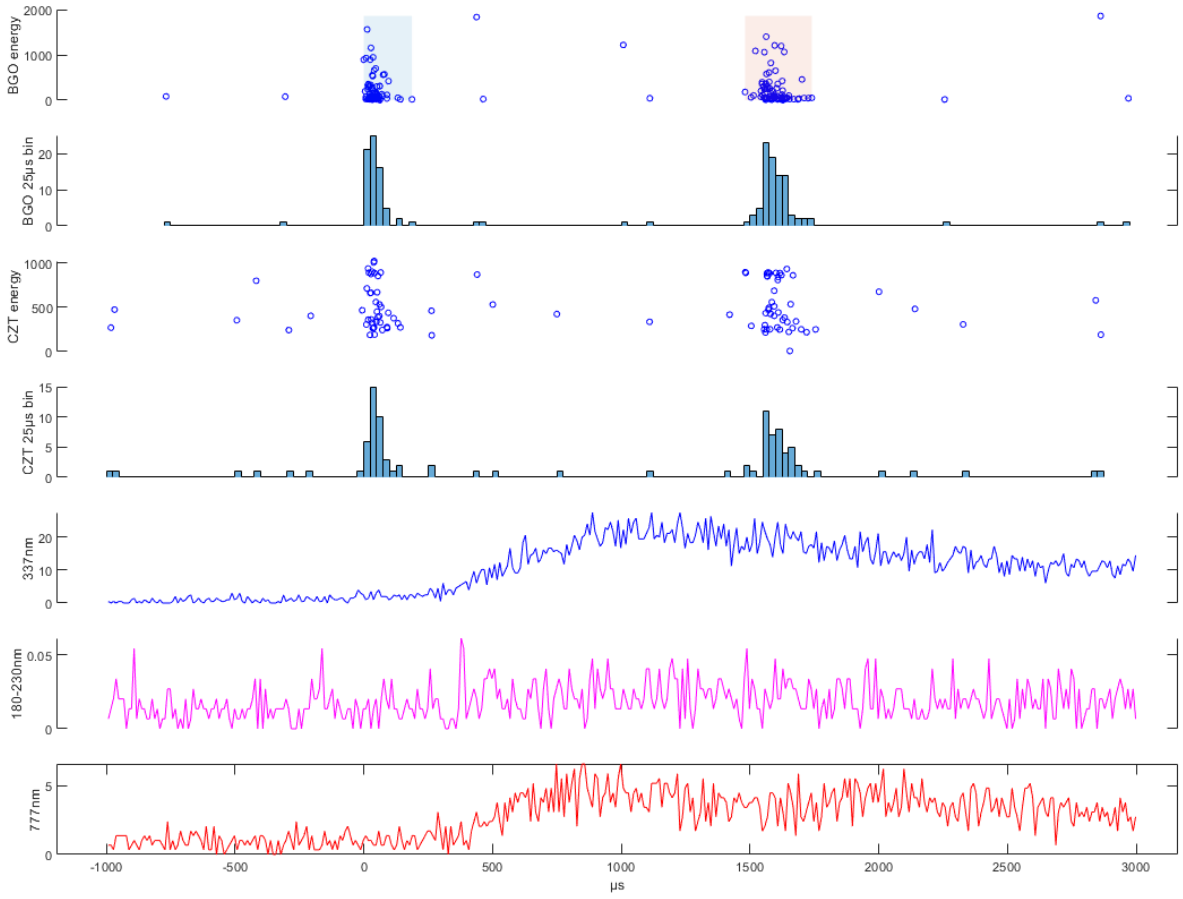

Figure 6.2: Energy scatterplot, histogram for HED and LED and lineplot for photometers of TGF 18/08/30-06:53:37.

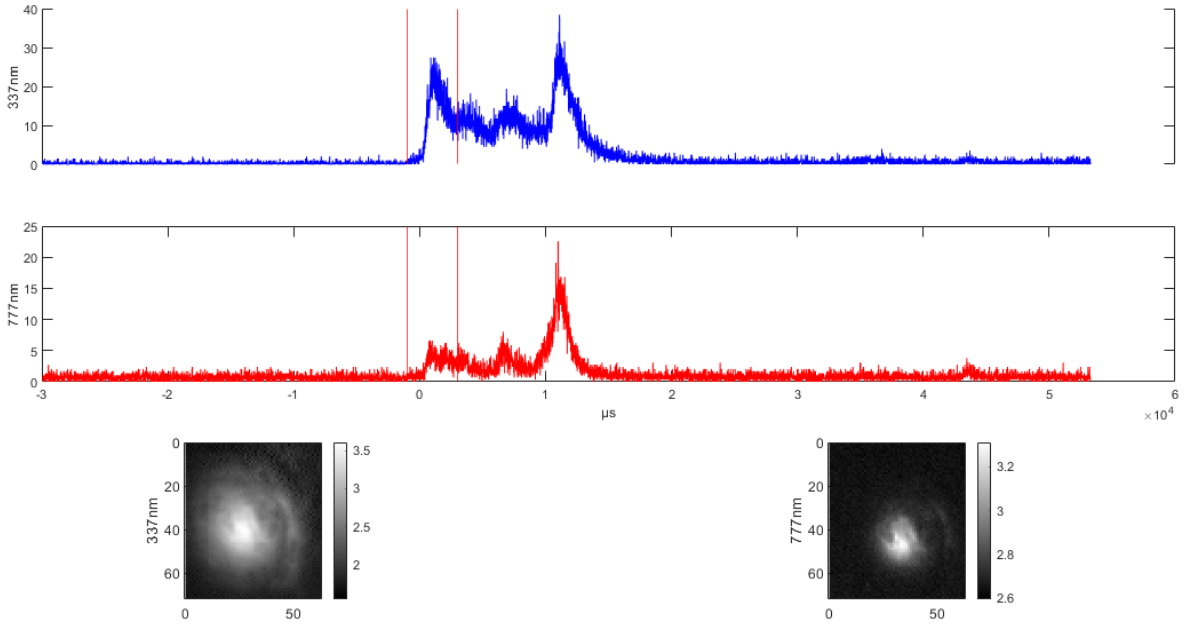

Figure 6.3: Lineplot for both frames of photometer 337 and 777 nm and camera frames for CHU 337 and 777 nm, of TGF 18/08/30-06:53:37. The red lines indicate the time interval shown in Figure 6.2.

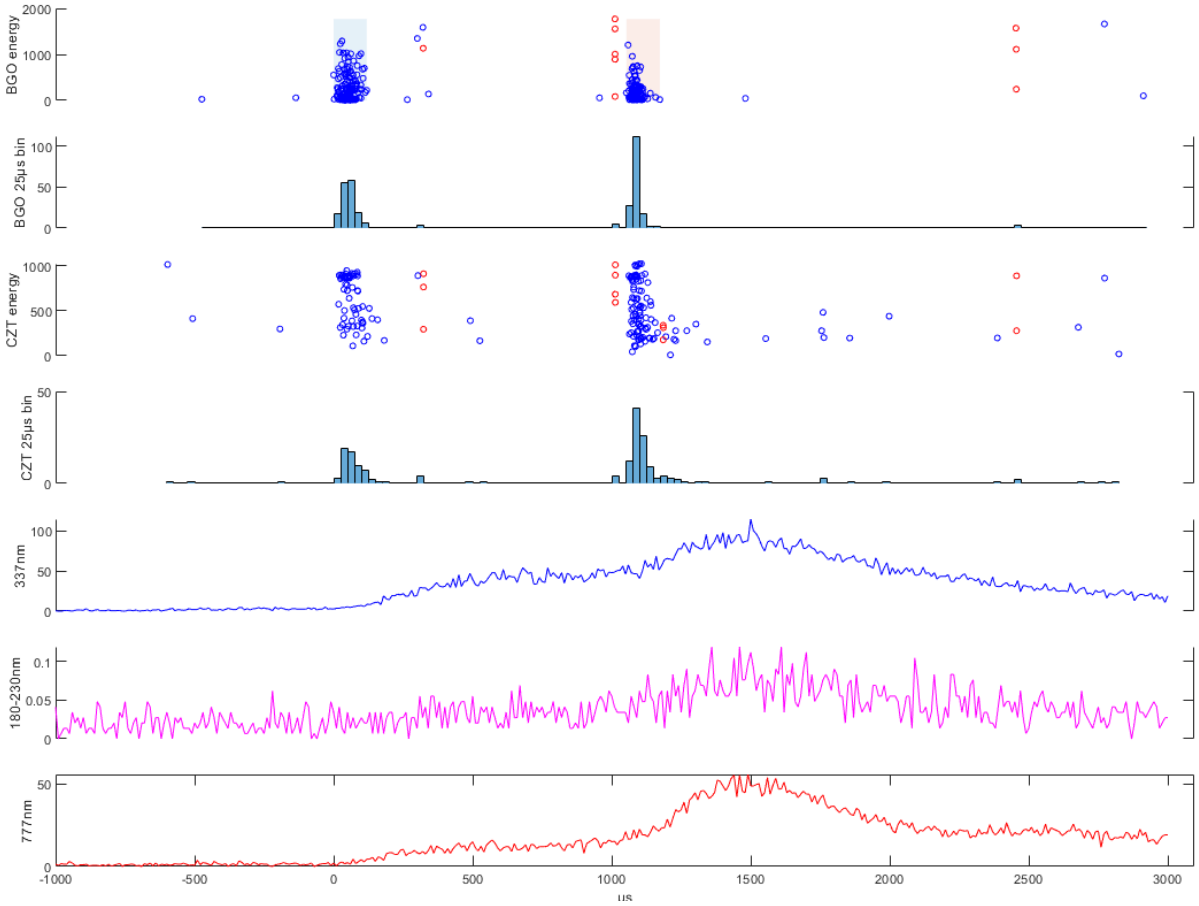

Figure 6.4: Energy scatterplot, histogram for HED and LED and lineplot for photometers of TGF 19/11/09-13:41:28.

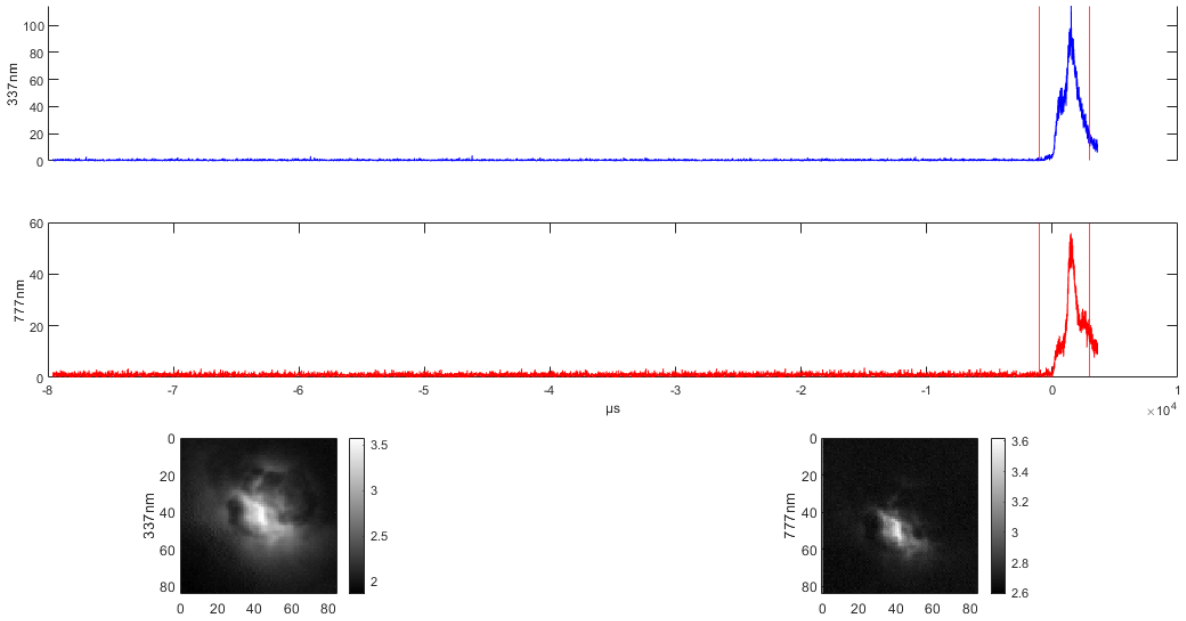

Figure 6.5: Lineplot for both frames of photometer 337 and 777 nm and camera frames for CHU 337 and 777 nm, of TGF 19/11/09-13:41:28. The red lines indicate the time interval shown in Figure 6.4.

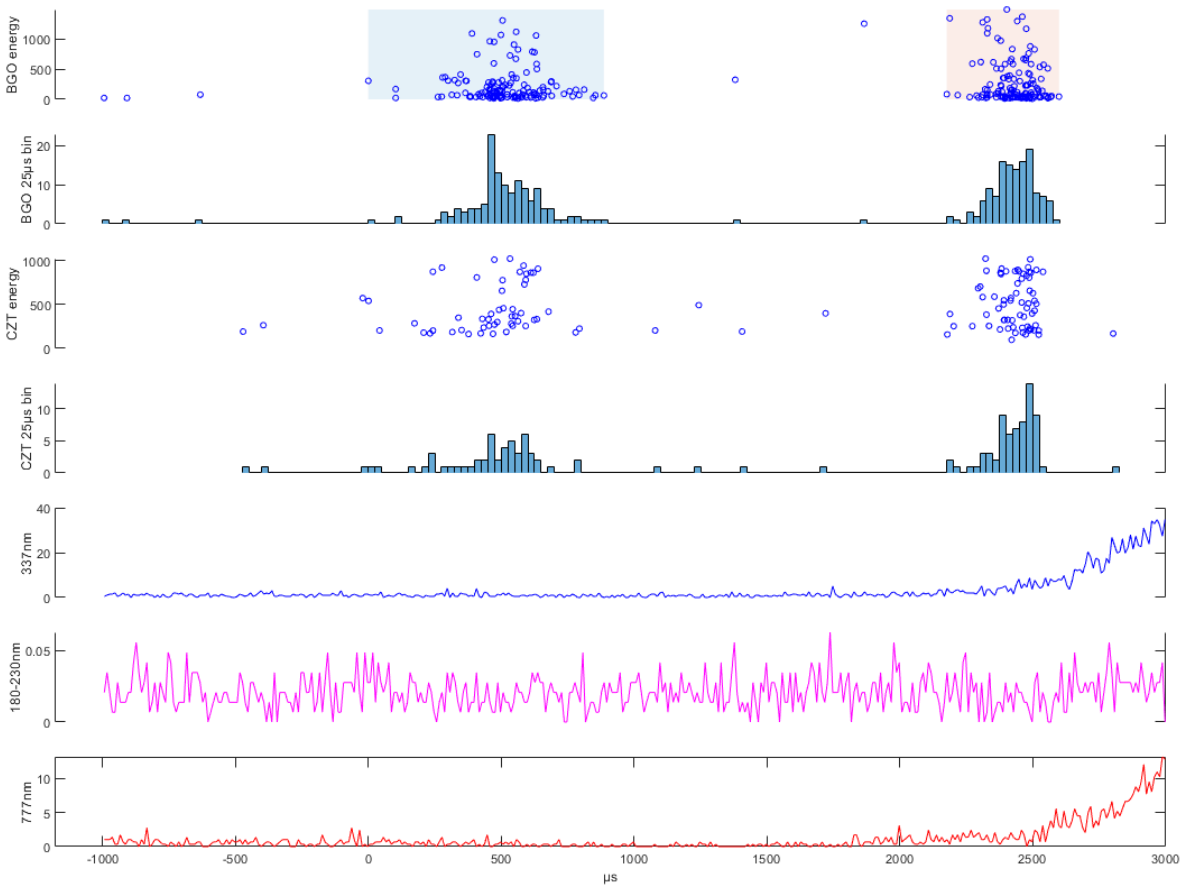

Figure 6.6: Energy scatterplot, histogram for HED and LED and lineplot for photometers of TGF 21/05/07-18:02:25.

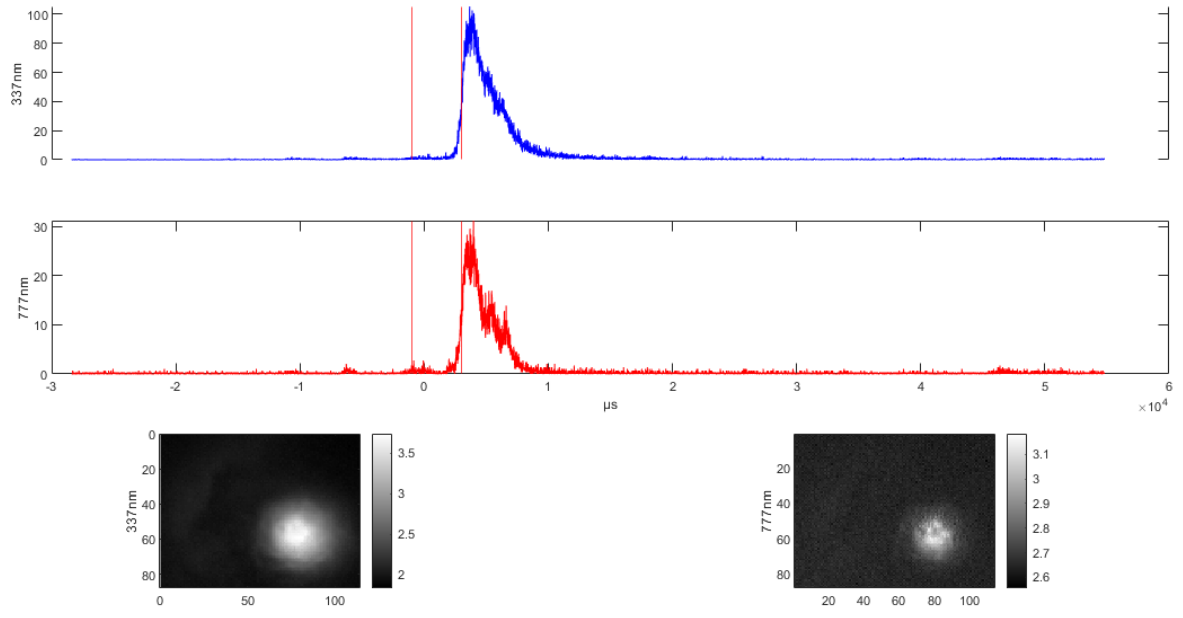

Figure 6.7: Lineplot for both frames of photometer 337 and 777 nm and camera frames for CHU 337 and 777 nm, of TGF 21/05/07-18:02:25. The red lines indicate the time interval shown in Figure 6.6.

6.2.2 Decreasing intensity

For multi pulse TGFs with decreasing intensity, most events had two peaks, with five events having three peaks and one event TGF 18/10/22-06:47:04 (not shown) having four peaks.

There where four events with optical data, TGF 21/12/30-17:57:41 (Figure 6.8) has an optical pulse associated with the last peak.

TGF 21/03/01-05:08:27 (not shown) is uncertain, the last peak could be related to the optical data but we would expect a brighter TGF if it was related to the optics.

The last two events TGF 19/04/24-23:22:21 (not shown) and TGF 21/05/07-21:25:49 (not shown) due to the low count rate and low energies it is questionable if these events are related to the optical data, they might be from outside the FoV. TGF 21/05/07-21:25:49 (not shown) also has a GLD sferic outside of the FoV within the $[-10, 40]$ ms uncertainty of ASIM which could be related to the event. Further study is needed for both of these.

TGF 21/12/30-17:57:41 (Figure 6.8) has two peaks, the first being bright while the second is weak. From the optical data it appears that both peaks occurred during the pre-activity phase, as seen by the activity in the 777 nm photometer occurring before the optical pulse. The dt value between the peaks is at around 0.8 ms, and from Figure 6.9 we can see that the optical signal is from one location. The brightness of both CHU are quite low at around 600 $\mu W m^{-2} Sr^{-1}$, which could be caused if the event was from deep inside a thick cloud. This event also had a likely associated GLD sferic which matched closely with the optical location.

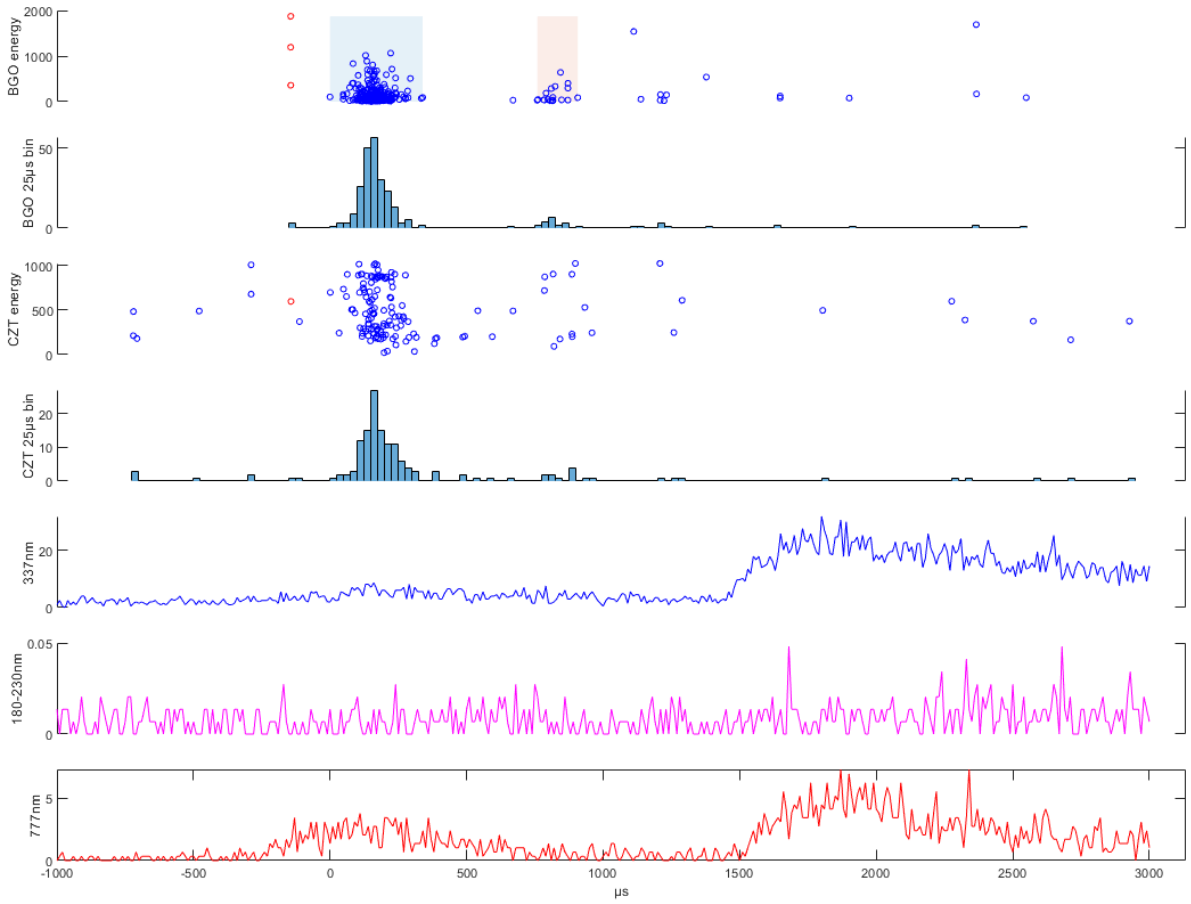

Figure 6.8: Energy scatterplot, histogram for HED and LED and lineplot for photometers of TGF 21/12/30-17:57:41.

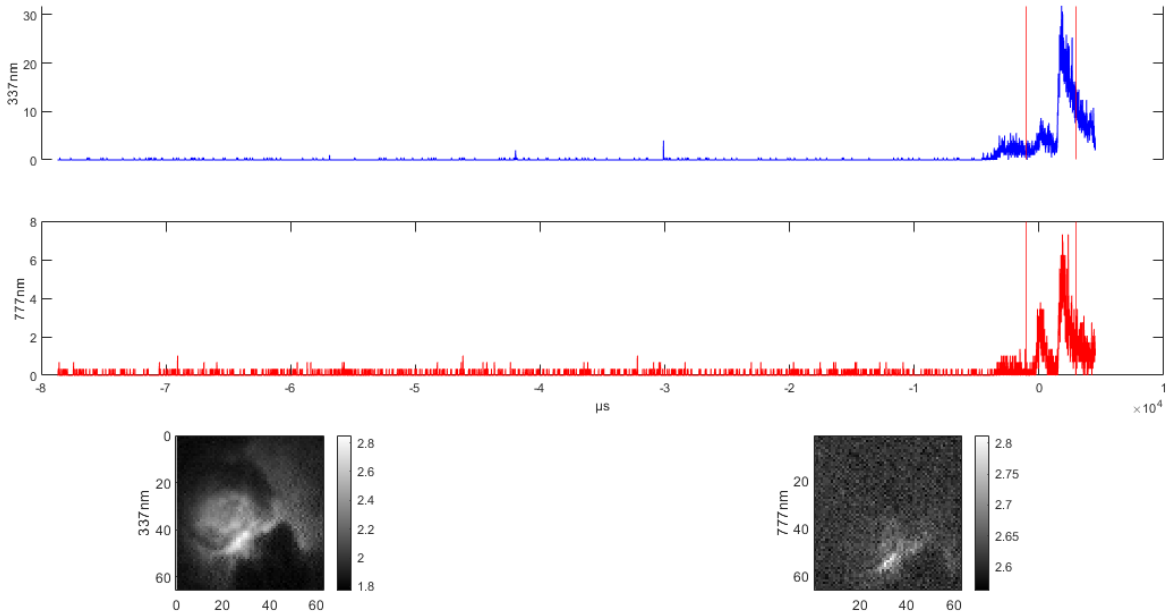

Figure 6.9: Lineplot for both frames of photometer 337 and 777 nm and camera frames for CHU 337 and 777 nm, of TGF 21/12/30-17:57:41. The red lines indicate the time interval shown in Figure 6.8.

6.2.3 Increasing intensity

For multi pulse TGFs with increasing intensity all events had two peaks with the exception of TGF 20/07/11-12:48:33 (Figure 6.10) which had three peaks.

There where five events with optical data, TGF 21/10/21-14:48:50 (Figure 6.12) had likely associated optical pulse for each peak, while TGF 20/07/11-12:48:33 (Figure 6.10) had a likely associated optical pulse for the last peak.

TGF 20/04/27-03:09:52 (not shown) is uncertain, the last peak could be related to the optical data but we would expect a brighter TGF if it was related to the optics.

The last two events TGF 21/05/10-12:51:32 (not shown), TGF 22/06/27-11:56:02 (not shown) both have low counts and low energies, which suggests that they occurred outside the FoV, in addition to having low activity in the photometers.

TGF 20/07/11-12:48:33 (Figure 6.10) has three peaks, with the first and second peak being weak and the last peak being bright with an associated optical pulse. The time from the onset of the first peak until the onset of the last peak is quite long at around 10 ms. This is much longer than the leader propagation time found by Cummer S. A. et al. [2015], which makes it questionable that all of the TGFs are from the same leader, but not unlikely. The first TGF of this event is also questionable if it is a TGF due to the low counts. Even disregarding the first peak, the dt value from the second to third peak is at about 7 ms which is still longer than the time found by Cummer S. A. et al. [2015]. Figure 6.11 shows no clear optical signal occurring during the first TGF. While there appears to be a slight optical signal occurring during the second TGF, which could indicate that the second TGF occurs during pre-activity. The third TGF appears to occur during pre-activity before the main rise. This event had a GLD sferic that matched closely with the optical location but occurred 20.1 ms before the time of the event which is outside of the $[-10, 40]$ ms uncertainty of ASIM, this makes it questionable if it is related.

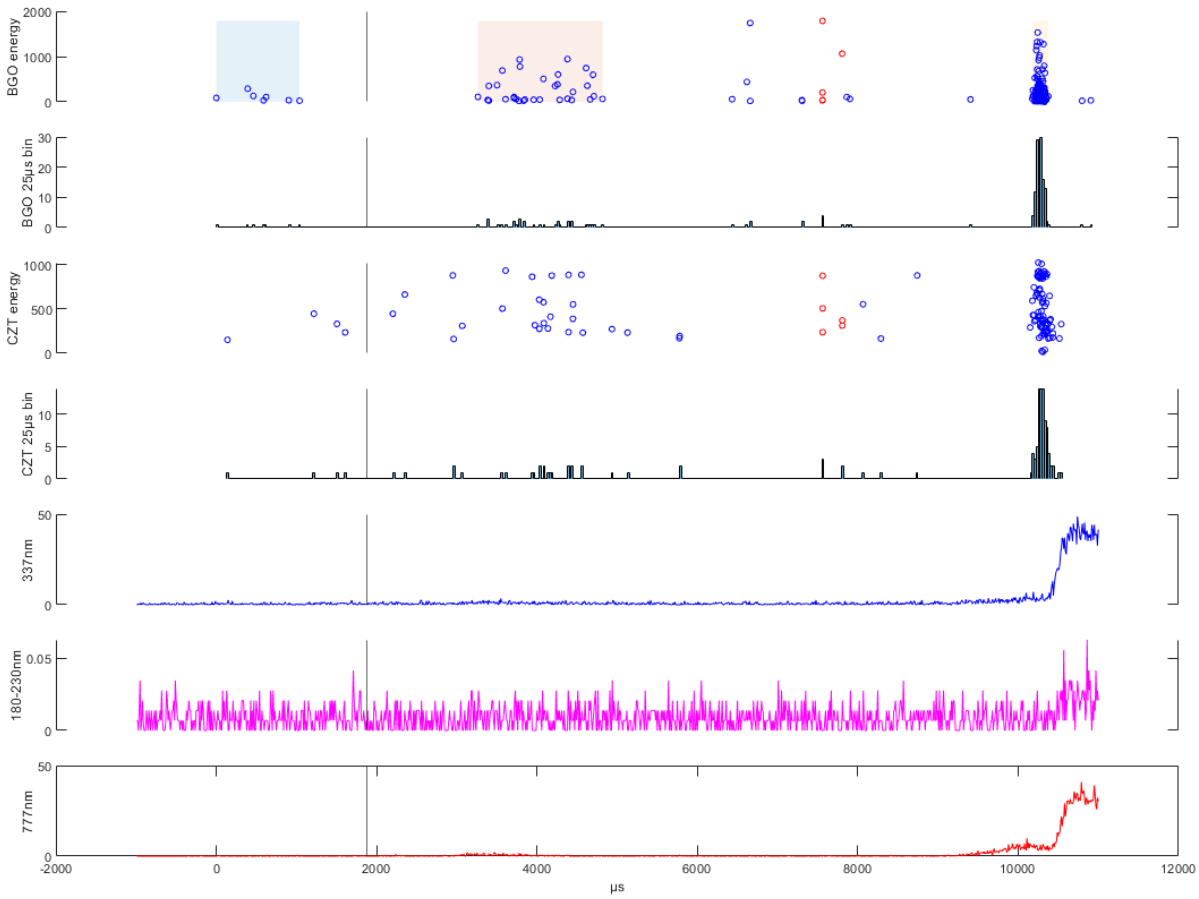

Figure 6.10: Energy scatterplot, histogram for HED and LED and lineplot for photometers of TGF 20/07/11-12:48:33. A frame split of the CHU occurs between the first and second peak indicated by the black line.

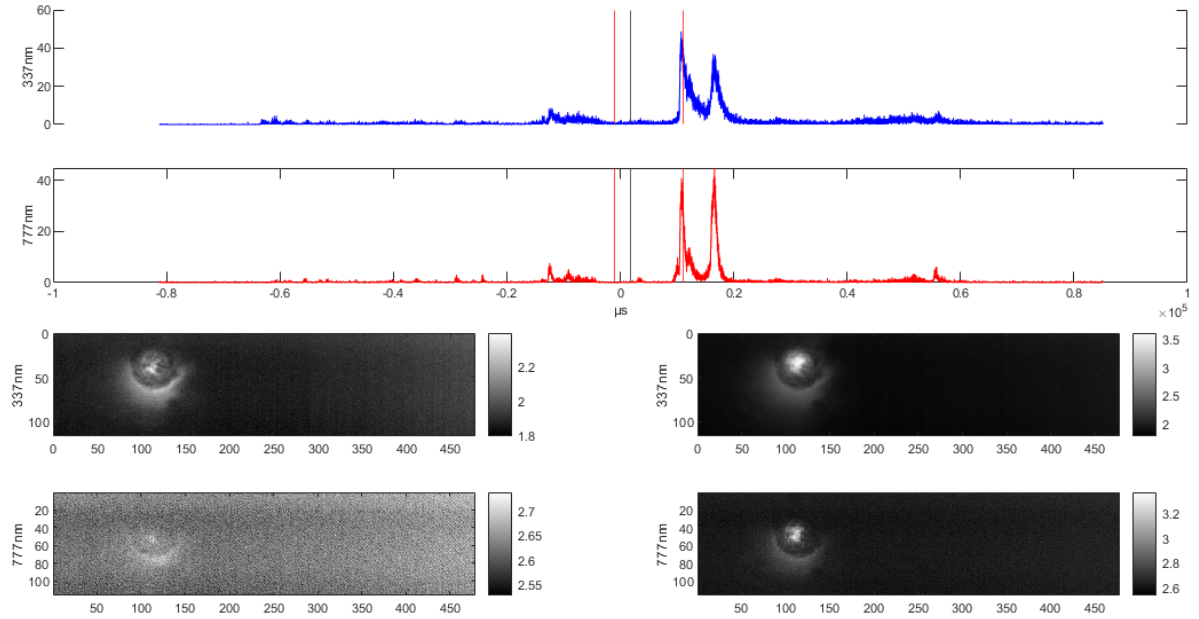

Figure 6.11: Lineplot for both frames of photometer 337 and 777 *nm* and camera frames for CHU 337 and 777 *nm*, of TGF 20/07/11-12:48:33. The frame split of the CHU is indicated by the black line, while the red lines indicate the time interval shown in Figure 6.10.

TGF 211021-14:48:50 (Figure 6.12) has two peaks both with an associated optical pulse. The dt between the peaks is at 4.6 ms which is quite long but within time of leader propagation found by Cummer S. A. et al. [2015]. This particular event had the frame split of the CHU occur between the TGF peaks meaning that each TGF peak has a separate frame on the CHU recording. From Figure 6.13 we can see that the optical signal occurs from the same region and from Figure 6.14 we can see that the optical signal is from the edge of the FoV. For this event it is reasonable that these TGFs are produced by the same leader. The CHU 777 nm brightness of this event is also remarkably high being around 31600 $\mu W m^{-2} Sr^{-1}$. However the 777 nm photometer has very low values, This is unexpected and needs to be further looked into. This event had two GLD sferics which both were within the $[-10, 40]$ ms uncertainty of ASIM and matched closely to the optical location. The time difference between these GLD sferics was at 15.3 ms which is a lot larger than the dt value between the peaks, this indicates that only one of the GLD sferics can be related to the TGFs which needs to be further looked into.

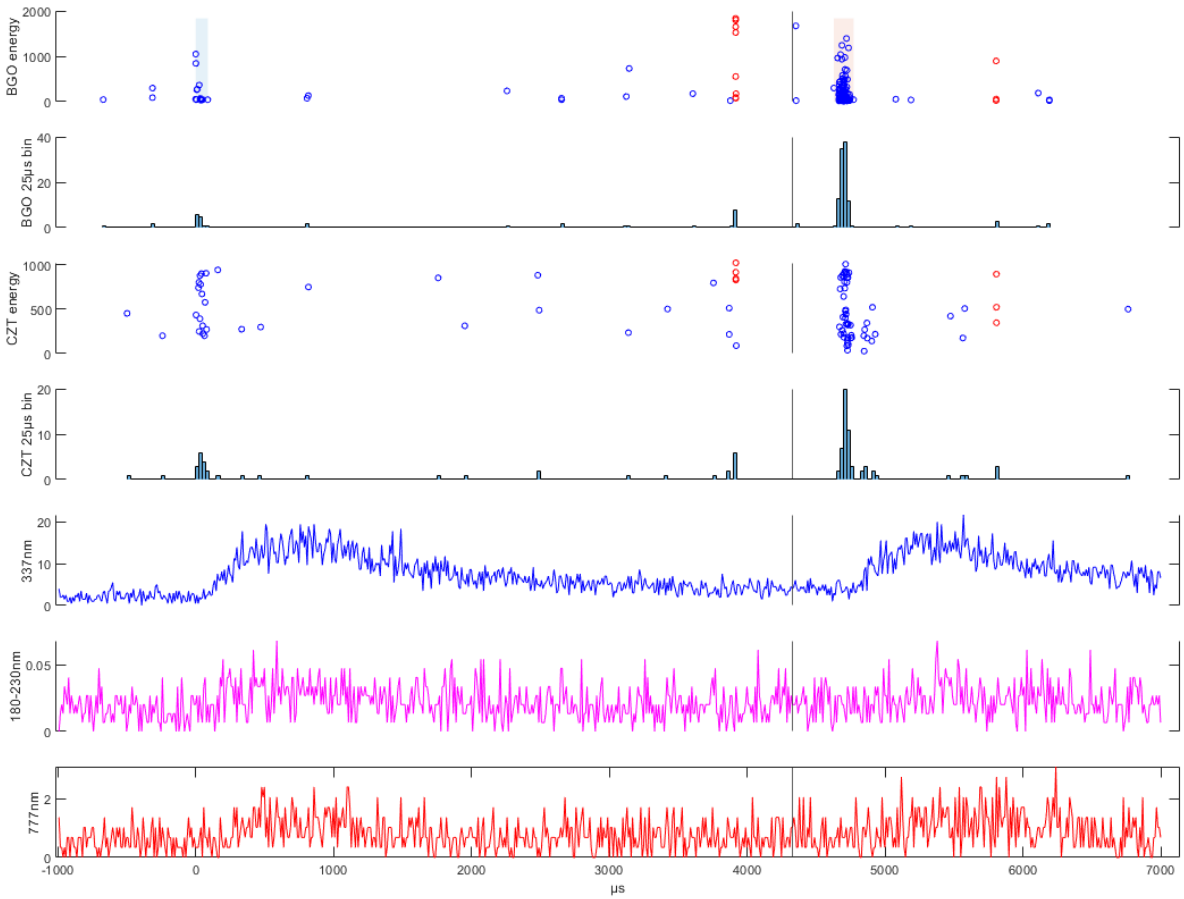

Figure 6.12: Energy scatterplot, histogram for HED and LED and lineplot for photometers of TGF 21/10/21-14:48:50. The frame split of the CHU is indicated by the black line.

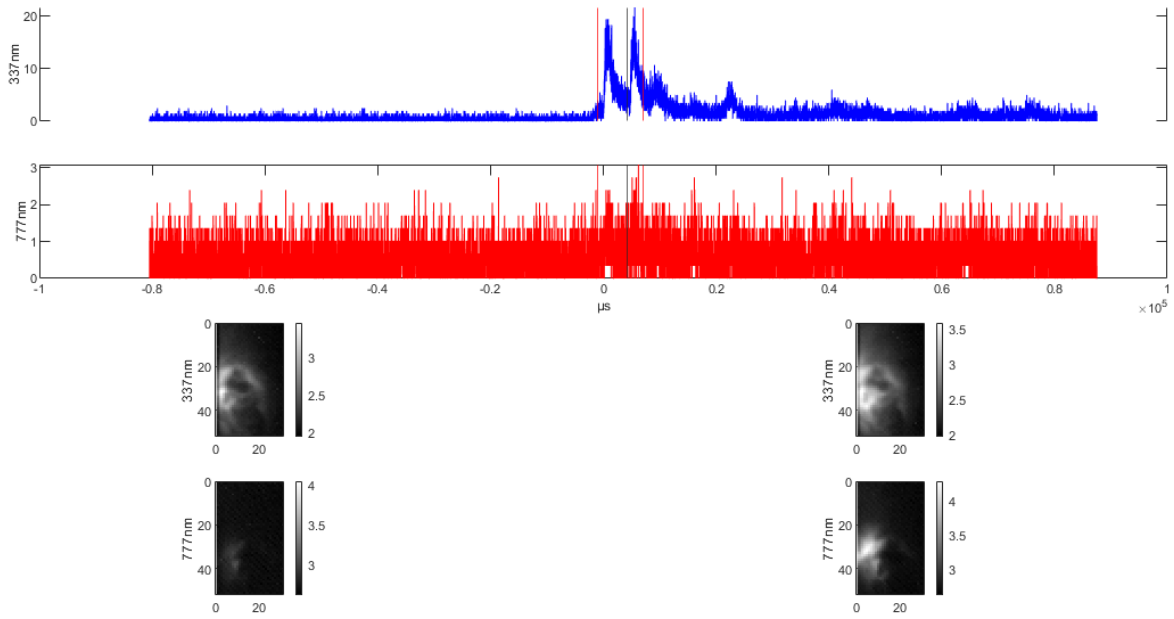

Figure 6.13: Lineplot for both frames of photometer 337 and 777 *nm* and camera frames for CHU 337 and 777 *nm*, of TGF 21/10/21-14:48:50. The frame split of the CHU is indicated by the black line, while the red lines indicate the time interval shown in Figure 6.12.

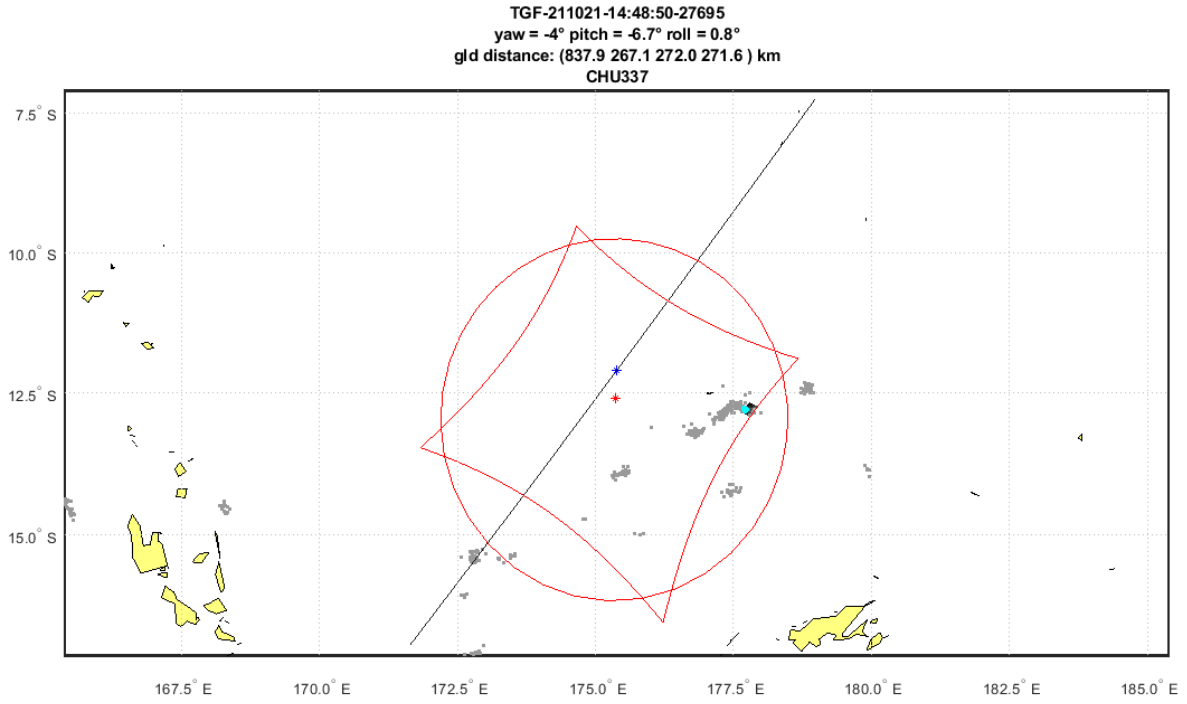

Figure 6.14: Map of TGF 21/10/21-14:48:50. The location of the optical pulse is right on the edge of the FoV, and matches closely with a GLD sferic indicated as a cyan dot.

6.3 Other notable multi pulse TGFs

TGF 21/12/09-18:09:13 (Figure 6.15) was the only multi pulse TGF found that was not weak and that did not fit into any of the groups. The event has three peaks, the first peak has no distinct optical pulse, but the photometers show weak optical activity occurring during the peak. Both the second and third peak are both followed by a distinct optical pulse. The pattern of this TGF appears to increase in intensity from peak 1 to peak 2, but then decrease in intensity from peak 2 to peak 3. It could also be argued that it has two peaks of similar intensity followed by a weak peak. The dt between the first and second peak is large at around 8.8 ms, this indicates that it is questionable if the first TGF is from the same leader as the second and third peak, but not unlikely. From Figure 6.16 we can see that the optical signal is from one spot, this indicates that the second and third peak associated with the distinct optical pulses are most likely from the same leader. Figure 6.16 shows the first TGF occurring during some weak optical activity, which could indicate the TGF occuring during pre-activity.

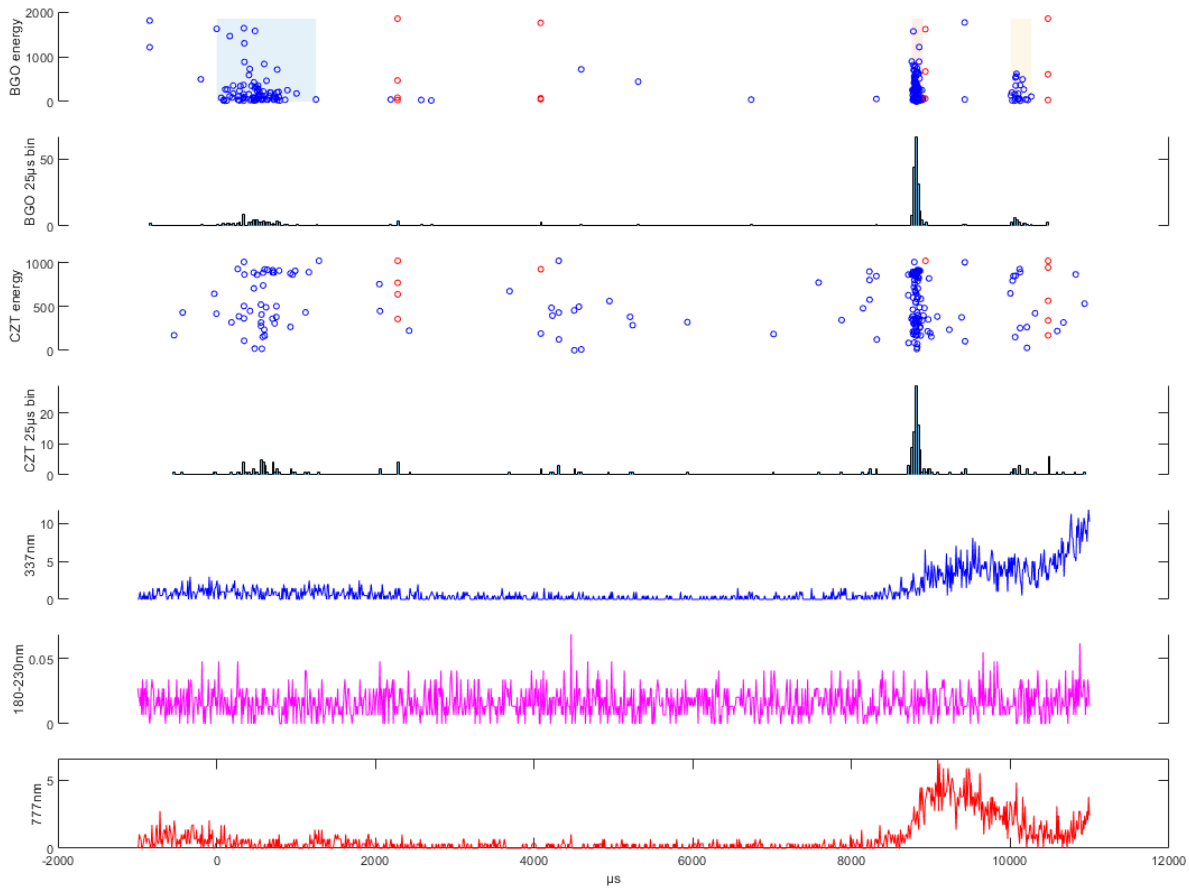

Figure 6.15: Energy scatterplot, histogram for HED and LED and lineplot for photometers of TGF 21/12/09-18:09:13.

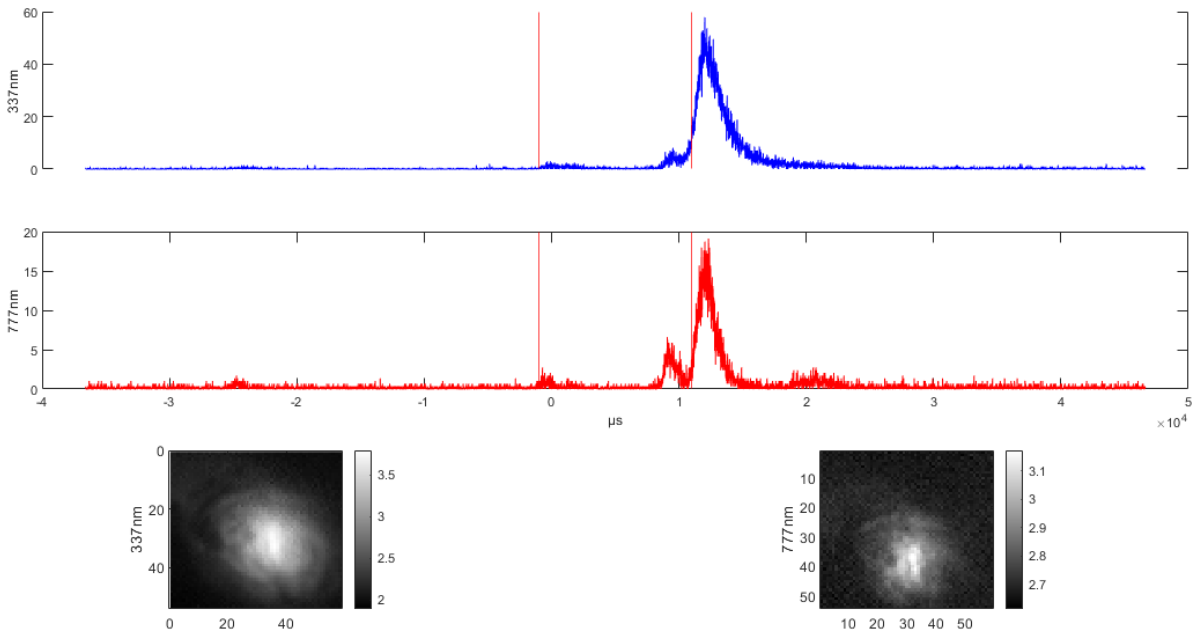

Figure 6.16: Lineplot for both frames of photometer 337 and 777 *nm* and camera frames for CHU 337 and 777 *nm*, of TGF 21/10/21-14:48:50. The red lines indicate the time interval shown in Figure 6.15.

TGF 18/06/21-16:00:53 (Figure 6.17) first reported by Østgaard et al. [2019], is a multi pulse TGF that was simultaneously observed by both ASIM and Fermi. It is an event with two peaks of similar intensity being the first and last peak, with several smaller TGFs occurring between the two main peaks. While Fermi only classified the last peak as a TGF, comparison of the event with ASIM data revealed that Fermi also saw the first peak of the event, but due to the low counts it did not pass their verification algorithm while the weaker TGFs occuring between the two main peaks could not be seen in Fermi.

In table 5.3 this event has been marked as having six peaks as indicated by the colored backgrounds in Figure 6.18. While it could be the case that this event has six peaks it could also be that the first two peaks indicated in Figure 6.18 is actually one TGF as was reported in Østgaard et al. [2019]. The gap in counts in the last peak is due to the count rate of HED being too high to detect all the photons. This event show that it is not always apparent what is one TGF or two separate TGFs and there are several multi pulse TGFs included in this thesis where the amount of peaks is uncertain. These cases have been marked under the peaks value in Table 5.2 to 5.7 with other possible peak amounts in parenthesis. However these alternate peak values have not been accounted for when looking at the separation time between peaks.

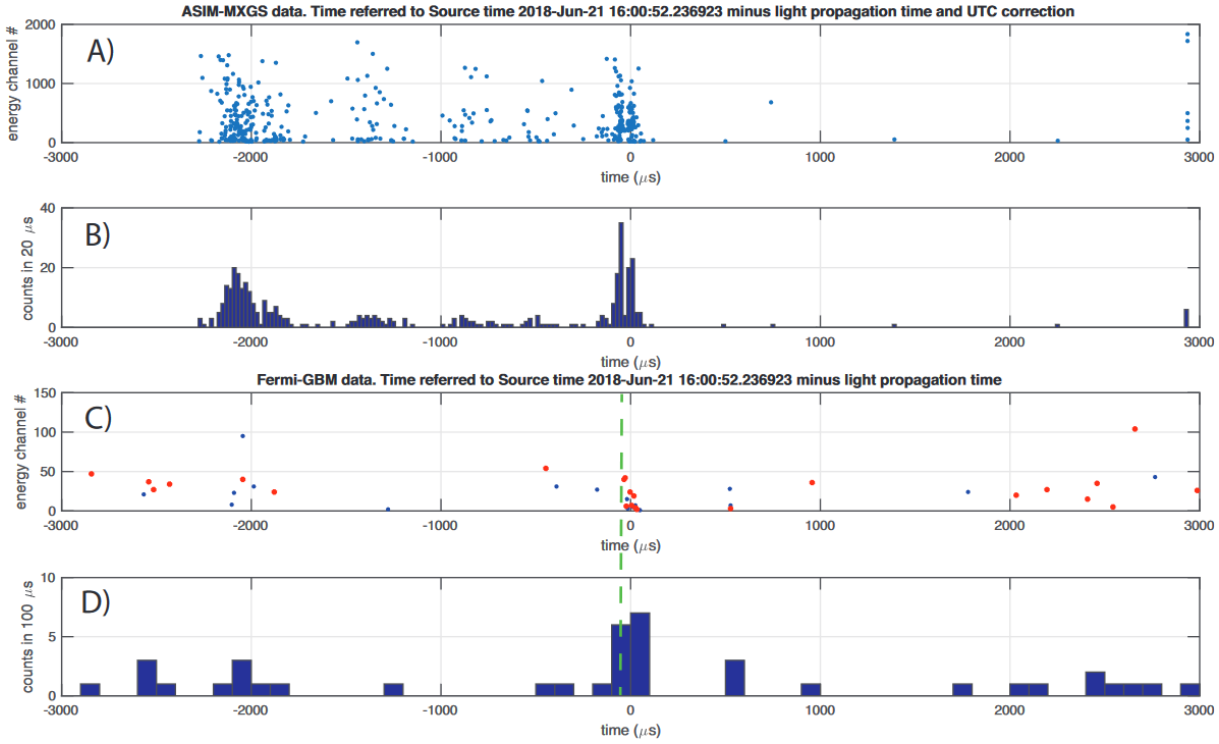

Figure 6.17: TGF 18/06/21-16:00:53, a multi pulse TGF with simultaneous observation from both ASIM and Fermi. (a) ADC scatterplot of HED. (b) Histogram with 20 μs bins of HED counts. (c) ADC scatterplot of Fermi BGOs, red is BGO 1 and blue BGO 2. (d) Histogram with 100 μs bins of Fermi BGO. The green dashed line shows WWLLN lightning stroke. Figure from Østgaard et al. [2019]

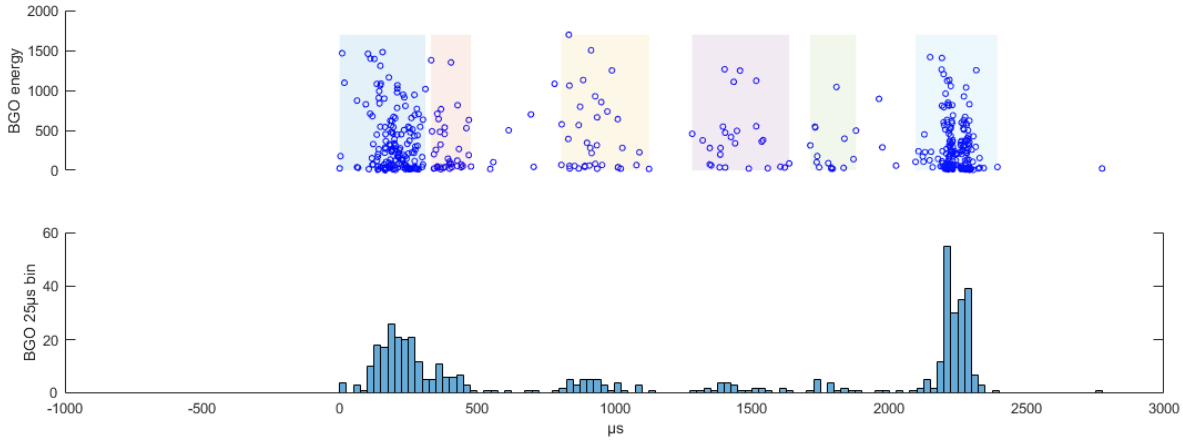

Figure 6.18: Scatterplot and histogram of HED and LED of TGF 18/06/21-16:00:53. The event occurred during daytime so LED and optical data is missing.

Generally for events with associated GLD sferics there was only one GLD likely to be associated with the events, for some cases two GLD sferics were found to likely be associated. In the cases with two associated GLD sferics the separation time between the GLD did not match the separation time between any of the TGFs from the event. There was one event TGF 19/07/31-04:57:25

(Figure 6.18) which had a similar value. The separation time between the first peak and the last peak for this event was at 1785 μs, while the separation time between the GLD sferics was at 1971 μs. Figure 6.20 shows that the two GLD sferics occurred in the same vicinity but still a couple of km apart. Both the TGF dt value and the GLD dt value are accurate down to tens of μs so the gap between the values still makes this case questionable if GLD sferics are related to the first and last TGF of the event, however it is worth looking further into.

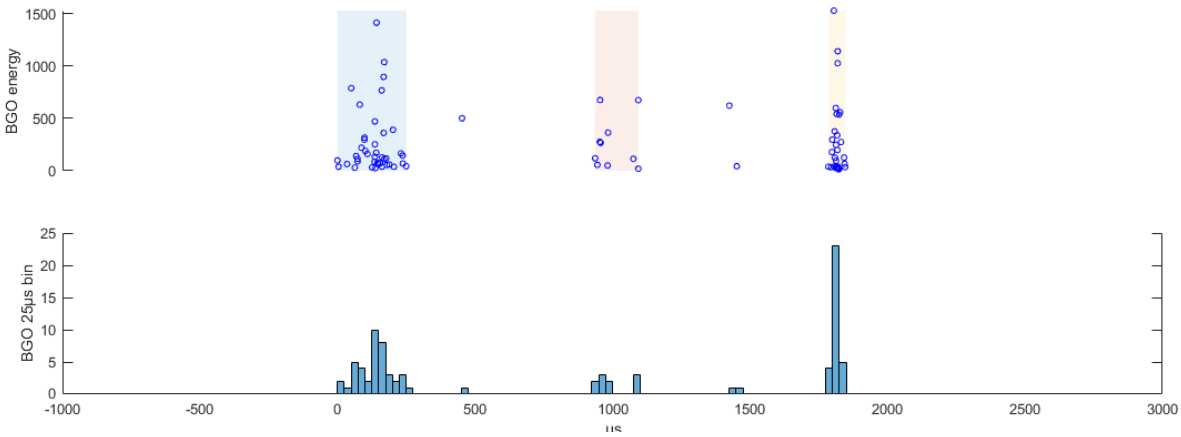

Figure 6.19: Scatterplot and histogram of HED and LED of TGF 19/07/31-04:57:25. The event occurred during daytime so LED and optical data is missing.

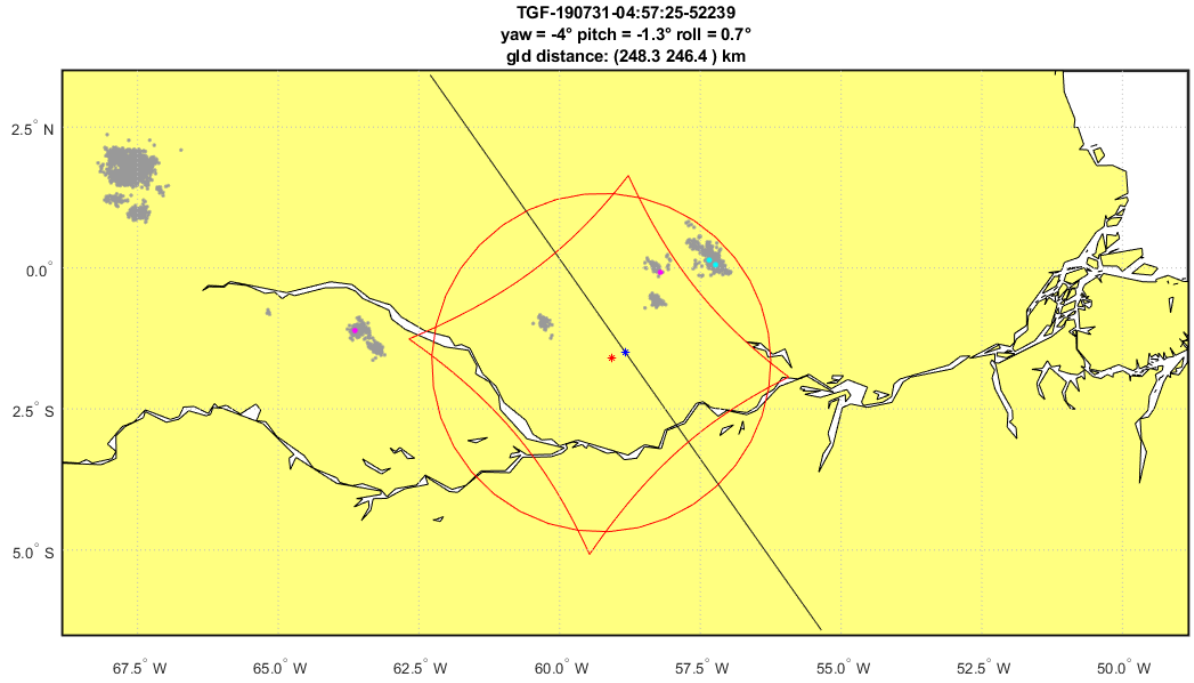

Figure 6.20: Map of TGF 19/07/31-04:57:25, the two blue dots near the edge of the FoV are the likely associated GLD sferics.

Chapter 7

Future work

From Figure 5.3 it is apparent that a larger set of multi pulse TGFs is necessary to determine if there are any statistical differences in properties of multi pulse TGFs based on region or pattern.
It is possible to use multi pulse TGFs observed by different space crafts, however care should be taken when mixing data sets from different instruments.

For radio pulses it could be possible to check multiple lightning location networks to do a more thorough check for radio pulses that could be associated with multi pulse TGFs. Additionally, preforming a time alignment of the multi pulse TGFs such as done by Bjørge-Engeland et al. [2022] could improve the timing accuracy between the TGFs and the radio pulses, which would allow determining which TGF in the multi pulse TGFs was associated with the radio pulse.

The large difference in the brightness of the CHU 777 nm and 777 nm photometer for TGF 21/10/21-14:48:50 (Figure 6.12) should be further inspected.

For the mapping of the CHU images onto geographical coordinates, the specific optical scheme of CHU 337 nm, CHU 777 nm and the photometers should be taken into account to properly determine the image projection.

Based on the separation times of multi pulse TGFs (Figure 6.1), further investigation into the propagation time of IC+ lightning leaders should be preformed.

Bibliography

Bjørge-Engeland, I., Østgaard, N., Mezentsev, A., Skeie, C. A., Sarria, D., Lapierre, J., et al. (2022). Terrestrial Gamma-ray Flashes with accompanying Elves detected by ASIM. Journal of Geophysical Research: Atmospheres, 127, e2021JD036368. https://doi.org/10.1029/2021JD036368

Briggs, M. S., et al. (2010), First results on terrestrial gamma ray flashes from the Fermi Gamma-ray Burst Monitor, J. Geophys. Res., 115, A07323, doi:10.1029/2009JA015242.

Carlson, B. E., Lehtinen, N. G., and Inan, U. S. (2007), Constraints on terrestrial gamma ray flash production from satellite observation, Geophys. Res. Lett., 34, L08809, doi:10.1029/2006GL029229.

Carlson, B. E., Lehtinen, N. G., and Inan, U. S. (2009), Terrestrial gamma ray flash production by lightning current pulses, J. Geophys. Res., 114, A00E08, doi:10.1029/2009JA014531.

Celestin, S., and Pasko, V. P. (2011), Energy and fluxes of thermal runaway electrons produced by exponential growth of streamers during the stepping of lightning leaders and in transient luminous events, J. Geophys. Res., 116, A03315, doi:10.1029/2010JA016260.

Chanrion, O., Neubert, T., Lundgaard Rasmussen, I. et al. The Modular Multispectral Imaging Array (MMIA) of the ASIM Payload on the International Space Station. Space Sci Rev 215, 28 (2019). https://doi.org/10.1007/s11214-019-0593-y

Connaughton, V., et al. (2010), Associations between Fermi Gamma-ray Burst Monitor terrestrial gamma ray flashes and sferics from the World Wide Lightning Location Network, J. Geophys. Res., 115, A12307, doi:10.1029/2010JA015681.

Connaughton, V., et al. (2013), Radio signals from electron beams in terrestrial gamma ray flashes, J. Geophys. Res. Space Physics, 118, 2313–2320, doi:10.1029/2012JA018288.

Cooray V. (2003) The Lightning Flash

Cummer, S. A., Lyu, F., Briggs, M. S., Fitzpatrick, G., Roberts, O. J., and Dwyer, J. R. (2015), Lightning leader altitude progression in terrestrial gamma-ray flashes, Geophys. Res. Lett., 42, 7792– 7798, doi:10.1002/2015GL065228.

Dwyer J. R. (2003), A fundamental limit on electric fields in air , Geophys. Res. Lett., 30, 2055, doi:10.1029/2003GL017781, 20.

Dwyer, J.R., Smith, D.M. & Cummer, S.A. High-Energy Atmospheric Physics: Terrestrial Gamma-Ray Flashes and Related Phenomena. Space Sci Rev 173, 133–196 (2012). https://doi.org/10.1007/s11214-012-9894-0

Dwyer, J. R. (2012), The relativistic feedback discharge model of terrestrial gamma ray flashes, J. Geophys. Res., 117, A02308, doi:10.1029/2011JA017160.

Fishman G. J., Bhat P. N, et al. (1994), Discovery of Intense Gamma-Ray Flashes of Atmospheric Origin, science, New Series, Vol. 264, No. 5163 (May 27, 1994), 1313-1316.

Foley, S., et al. (2014), Pulse properties of terrestrial gamma-ray flashes detected by the Fermi Gamma-Ray Burst Monitor, J. Geophys. Res. Space Physics, 119, 5931– 5942, doi:10.1002/2014JA019805.

Gjesteland, T., Østgaard, N., Collier, A. B., Carlson, B. E., Cohen, M. B., and Lehtinen, N. G. (2011), Confining the angular distribution of terrestrial gamma ray flash emission, J. Geophys. Res., 116, A11313, doi:10.1029/2011JA016716.

Grefenstette, B. W., Smith, D. M., Hazelton, B. J., and Lopez, L. I. (2009), First RHESSI terrestrial gamma ray flash catalog, J. Geophys. Res., 114, A02314, doi:10.1029/2008JA013721.

Hatton J. , The ISS as an Earth observation platform,
URL: https://esamultimedia.esa.int/docs/hsf_research/Climate_change_ISS_presentations/ISS-as-observation-platform-Hatton.pdf, [Accessed 26-Apr-2023]

Hazelton, B. J., Grefenstette, B. W., Smith, D. M., Dwyer, J. R., Shao, X.-M., Cummer, S. A., Chronis, T., Lay, E. H., and Holzworth, R. H. (2009), Spectral dependence of terrestrial gamma-ray flashes on source distance, Geophys. Res. Lett., 36, L01108, doi:10.1029/2008GL035906.

Heumesser, M., Chanrion, O., Neubert, T., Christian, H. J., Dimitriadou, K., Gordillo-Vazquez, F. J., et al. (2021). Spectral observations of optical emissions associated with Terrestrial Gamma-Ray Flashes. Geophysical Research Letters, 48, e2020GL090700. https://doi.org/10.1029/2020GL090700

Lindanger, A., Marisaldi, M., Maiorana, C., Sarria, D., Albrechtsen, K., Østgaard, N., et al. (2020). The 3rd AGILE Terrestrial Gamma Ray Flash Catalog. Part I: Association to Lightning Sferics. Journal of Geophysical Research: Atmospheres, 125, e2019JD031985. https://doi.org/10.1029/2019JD031985

Lindanger, A., Marisaldi, M., Sarria, D., Østgaard, N., Lehtinen, N., Skeie, C. A., et al. (2021). Spectral analysis of individual terrestrial gamma-ray flashes detected by ASIM. Journal of Geophysical Research: Atmospheres, 126, e2021JD035347. https://doi.org/10.1029/2021JD035347

Mailyan, B., Stanbro, M., Briggs, M. S., Cummer, S., Dwyer, J. R., Roberts, O. J., & Holzworth, R. (2021). Radio Frequency Emissions Associated With Multi-Pulsed Terrestrial Gamma-Ray Flashes. Journal of Geophysical Research: Space Physics, 126, e2020JA027928. https://doi.org/10.1029/2020JA027928

Marisaldi, M., et al. (2010), Detection of terrestrial gamma ray flashes up to 40 MeV by the AGILE satellite, J. Geophys. Res., 115, A00E13, doi:10.1029/2009JA014502.

Mezentsev, A., Østgaard, N., Gjesteland, T., Albrechtsen, K., Lehtinen, N., Marisaldi, M., Smith, D., and Cummer, S. (2016), Radio emissions from double RHESSI TGFs, J. Geophys. Res. Atmos., 121, 8006– 8022, doi:10.1002/2016JD025111.

Moss G., Pasko V. P., Liu N., and Veronis G. (2006), Monte Carlo model for analysis of thermal runaway electrons in streamer tips in transient luminous events and streamer zones of lightning leaders, J. Geophys. Res., 111, A02307, doi:10.1029/2005JA011350.

Neubert T., Østgaard N., Reglero V. et al. The ASIM Mission on the International Space Station. Space Sci Rev 215, 26 (2019). https://doi.org/10.1007/s11214-019-0592-z

Paolini M. L.ISS Tracker, URL: http://www.isstracker.com/home

Rakov V. A., Uman M. A. (2003) Lightning: Physics and Effects.

Said R., Murphy M. (2016). GLD360 Upgrade: Performance Analysis and Applications.

Skeie, C. A., Østgaard, N., Mezentsev, A., Bjørge-Engeland, I., Marisaldi, M., Lehtinen, N., et al. (2022). The temporal relationship between terrestrial gamma-ray flashes and associated optical pulses from lightning. Journal of Geophysical Research: Atmospheres, 127, e2022JD037128. https://doi.org/10.1029/2022JD037128

Stanbro, M. C., Briggs, M. S., Roberts, O. J., Cramer, E. S., Cummer, S. A., & Grove, J. E. (2018). A Study of Consecutive Terrestrial Gamma-ray Flashes Using the Gamma-ray Burst Monitor. Journal of Geophysical Research: Space Physics, 123, 9634– 9651. https://doi.org/10.1029/2018JA025710

Stolzenburg, M., Rust, W. D., and Marshall, T. C. (1998), Electrical structure in thunderstorm convective regions 3. Synthesis, J. Geophys. Res., 103(D12), 14097– 14108, doi:10.1029/97JD03545.

Vectornav,Referance Frames, URL:https://www.vectornav.com/resources/inertial-navigation-primer/math-fundamentals/math-refframes, [Accessed 26-Apr-2023]

William H. B., METEO 300:Fundamentals of Atmospheric Science, url = https://www.e-education.psu.edu/meteo300/node/624, [Accessed 9-feb-2023]

Østgaard, N., Gjesteland, T., Stadsnes, J., Connell, P. H., and Carlson, B. (2008), Production altitude and time delays of the terrestrial gamma flashes:

Revisiting the Burst and Transient Source Experiment spectra, J. Geophys. Res., 113, A02307, doi:10.1029/2007JA012618.

Østgaard, N., Balling, J.E., Bjørnsen, T. et al. The Modular X- and Gamma-Ray Sensor (MXGS) of the ASIM Payload on the International Space Station.. Space Sci Rev 215, 23 (2019). https://doi.org/10.1007/s11214-018-0573-7

Østgaard, N., Neubert, T., Reglero, V., Ullaland, K., Yang, S., Genov, G., et al. (2019). First 10 Months of TGF Observations by ASIM. Journal of Geophysical Research: Atmospheres, 2019; 124: 14024– 14036. https://doi.org/10.1029/2019JD031214